# A Six Degree of Freedom Flexural Positioning Stage

by

Gordon A.B. Anderson

BSc Mechanical Engineering (1999)

University of the Witwatersrand, Johannesburg, South Africa

Submitted to the Department of Mechanical Engineering in Partial Fulfillment of the Requirements for the Degree of Master of Science in Mechanical Engineering

at the

Massachusetts Institute of Technology

February 2003



Signature of Author.....
Department of Mechanical Engineering
January 24, 2003

Certified by.....
Martin Culpepper
Assistant Professor of Mechanical Engineering
Thesis Supervisor

Accepted by.....
Ain A. Sonin
Chairman, Department Committee on Graduate Students

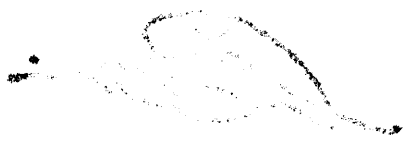

A Six Degree of Freedom Flexural Positioning Stage

by

Gordon A.B. Anderson

Submitted to the Department of Mechanical Engineering on January 24, 2003 in partial fulfillment of the requirements for the Degree of Master of Science in Mechanical Engineering

# Abstract

A novel, low-cost positioning stage was constructed using a six-axis compliant mechanism driven by three two-axis electromagnetic actuators. The mechanism's monolithic, planar geometry is easily fabricated with low-cost manufacturing processes (such as waterjet machining). The manipulator tolerates ±1 mm actuator misalignment with less than 0.1% full-scale position error. Measurements over a 100x100x100 $nm^3$ work volume displayed resolution better than the sensing capability, 5nm, and open-loop linearity errors less than 0.005% of the full-scale range (100 μm). Measurements over a 100x100x100 $\mu m^3$ work volume exhibited linearity errors less than 0.20% full-scale. The mechanism's equilateral symmetry and planar geometry restricted thermal drift rates at start-up to 23nm and 4 μradians over 30 minutes and 0.1°C temperature change. The manipulator, built for $ 2000 (excluding electronics), was successfully tested in a fiber optic alignment application.

Thesis Supervisor: Martin Culpepper

Title: Assistant Professor of Mechanical Engineering

# Acknowledgements

To my advisor, Prof Martin Culpepper, thank you for accepting me into your research group, funding my study and providing all the help necessary to complete this project. I was fortunate to be given such an interesting thesis topic.

I owe a debt of gratitude to the Institute of International Education (IIE) and the SA-USA Fulbright Commission which together with Prof Culpepper financed my time in the USA. My thanks are due in particular to Sarah Ilchman at the IIE and Riana Coetsee and Monica Joyi of the SA-USA Fulbright Commission.

The friendship, advice and support of my lab mates will not be forgotten. I thank Carlos Araque and Naomi Davidson for instruction in data acquisition; Patrick Petri for developing the CoMeT compliant mechanism analysis program and formulating a method for controlling the positioning stage; Shih-Chi Chen for advice on optical fiber alignment; and Tzu-Liang Loh for his readiness to help in the machine shop.

Etan Trangle and Mark Velsco played a significant part in the final month of the project. Etan implemented the control system and Mark designed and built the fiber optic alignment apparatus for the case study.

Prof Rajeev Ram and Harry Lee from the MIT Physical Optics and Electronics Group made available a laser and transmission loss detector for the fiber alignment case study. Harry Lee demonstrated remarkable patience in teaching me how to cleave optical fiber.

Prof David Trumper, head of the MIT Precision Motion Control Group, advised on the actuator control electronics.

I valued the instruction from Gerald Wentworth and Mark Belanger in the MIT LMP machine shop. The hours Mark Belanger contributed in helping machine parts were crucial for meeting the project deadline.

Finally I must thank Leslie Regan of the Mechanical Engineering Graduate Office for her intervention through which I gained admission to MIT.

# Table of Contents


Abstract ..... 3

Acknowledgements ..... 4

Table of Contents ..... 5

List of Figures ..... 7

List of Tables ..... 10

Chapter 1 Introduction ..... 11

1.1 Motivation ..... 11

1.2 Hexflex Description ..... 12

1.3 Fundamental Issues ..... 19

Chapter 2 Background ..... 20

2.1 Flexure Systems ..... 20

2.2 Actuator Technology ..... 21

Chapter 3 Design ..... 58

3.1 Requirement Specification ..... 58

3.2 Concept Selection Process ..... 59

3.3 Analysis ..... 67

3.4 Error Estimate ..... 99

3.5 General Arrangement ..... 100

3.6 Cost Summary ..... 107

Chapter 4 Testing ..... 109

4.1 Instrumentation ..... 109

4.2 CoMeT Validation ..... 111

4.3 Actuator analysis validation ..... 115

4.4 Calibration ..... 118

4.5 Displacement results ..... 119

4.6 Repeatability ..... 121

4.7 Natural Frequency ..... 122

4.8 Drift ..... 123

Chapter 5 Case Study ..... 125

5.1 Introduction ..... 125
5.2 Testing ..... 129
Chapter 6 Conclusions ..... 132
Chapter 7 References ..... 134
Appendix A Electromagnet Actuation ..... 137
Appendix B Repeatability Histograms ..... 147
Appendix C Frequency Response Plots ..... 149

# List of Figures

Figure 1-1 Six axis concept ..... 13
Figure 1-2 Components of a six-axis, three tab compliant mechanism ..... 15
Figure 1-3 Sample stage position changes for combined actuator input ..... 17
Figure 2-1 Stack actuator schematic ..... 27
Figure 2-2 Bimorph actuator ..... 27
Figure 2-3 Actuator with mechanical amplifier ..... 29
Figure 2-4 Capstan drive ..... 31
Figure 2-5 Dynamic linear spring actuator ..... 33
Figure 2-6 Magnetostrictive actuator schematic ..... 35
Figure 2-7 Basic solenoid actuator ..... 41
Figure 2-8 Moving coil actuator ..... 45
Figure 2-9 Linear spring with a four-magnet, two-coil actuator ..... 49
Figure 2-10 Magnet coil nomenclature ..... 49
Figure 2-11 Geometry factor for a uniformly wound cylindrical coil ..... 51
Figure 2-12 Parallel plate capacitor ..... 53
Figure 2-13 Bellows actuator system ..... 55
Figure 3-1 Actuator range vs. accuracy ..... 59
Figure 3-2 Sphere and flat coupling ..... 63
Figure 3-3 Flexural joint coupling ..... 63
Figure 3-4 Electromagnetic field coupling ..... 64
Figure 3-5 Comet screen capture ..... 67
Figure 3-6 Single-coil actuator ..... 70
Figure 3-7 Dual-coil actuator ..... 71
Figure 3-8 Specific force vs. magnet displacement ..... 72
Figure 3-9 Magnetic flux due to a current loop ..... 73
Figure 3-10 Nomenclature for Garret's equations ..... 74
Figure 3-11 Surface plot of $f_z$ vs. $a_1$ and $g$ ..... 77
Figure 3-12 Surface plot of variation in $f_z$ vs. $a_1$ and $g$ ..... 77
Figure 3-13 Specific force vs. $\alpha$ and $\beta$ ..... 79

# List of Figures contd.

Figure 3-14 Percentage variation in $f_z$ over actuator range vs. $\alpha$ and $\beta$ ..... 81
Figure 3-15 Variation in $f_z$ over a ±0.6mm radial operating range ..... 83
Figure 3-16 Variation in $f_z$ over a ±0.6mm axial operating range ..... 84
Figure 3-17 Contour plot of percentage variation in $f_z$ vs. r and z. ..... 85
Figure 3-18 Coil configuration in dual axis actuator ..... 87
Figure 3-19 Magnetic flux lines for 1 amp coil current ..... 89
Figure 3-20 Temperature distribution with all aluminum construction ..... 93
Figure 3-21 Temperature distribution with aluminum/acetal resin construction ..... 95
Figure 3-22 Temperature distribution with aluminum/tufnol/acetal resin ..... 97
Figure 3-23 Positioning stage ..... 101
Figure 3-24 Hexflex exploded assembly ..... 103
Figure 3-25 Dual-axis actuator assembly ..... 105
Figure 4-1 Apparatus ..... 111
Figure 4-2 Force displacement transmission ratio: tab 1 in-plane ..... 113
Figure 4-3 Force displacement transmission ratio: tab 1 out-of-plane ..... 114
Figure 4-4 Centroid displacement vs. current: tab 1 in-plane ..... 116
Figure 4-5 Centroid displacement vs. current: tab 1 out-of-plane ..... 117
Figure 4-6 Percentage variation in $f_z$ vs. $r$ ..... 120
Figure 4-7 Drift test – position variation ..... 123
Figure 4-8 Drift test – temperature variation ..... 124
Figure 5-1 Transverse offset ..... 126
Figure 5-2 Longitudinal offset ..... 127
Figure 5-3 Longitudinal separation ..... 127
Figure 5-4 Fiber alignment apparatus ..... 129
Figure 5-5 Transmission loss vs. time ..... 131
Figure A-1 Response to x command input (micro-manipulation) ..... 138
Figure A-2 Response to y command input (micro-manipulation) ..... 139
Figure A-3 Response to z command input (micro-manipulation) ..... 140

# List of Figures contd.

Figure A-4 Response to theta x command input ..... 141
Figure A-5 Response to theta y command input ..... 142
Figure A-6 Response to theta z command input ..... 143
Figure A-7 Response to x command input (nano-manipulation) ..... 144
Figure A-8 Response to y command input (nano-manipulation) ..... 145
Figure A-9 Response to z command input (nano-manipulation) ..... 146
Figure B-1 Repeatability summary ..... 148
Figure C-1 Response to impulse ..... 149
Figure C-2 Frequency response ..... 150

# List of Tables

Table 2-1 Comparison of commercial magnetostrictive and piezo actuators ..... 37
Table 3-1: Design requirements for the six-axis nano-manipulator ..... 58
Table 3-2 Actuator attribute summary ..... 64
Table 3-3 Actuator selection chart ..... 65
Table 3-4 Out-of-plane force contributions ..... 89
Table 3-5 In-plane force contributions ..... 91
Table 3-6 Clockwise moment contributions about the tab longitudinal axis ..... 91
Table 3-7 Error estimate ..... 99
Table 3-8 Manufacturing costs ..... 107
Table 4-1 Error summary (-50μm to 50μm translation) ..... 119
Table 4-2 Error summary (0 – 0.100 μm translation) ..... 120
Table 4-3 Repeatability results ..... 121
Table 4-4 Natural frequency of vibration ..... 122

# Chapter 1 Introduction

## 1.1 Motivation

From optical lithography to photonic packaging, precise positioning and manipulation are essential technologies. These areas are of fundamental importance in the alignment of satellite antenna, semiconductor processing, control of secondary mirrors in astronomical telescopes and small scale machining and assembly processes required in the burgeoning field of nanotechnology. The sought after attributes of positioning devices include compactness, repeatable high resolution positioning (i.e. no/low hysteresis) and high natural frequency.

Conventional micro-positioning systems use a series of stacked stages. There have been attempts to change this space inefficient practice through stage integration: Ryu et al [1] have developed a monolithic XYθ stage for wafer stepping applications, while Nomura and Suzuki [2] devised a low-height six degree of freedom (DOF) device with four nested stages on low profile guide ways. A similarly compact 6 DOF design by Taniguchi et al [3] positioned a wafer chuck with six piezoelectric actuator links. Integration has also been achieved through other means – Holmes et al [4] constructed a 6 DOF magnetically levitated stage for scanned probe microscopy, while Stewart platforms [5] have been popular for optical alignment. Though novel, none of the 6 DOF devices scaled well (with respect to the attributes laid out above) when one desires compact devices for nanometer-level positioning.

Consequently other designs [6] [7] [8] have been proposed for six-axis, small scale manipulation in MEMs and photonics. Although these are significant advances in the state of the art, each is based on the use of an assembled, three dimensional structure to produce motion in six axes. Looking toward the future, simplicity of design and ease of manufacture would be improved if such devices could be planar.

## 1.2 Hexflex Description [9]

The Hexflex, a planar, monolithic structure developed at the MIT Precision Systems Design and Manufacturing (PSDAM) Laboratory has the potential to satisfy all requirements of next-generation 6 DOF manipulation. It offers rapid response, unlike stacked axis systems where the base axis must move the mass of the axes stacked above.

The planar six-axis compliant mechanism takes advantage of the fact that elements of compliant structures act as hinges at locations where loads are applied. In Figure 1-1 A the applied torque ($T_z$) results in a displacement of the stage's vertices. The vertex adjacent to $T_z$ is displaced to the side while the remaining vertices are constrained to move perpendicular to their supports. The result is in-plane motion ($x$ translation and $\theta_z$ rotation) of the stage centroid. Out-of-plane motion is achieved through out-of-plane forces ($F_z$) and in-plane moments ($T_p$).

Unfortunately, it is difficult to implement rotary actuation to apply sufficient moments in the manner depicted in Figure 1-1 A and B. An adaptation of the mechanism, the Hexflex, is shown in Figure 1-2. This design includes lever arms, called tabs, which make it easier to apply $T_p$ and $F_z$. The tabs can be displaced in-plane and out-of-plane by linear actuators. This provides the effective force ($F_z$), and moment ($T_p$) which then causes the desired motion. Combinations of in-plane and out-of-plane loads can be used to achieve one to six-axis motion between the stage and ground. Intuitive examples of single axis actuation-motion combinations are provided in Figure 1-3. Multi-axis combinations can be visualized using superposition of the examples.

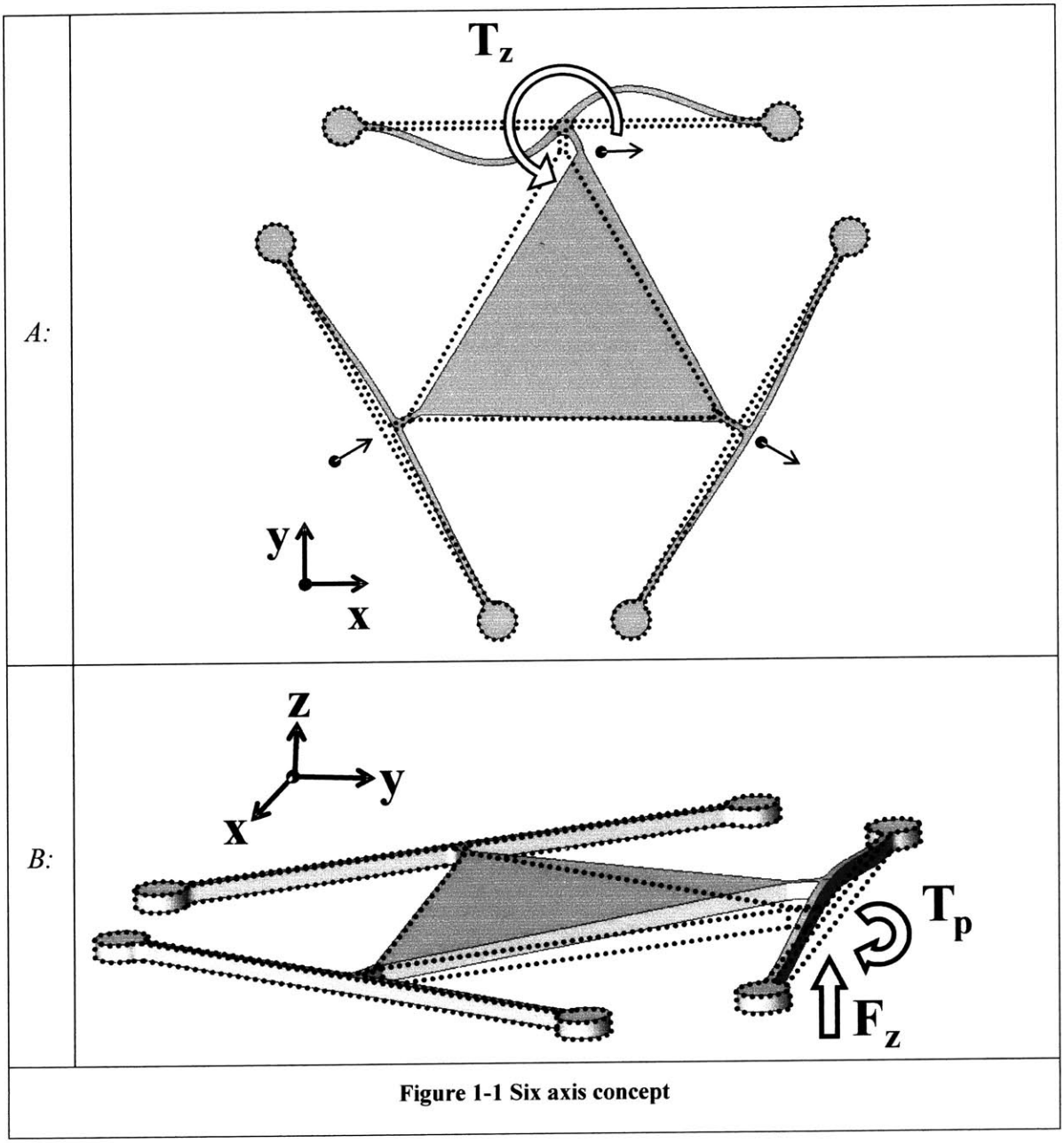


**Figure 1-1 Six axis concept**

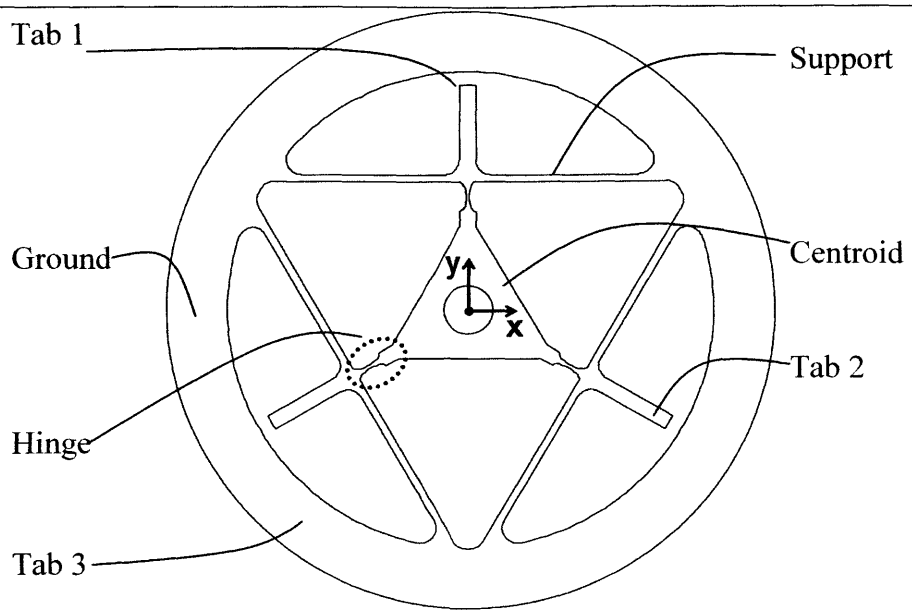


**Figure 1-2 Components of a six-axis, three tab compliant mechanism**

The geometry of the compliant mechanism was developed with CoMeT (**Co**mpliant **Me**chanisms **T**ool). CoMeT is a Matlab script originating in the PSDAM Laboratory with the following features:

Direct input-output mapping - As part of the deformation analysis, CoMeT provides two *m* x *n* input-output matrices that map *n* actuator inputs to *m* stage motions. The first matrix ($\mathbf{S_F}$) relates stage motions ($\mathbf{X_C}$) to the applied forces ($\mathbf{F_A}$) as shown in Eq. ( 1-1).

$$X_C = S_F F_A \rightarrow \begin{bmatrix} x & y & z & \theta_x & \theta_y & \theta_z \end{bmatrix}^T = S_F \begin{bmatrix} f_{1p} & f_{2p} & f_{3p} & f_{1z} & f_{2z} & f_{3z} \end{bmatrix}^T \quad \textbf{(1-1)}$$

Here forces $f_{ij}$ are applied at tab $i$ in direction $j$ ( $j$ = p for in-plane or $z$ for out-of-plane). The second matrix ($\mathbf{S_X}$) relates stage motions ($\mathbf{X_C}$) to the displacements ($\mathbf{X_A}$) applied to the lever arms as given in Eq. (1-2):

$$X_C = S_X X_A \rightarrow \begin{bmatrix} x & y & z & \theta_x & \theta_y & \theta_z \end{bmatrix}^T = S_X \begin{bmatrix} x_{1p} & x_{2p} & x_{3p} & x_{1z} & x_{2z} & x_{3z} \end{bmatrix}^T \quad \textbf{(1-2)}$$

$$F_A = S_F^{-1} X_C \quad \textbf{(1-3)}$$

$$X_A = S_X^{-1} X_C \quad \textbf{(1-4)}$$

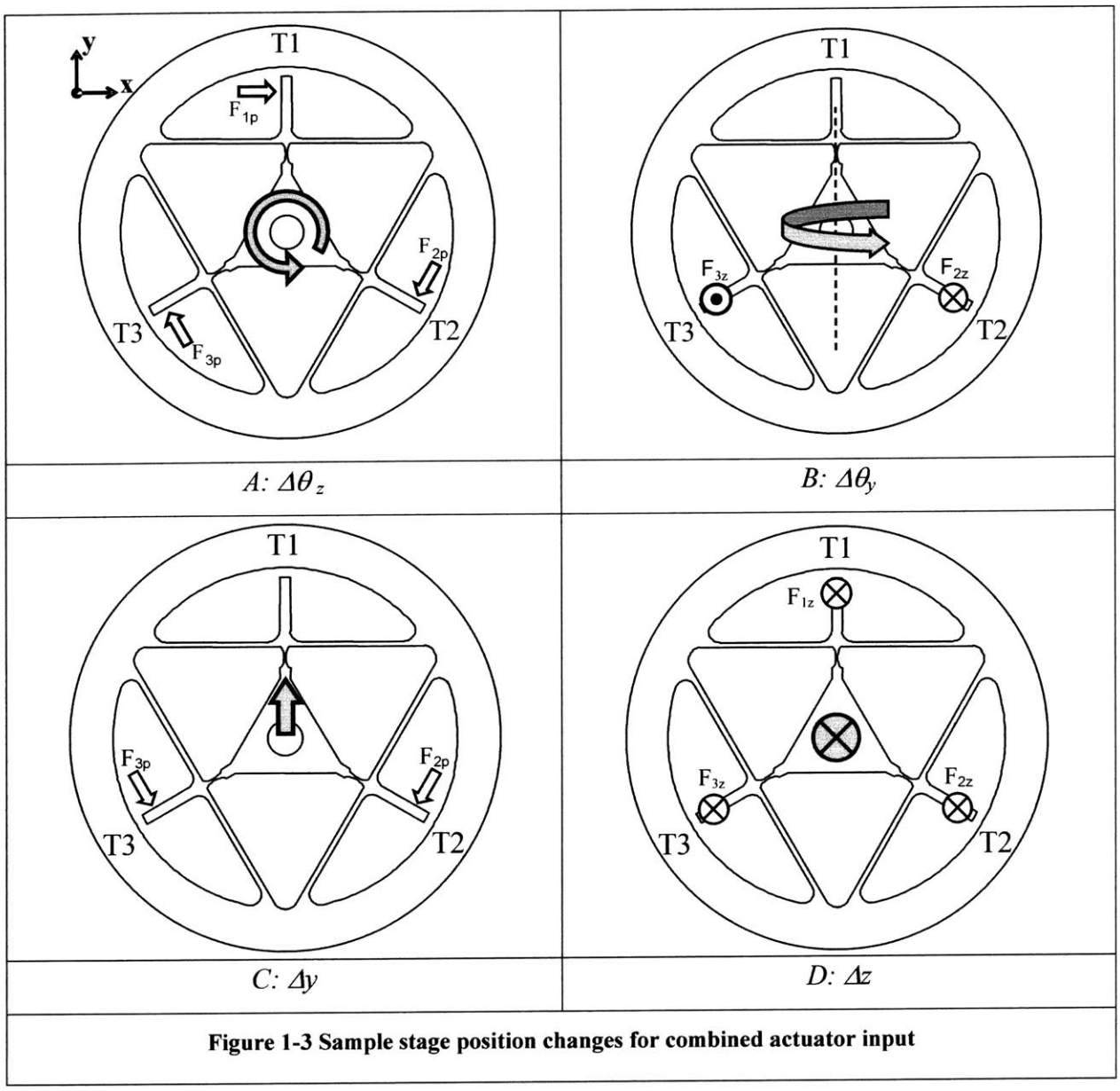


**Figure 1-3 Sample stage position changes for combined actuator input**

## 1.3 Fundamental Issues

The monolithic, planar Hexflex design provides a unique solution to the following cost-performance issues.

- Stability- The equilateral arrangement of symmetric constraints (e.g. supports) and low out-of-plane profile make the structure insensitive to thermal expansion errors.
- Machine structure and envelope – The planar nature of the structure enables tighter packaging than three dimensional compliant structures.
- Manufacturing – The planar geometry is easily fabricated using low-cost manufacturing processes such as EDM, stamping, abrasive waterjet and deep reactive ion etching.

With a functional actuation scheme, the Hexflex will become the first six degree of freedom planar positioning system, radically different from existing devices. The objective of this work is devising such an actuation system. Generally there are tradeoffs involved.

- Which actuation systems offer the best range to accuracy ratio?
- How should the in-plane and out-of-plane actuation systems be decoupled?

Chapter 2 provides background information on the types of precision actuators available. Chapter 3 uses this background information for the selection of a suitable actuator and documents the analysis procedure. The results of displacement, repeatability, impact and drift tests are recorded in Chapter 4. Chapter 5 discusses a fiber alignment case study. The insights gained from the testing are presented in Chapter 6.

# Chapter 2 Background

## 2.1 Flexure Systems

When the work envelope is less than about 10% of the size of the positioning device, flexures can be used in place of conventional bearings. Slocum [10] and Smith [11] have identified the following key elements regarding their application:

**Advantages**

- Wear free. No sliding motion is present between interfaces. Performance should not degrade with use, provided there is no fretting.
- Frictionless. Flexures have no static or dynamic friction. Resolution is not limited by "stiction", rather it is limited to the level of hysteresis in the material itself.
- Low part count. Manufacturing flexural motion stages as monolithic structures reduces part count, eliminates assembly alignment errors, and allows for increased miniaturization
- Vibration and shock resistance. Unlike conventional bearing systems, flexures are not affected by vibration and shock loads provided the elastic limits of the material are not exceeded.
- No maintenance
- Low cost

**Disadvantages**

- Low range of motion. Monolithic flexures have a range of motion to flexure size of 1:100. This ratio can be reduced to 1:10 with clamped flat spring bearings.

- Displacement uncertainty. Displacement due to a given force depends on the elastic modulus ($E$) of the flexure material. Published values of $E$ are generally accurate to only 1%, necessitating custom calibration.
- Low out-of-plane stiffness. In comparison to conventional bearing systems, the out-of-plane stiffness is low and the stiffness in the drive direction high – leading to large sensitivities to drive misalignment
- Low damping. Flexures generally have negligible damping, making them prone to extended oscillations. Elastomeric dampers can, however, be bonded to flexural surfaces.
- Hysteresis. Hysteresis errors arise from dislocation movement in the flexure material.
- Sensitivity to overloading. Plastic deformation from overloading will change the device characteristics, necessitating recalibration.
- Thermal sensitivity. The low volume to surface area ratio makes flexures sensitive to temperature fluctuations. These fluctuations affect geometry and the elastic modulus.
- Low stiffness. The larger the range of motion, the lower the stiffness.

## 2.2 Actuator Technology

A brief account of candidate actuators follows. The information presented here is used in the actuator selection process of Chapter 3.2.

**Piezo Actuators**

Presently the most popular high precision actuation technique, piezo actuation, relies on the dimensional change of a crystal when exposed to an electric field. Ranges are typically 0 -200 μm, but it is their high bandwidth and sub-nanometer resolution which make them so attractive. Slocum [10] notes that these actuators only dissipate power on the milliwatt level (which reduces the effect of thermal distortion) but can generate forces up to several kilonewtons. Although depolarization can be a problem, solid state operation exhibits no wear and tear with lifetimes of several billion cycles. Piezo

actuators offer unrivalled response time (microsecond time constants). Accelerations of more than 10 000 g can be obtained.

All crystalline materials can be divided into 32 different classes, 21 of which lack a center of symmetry. Of the asymmetric crystals, 20 exhibit piezoelectricity. It is this asymmetry which gives rise to the piezoelectric phenomenon - the generation of an electrical charge proportional to an applied mechanical stress and, conversely, a dimensional change proportional to an applied electric field.

Furthermore, there exist 10 classes of piezoelectrics which generate electrical charges when uniformly heated, an effect known as pyroelectricity. The unit cells of pyroelectric crystals are dipoles.

In the ferroelectric subgroup of pyroelectrics, the orientation of the dipoles can be changed by the application of an electric field. They can be permanently polarized by exposure to a large potential. The material is first sintered into the correct shape as a ceramic and then polarized. The polarization causes permanent orientation of dipoles in the direction of polarization. The ceramic will now respond to an applied electric field and mechanical pressure.

The elastic and electrical properties of piezoelectric materials are coupled. Gallego-Juarez [12] gives the following relations.

For the electric domain:

$$q = \in \mathscr{E} \qquad \textbf{(2-1)}$$

$q$ – dielectric displacement

$\in$ – permittivity of the medium

$\mathscr{E}$ – electric field strength

In the mechanical domain:

$$\varepsilon = c\sigma \qquad (2\text{-}2)$$

$\varepsilon$ – strain

$c$ - compliance

$\sigma$ - stress

The piezoelectric interaction between the domains is described by the following relations:

$$q = \mathrm{d}\sigma + {}^{\sigma}\in \mathscr{E} \qquad (2\text{-}3)$$

$$\varepsilon = {}^{\mathscr{E}}c\sigma + \mathrm{d}\mathscr{E} \qquad (2\text{-}4)$$

Where the superscripts denote the quantity kept constant for the evaluation. For example the constants ${}^{\sigma}\in$ and ${}^{\varepsilon}\in$ are the permittivities at constant stress (with the piezoelectric elements free) and constant strain (with the piezoelectric element clamped) respectively. The form of the equations depends on the choice of independent variables. There are four possible combinations yielding four pairs of equations.

$$q_m = \mathrm{d}_{\mathrm{mi}}\sigma_i + {}^{\sigma}\in_{mk} \mathscr{E}_k \qquad (2\text{-}5)$$

$$\varepsilon_i = {}^{\mathscr{E}}c_{ij}\sigma_j + \mathrm{d}_{\mathrm{mi}}\mathscr{E}_m \qquad (2\text{-}6)$$

$$q_m = \mathrm{e}_{\mathrm{mi}}\varepsilon_i + {}^{\varepsilon}\in_{mk} \mathscr{E}_k \qquad (2\text{-}7)$$

$$\sigma_i = {}^{\mathscr{E}}k_{ij}\varepsilon_j - \mathrm{e}_{mi}\mathscr{E}_m \qquad (2\text{-}8)$$

$$\mathscr{E}_m = -\mathrm{g}_{\mathrm{mi}}\sigma_i + {}^{\sigma}\beta_{mk}q_k \qquad (2\text{-}9)$$

$$\varepsilon_i = {}^{q}c_{ij}\sigma_j + g_{mi}q_m \qquad (2\text{-}10)$$

$$\mathscr{E}_m = -h_{\mathrm{mi}}\varepsilon_i + {}^{\varepsilon}\beta_{mk}q_k \qquad (2\text{-}11)$$

$$\sigma_i = {}^{q}k_{ij}\varepsilon_j - h_{mi}q_m \qquad (2\text{-}12)$$

The piezoelectric constants *d, e, g, h* are defined by:

$$d = \left(\frac{\partial q}{\partial \sigma}\right)_{\mathscr{E}} = \left(\frac{\partial \varepsilon}{\partial \mathscr{E}}\right)_{\sigma} \quad \textbf{(2-13)}$$

$$e = \left(\frac{\partial q}{\partial \varepsilon}\right)_{\mathscr{E}} = -\left(\frac{\partial \sigma}{\partial \mathscr{E}}\right)_{\varepsilon} \quad \textbf{(2-14)}$$

$$g = -\left(\frac{\partial \mathscr{E}}{\partial \sigma}\right)_{q} = \left(\frac{\partial \varepsilon}{\partial q}\right)_{\sigma} \quad \textbf{(2-15)}$$

$$h = -\left(\frac{\partial \mathscr{E}}{\partial \varepsilon}\right)_{q} = -\left(\frac{\partial \sigma}{\partial q}\right)_{\varepsilon} \quad \textbf{(2-16)}$$

The set of equations specific to piezoelectric ceramics are given below. In this case the material exhibits piezoelectric properties only in the direction of polarization.

$$q_1 = {}^{\sigma}\in_{11} \mathscr{E}_1 + d_{15}\sigma_5 \quad \textbf{(2-17)}$$

$$q_2 = {}^{\sigma}\in_{11} \mathscr{E}_2 + d_{15}\sigma_4 \quad \textbf{(2-18)}$$

$$q_3 = {}^{\sigma}\in_{33} \mathscr{E}_3 + d_{31}(\sigma_1 + \sigma_2) + d_{33}\sigma_3 \quad \textbf{(2-19)}$$

$$\varepsilon_1 = {}^{\mathscr{E}}c_{11}\sigma_1 + {}^{\mathscr{E}}c_{12}\sigma_2 + {}^{\mathscr{E}}c_{13}\sigma_3 + d_{31}\mathscr{E}_3 \quad \textbf{(2-20)}$$

$$\varepsilon_2 = {}^{\mathscr{E}}c_{11}\sigma_2 + {}^{\mathscr{E}}c_{12}\sigma_1 + {}^{\mathscr{E}}c_{13}\sigma_3 + d_{31}\mathscr{E}_3 \quad \textbf{(2-21)}$$

$$\varepsilon_3 = {}^{\mathscr{E}}c_{13}(\sigma_1 + \sigma_2) + {}^{\mathscr{E}}c_{33}\sigma_3 + d_{33}\mathscr{E}_3 \quad \textbf{(2-22)}$$

$$\varepsilon_4 = {}^{\mathscr{E}}c_{44}\sigma_4 + d_{15}\mathscr{E}_2 \quad \textbf{(2-23)}$$

$$\varepsilon_5 = {}^{\mathscr{E}}c_{44}\sigma_5 + d_{15}\mathscr{E}_1 \quad \textbf{(2-24)}$$

The subscripts 1,2 and 3 correspond to orthogonal axes. Subscripts 4,5 and 6 denote planes normal to the 1, 2 and 3 axes respectively.

The electromechanical coupling factor ($k$) relates the ability of the piezoelectric element to transduce energy from the electrical to the mechanical domain and vice versa.

$k_1^2$ **= electrical energy generated / mechanical energy applied** **(2-25)**

$k_2^2$ **= mechanical energy generated / electrical energy applied** **(2-26)**

Values of the piezoelectric strain constant, $d$, which relates the applied electric field to displacement are very low, ranging from $2.3 \times 10^{-12}$ to $290 \times 10^{-12}$ m/V. For the ceramic lead titanate zirconate (PZT) $d = 190 \times 10^{-12}$m/V. A 1mm high cylinder of the material will experience a 190 pm displacement when a potential of 1V is applied across its ends.

To increase the output displacement for a given input voltage, stack actuators (see Figure 2-1) have been developed. The piezoelectric material is layered between electrodes of alternating polarity. An alternative approach is the bimorph shown in Figure 2-2.

Even with these enhancements the range may still be insufficient. Compliant structures are frequently used to amplify the motion of the piezoelectric elements as shown in Figure 2-3.

For larger motions the Inchworm® has been developed. A piezo electric actuator is positioned on either side of a rail. Pairs of electrostatic clamps are mounted at both ends. One pair clamps to the rail, fixing an end of the piezo. The piezo then expands and the other pair of clamps is activated. The first pair is then released allowing the piezo to contract freely. By repetition of the process, the device creeps forward like a caterpillar. Actuators with traverses in excess of 100mm are available with step sizes below 20nm. Variations of the Inchworm exist where the electrostatic clamps have been replaced with a piezo actuated variety.

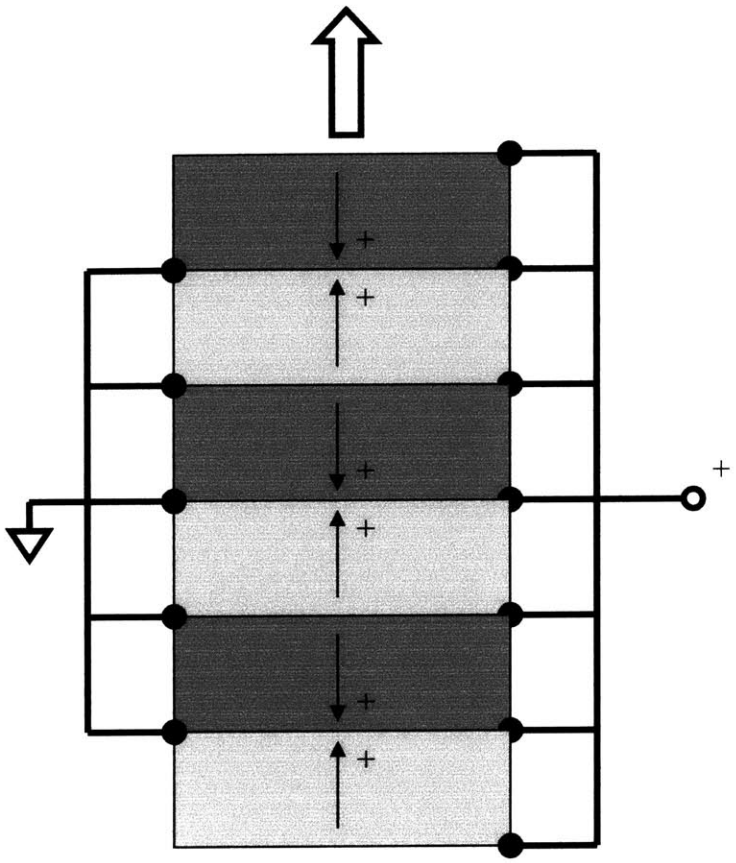


**Figure 2-1 Stack actuator schematic**

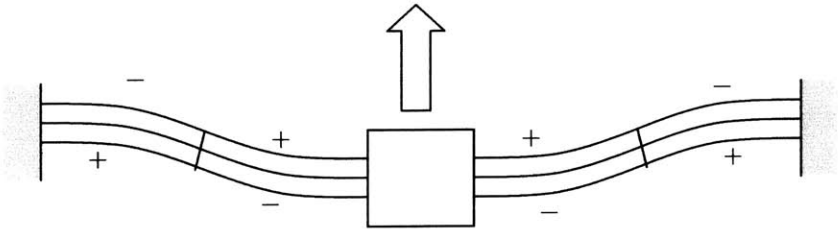


**Figure 2-2 Bimorph actuator**

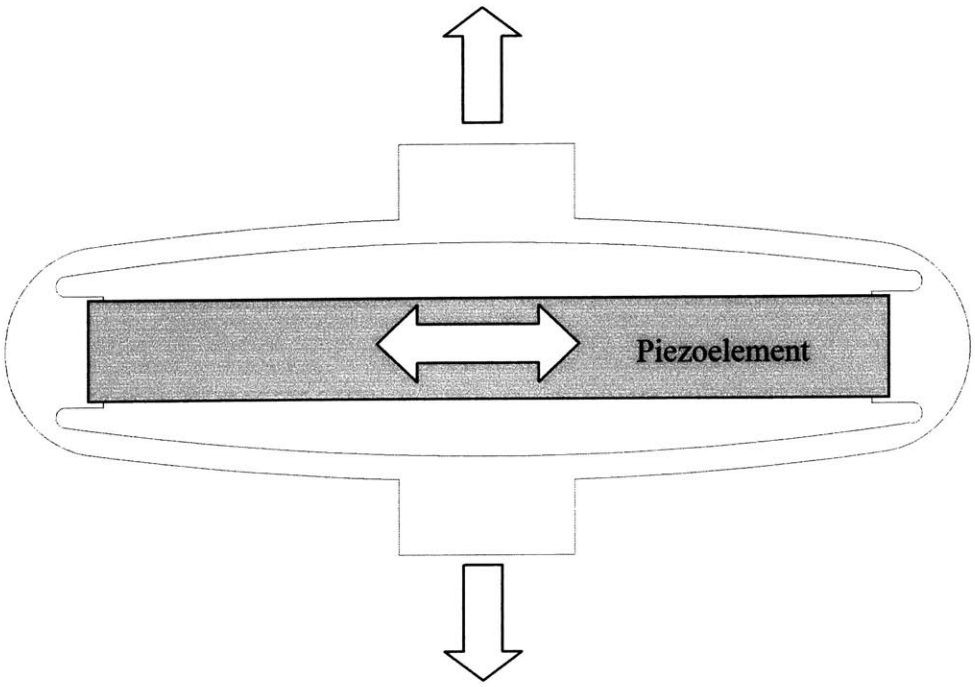


**Figure 2-3 Actuator with mechanical amplifier**

**Micrometers**

These provide an economic alternative in applications which can tolerate limited resolution. Figure 3-1 on page 59 shows that micrometers have a favorable range to accuracy ratio; however, in applications where absolute accuracy is critical, they may prove inadequate.

Micrometers display hysteresis and are prone to backlash. They are temperature sensitive due to their all-metal construction from alloys with relatively high thermal expansion coefficients. Open loop, micrometers may be accurate to within 1μm [11]. Differential micrometers with counter-moving threads can be manually positioned to 0.1μm, although their range is limited. Feedback control, which can correct for the pitch errors in the screw, allows this value to be reduced to 0.01μm [11].

Hatheway [13] has demonstrated that using compliant structures to scale the motion of the micrometer, angstrom level repeatability can be achieved over a range of a few nanometers. His series of *Angstrom Precision Actuators*™ have range to resolution ratios of 1000 and reduction ratios of up to 2 540 000. For example model *1000-1/100* has a resolution of 0.010nm and a range of 10nm.

**Friction Drives**

There are two classes of friction drive. The first, a capstan drive, relies on clamping friction; the second behaves like a vibratory feeder, using a series of impulses to momentarily overcome friction forces on the carriage.

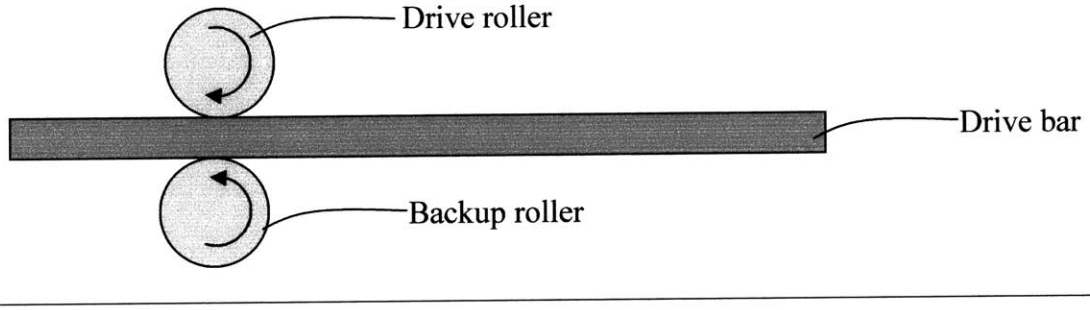


**Figure 2-4 Capstan drive**

The most common example of the first type consists of a bar squeezed between two preloaded rollers. The preload is used to raise the frictional force between the bar and rollers. In such a device, backlash is eliminated, although hysteresis errors are present. It is caused by the finite slip present at the roller/drive rod interface and at the bearings of the rollers themselves. A study by Weck and Bispink [14] determined values for the friction drive hysteresis to be between 0.1 and 0.05μm. With feedback position control the resolution of the drive was on the order of 10nm.

The advantages of a capstan drive include low frictional losses and zero backlash, while its detriments are sensitivity to drive bar cleanliness, low drive force capability, moderate stiffness and damping and a limited transmission ratio.

A fine surface finish on the contacting faces is necessary to minimize wear and improve repeatability. Inaccuracies in the circularity of the rollers and spacing of the working faces of the drive rod will cause variations in the preload, thus affecting the transmission ratio.

In the second class of friction drives a carriage is placed on a sprung slideway. An impulse applied to the slideway causes relative slip between itself and the carriage. A series of impulses can be used to translate the carriage with nanometer level resolution and velocities up to 0.2 mm/s for 1 kg carriages [14]. The stiffness of the system is low and depends entirely on the frictional forces holding the carriage in place on the slideway.

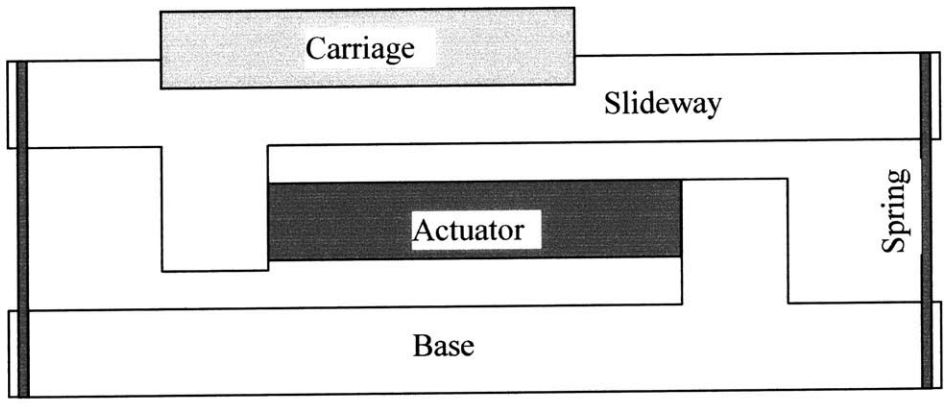


**Figure 2-5 Dynamic linear spring actuator**

**Magnetostriction**

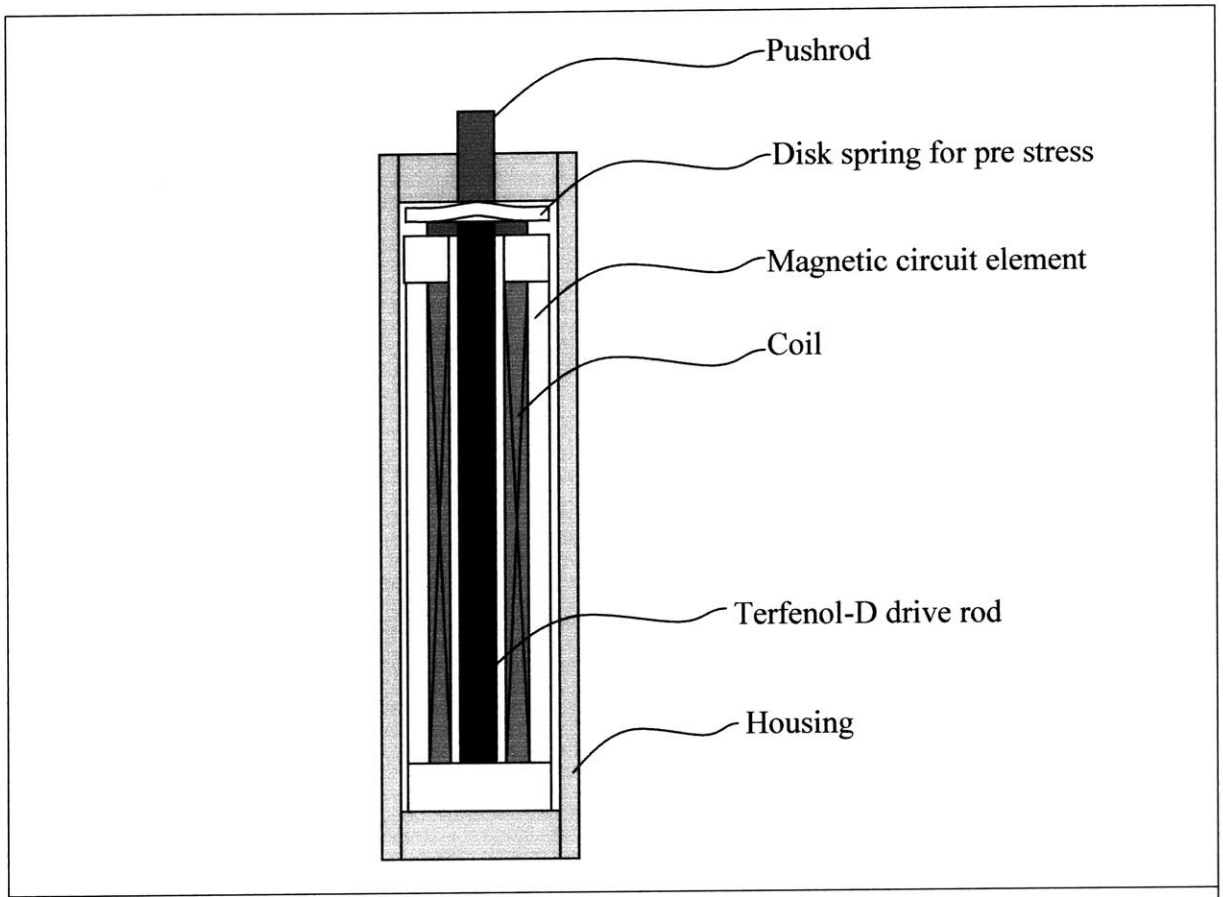


**Figure 2-6 Magnetostrictive actuator schematic**

Magnetostrictive materials undergo a positive strain in the presence of a magnetic field. The rotation of small magnetic domains results in expansion in the direction of the magnetic field. As the field is increased, more domains become aligned until saturation. If the field is reversed, the domains also reverse but the strains still cause an expansion in the field direction.

The material *Terfenol-D*, an alloy of terbium, dysprosium and iron displays the greatest magentostrictive effect of commercially available materials.

The material approaches its expansion limit when subject to an applied stress of 20 MPa and a magnetic field strength of $70kAm^{-1}$. Strains on the order of 2000 x $10^{-6}$ are produced. At zero pre-stress the strain at the same field strength is approximately half of the 20MPa value. For this reason most magnetostrictive actuators are preloaded. In addition permanent magnets are used to create a bias field which partially expands the *Terfenol-D* into the middle of its operating region. The actuator can now be driven in both directions with reduced current requirements from the drive electronics. The heat generated by the coil can reduce the repeatability of the actuator.

Actuators currently available through *Etrema Inc.*[15], the sole supplier of *Terfenol-D*, provide about half the displacement output of equivalent size piezo stack actuators.

**Table 2-1 Comparison of commercial magnetostrictive and piezo actuators**

| **Manufacturer** | **Etrema** | **Piezojena** | **Etrema** | **Piezojena** | **Etrema** | **Piezojena** |
|---|---|---|---|---|---|---|
| **Model** | AA 050H | PA 25/12 | AA 090J | PAHL 40/20 | AA 140H | PAHL 80/20 |
| **Length** | 100 mm | 44 mm | 170 mm | 54 mm | 220 mm | 90 mm |
| **Diameter** | 31.8 mm | 12 mm | 47.0 mm | 20 mm | 47.0 mm | 20 mm |
| **Price** (July 2002) | $745 | $399 | $1165 | $1076 | $1540 | $1873 |
| **Max Displacement** | 25µm | 25µm | 45µm | 40µm | 70µm | 80µm |
| **Max Load** | 462N | 1000N | 1680N | 3500N | 1740N | 3500N |
| **Bandwidth** | 3kHz | 12kHz | 1.25kHz | 16kHz | 3kHz | 12kHz |

The table above shows the three basic actuator types available from *Etrema Inc.* together with the closest equivalent piezo actuators from *Piezojena Inc.*[16]. It is evident that piezo actuators offer superior displacement and load carrying performance per unit cost.

The chief advantage of magnetostrictive actuators is their ability to withstand elevated temperature making them suitable for aeronautical and automotive applications. Piezoactuators are permanently depolarized by exposure to high temperature, whereas magnetostrictive actuators can withstand continuous cycling through their Curie point.

**Magnetoelastic Actuators**

Magnetic fields not only produce strains by reorientation of domains in materials, but also by changing the modulus of elasticity. The magnetoelastic effect refers to the change in elastic modulus brought about by the exposure of material to a magnetic field. Consequently displacements are only produced if the material is preloaded.

From the equation

$$\varepsilon = \frac{\sigma}{E} \qquad \textbf{(2-27)}$$

$\sigma$ = stress

$E$ = elastic modulus

It is easy to see that the strain is proportional to the preload and inversely proportional to the elastic modulus.

For constant preload the incremental strain ($\Delta\varepsilon$) due to $\Delta E$ is given by

$$\Delta\varepsilon \approx \varepsilon_o \frac{\Delta E}{E} \qquad \textbf{(2-28)}$$

$\varepsilon_o$ = initial strain due to preload

Since the maximum strain for most materials is in the region of 0.1% and the maximum change in modulus is 2 -10%, the maximum change in length of a 100mm magnetoelastic actuator is 2 to 10 μm compared to 50 μm for a similarly sized piezoactuator.

Materials with a low thermal expansion coefficient and near zero thermoelastic coefficients are desirable.

Magnetoelastic materials are highly non-linear and exhibit considerable hysteresis making closed loop position control a necessity.

**Shape Memory Alloys**

Alloys which exhibit one way shape memory have the ability to transform to a pre-defined shape upon heating. Two-way shape memory alloys undergo a shape change upon both heating and cooling.

When a shape memory alloy is plastically deformed below the martensitic transformation temperature it will regain its original shape upon heating to the austenite phase. In most cases the effect is one-way so the alloy will not change shape upon cooling from an austenite structure to martensite.

Two-way behavior can be created by the introduction of internal stresses which create preferential directions for martensitic grain formation during cooling. The potential for shape change during cooling is less than that during heating so the forces the cooling alloy can exert are lower.

It is the nickel-titanium and copper-base alloys which are the most popular commercially because they generate the largest strains and forces. The former is capable of producing shape memory strains up to 8.5%, while copper-base alloys exhibit strain recoveries of 4%.

Because the shape memory transformation is gradual, occurring over a temperature range, shape memory actuators do not have to be binary. Positioning is possible to within 0.1mm over a range of 20mm [11].

Yaeger [17] has demonstrated a 100mm cantilever shape memory actuator with a deflection of 20mm, a drive force of 300N, and a 4s time constant. Jebens [18] has demonstrated shape memory positioning of optical fibers to within 100nm. Unfortunately the heat used to control the actuator may cause unacceptable thermal distortion in a precision device.

## Electromagnetic Actuators

*Solenoid*

The most basic of electromagnetic actuators, the solenoid, uses an electromagnet to attract an iron component.

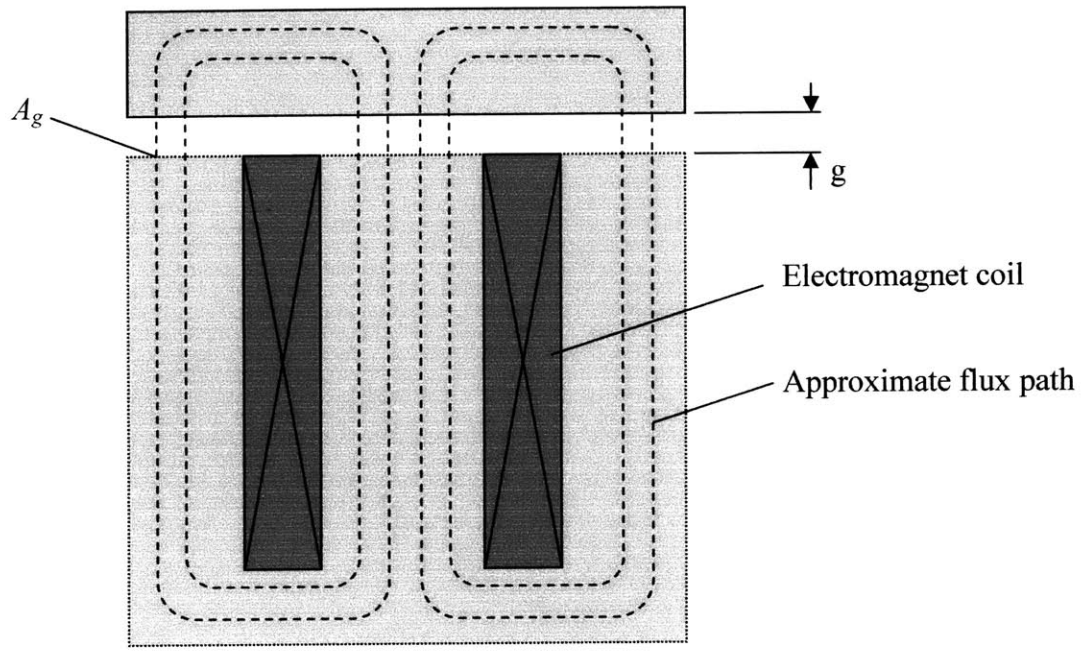


**Figure 2-7 Basic solenoid actuator**

The attractive force ($F$) between the solenoid coil and the moving magnetic member is given by the following relation:

$$F \approx \frac{\mu_o N^2 I^2 A_g}{2g^2} \qquad \textbf{(2-29)}$$

$\mu_o$ = magnetic permeability of air

$N$ = number of turns in the coil

$A_g$ = pole area

$I$ = current

g = separation distance

The non-linearity of the force response is evident - proportional to the square of the current and inversely proportional to the square of the separation distance. Solenoids may present control difficulties from positive feedback where an increase in force leads to a decrease in separation distance which in turn causes an increase in force.

*Magnet-coil Actuators*

Magnet-coil actuators have the following characteristics:

- linear operation over a relatively long range
- low hysteresis
- direct electrical control (as opposed to a lead screw or friction drive)
- no mechanical linkage between actuator and stage
- low stiffness actuator minimizes cross axis forces, accommodates misalignment and reduces vibration transmission
- self centering

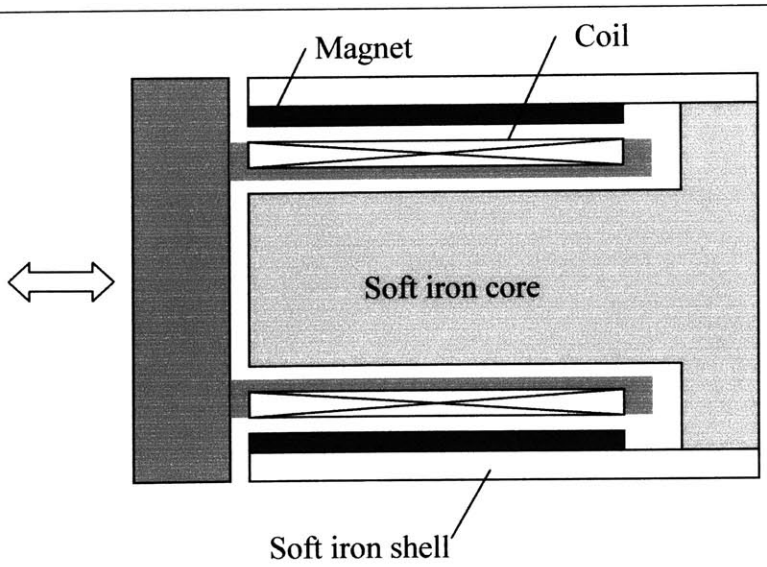


**Figure 2-8 Moving coil actuator [10]**

There are two main categories: moving coil/fixed magnet and moving magnet/fixed coil. In the first category a fixed permanent magnet is used to create a magnetic field in a narrow air gap in which the driven conductor coil is positioned. The force on the coil is given by the equation [10].

$$F = ILB \tag{2-30}$$

$B$ = magnetic flux density

$L$ = length of conductor in field

The magnetic flux can be estimated from the following equation [10]:

$$B \approx \sqrt{\frac{\mu_o H_m B_m V_m}{V_g}} \tag{2-31}$$

$H_m B_m$ = energy product for the magnetic material

$V_m$ = magnet volume

$V_g$ = coil gap volume

It is evident that gap volume should be minimized and magnet volume maximized for optimum force generation.

Unfortunately heat generated by the passage of current through the coil can introduce thermal errors to the stage. These may be mitigated by the use of two counter wound coils. The coils are energized with equal bias currents when the stage is at the origin. Motion occurs when current in one coil is increased at the expense of the other such that the combined heat generation remains constant. The redundant coil increases stage mass and coil gap volume thus degrading system performance. Alternatively a moving magnet device can be employed.

In moving magnet actuators the coil is bonded to the base and surrounds the permanent magnet on the mobile platform. The force generated is [19]:

$$F_z \approx \frac{B_{rem} A}{\mu_0}\left[B_{z0}(z_m + b_m) - B_{z0}(z_m - b_m)\right] \quad \textbf{(2-32)}$$

$B_{rem}$ = remnance of permanent magnet

$B_{z0}$ = magnetic flux density

$A$= cross sectional area of magnet

Such an actuator is constructed by fixing a series of disc type magnets to a linear spring. The coil is then positioned over the magnets. The maximum force is generated at the ends of the coil where the magnetic field gradient is highest.

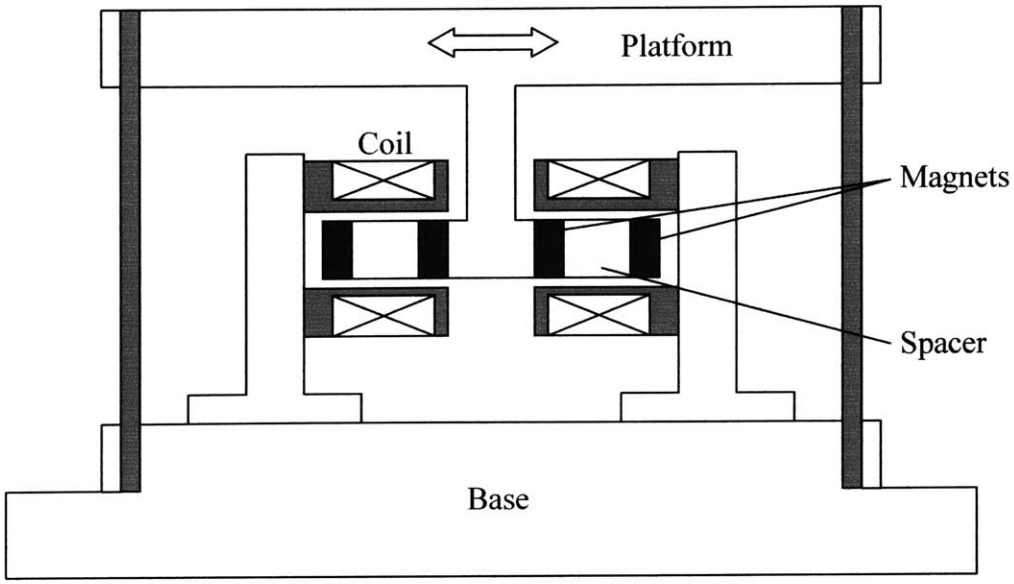


**Figure 2-9 Linear spring with a four-magnet, two-coil actuator [19]**

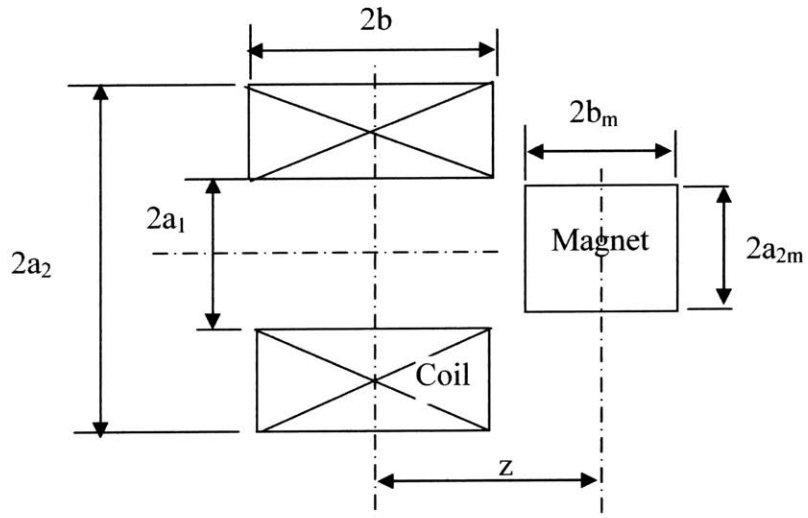


**Figure 2-10 Magnet coil nomenclature**

The equations governing coil design are as follows

$$R = \frac{\pi\rho(\alpha+1)N^2}{a_1\lambda(\alpha-1)2\beta} \quad \textbf{(2-33)}$$

$$L = a_1^2 R\lambda\frac{\phi(\alpha,\beta)}{\rho} \quad \textbf{(2-34)}$$

$R$ = resistance

$L$ = inductance

$\lambda$ = coil packing factor ( $\approx$ 0.77 [20])

$\phi$ = geometry factor

$\rho$ = resistivity of winding material

$\alpha = a_2/a_1$ [dimensionless]

$\beta = b/a_1$ [dimensionless]

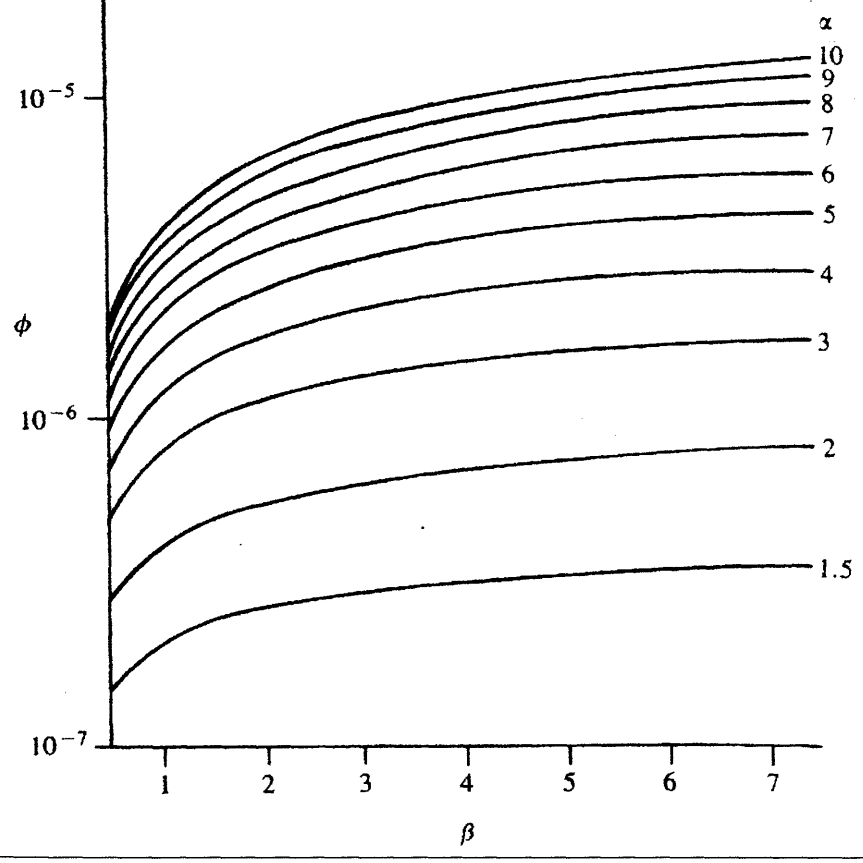


**Figure 2-11 Geometry factor for a uniformly wound cylindrical coil [19]**

The magnetic field [20] along the coil axis inside the coil $z < a_1\beta$ is:

$$B_{z0}(z) = \frac{\mu_0 NI}{4a_1\beta(\alpha-1)}\left[f(\alpha,\beta+z/a_1)+f(\alpha,\beta-z/a_1)\right] \quad \textbf{(2-35)}$$

for the magnetic field along the coil axis outside the coil $z > a_1\beta$

$$B_{z0}(z) = \frac{\mu_0 NI}{4a_1\beta(\alpha-1)}\left[f(\alpha,\beta+z/a_1)-f(\alpha,z/a_1-\beta)\right] \quad \textbf{(2-36)}$$

The function $f(\alpha,\nu)$ is defined as

$$f(\alpha,\nu) = \nu \ln\left[\frac{\alpha+\left(\alpha^2+\nu^2\right)^{1/2}}{1+\left(1+\nu^2\right)^{1/2}}\right] \quad \textbf{(2-37)}$$

Where high bandwidth is critical, moving coil actuators are employed. For example, the common loudspeaker is a moving coil actuator offering exceptional performance with a 20kHz bandwidth and a 500μm range.

**Electrostatic Actuators**

The solenoid relation:

$$F \approx \frac{\mu_o N^2 A_g I^2}{2g^2} \quad \textbf{(2-38)}$$

bears a close resemblance to the force of attraction between two rectangular flat electrodes in a parallel plate capacitor:

$$F = \frac{\varepsilon A V^2}{2g^2} \quad \textbf{(2-39)}$$

$\varepsilon$ = permittivity of the gap

$A$ = overlapping area of the plates

$g$ = separation distance

$V$= potential difference across plates

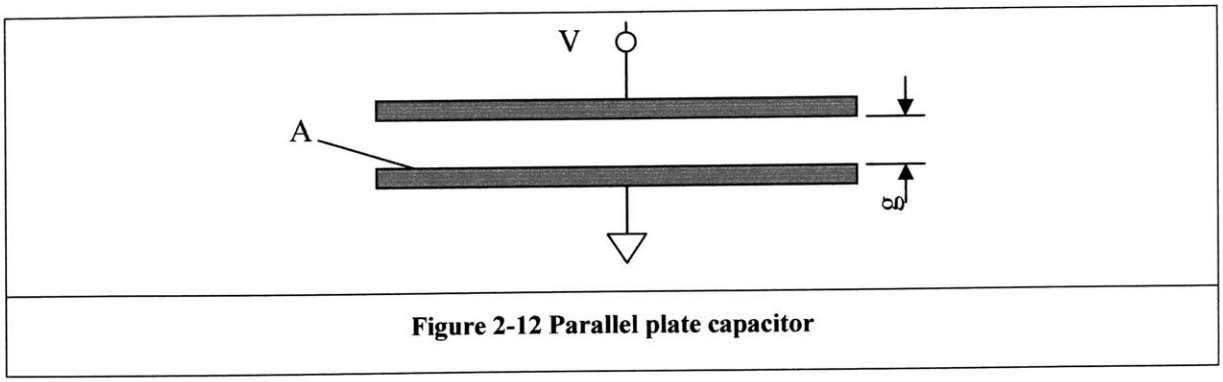


**Figure 2-12 Parallel plate capacitor**

In contrast to the magnet coil actuator where the attractive force increased with magnet volume, electrostatic actuators become more effective as dimensions are reduced. Micro- and nano-scale devices are suitable candidates.

The inverse square relationship between force and separation distance is the determining factor. A device operating in air with the following parameter values

$A = 100\text{mm}^2$

$g = 1\text{mm}$

$V = 100\text{V}$

yields a micro-scale attractive force of $4.25 \times 10^{-6}\text{N}$. As the gap is reduced to 0.01mm the force increases by a factor of $10^4$ to $4.25 \times 10^{-2}\text{N}$.

Smith [11] notes that the electrostatic force relation in equation 2-36 is exact and extends over many orders of magnitude, limited only by the stability of the dielectric between the two plates. The permittivity of air is very sensitive to temperature and humidity, so vacuum conditions are preferable.

**Hydraulic Actuators**

For motion ranges of several meters, hydraulic cylinders are used. These have rods which are displaced by the introduction of fluid into the cylinder. The fluid flow is controlled by servo-valves. Micron resolution can be obtained if the system is properly equipped with Teflon seals and hydrostatic bearings to support the piston and rod in the cylinder.

Single acting cylinders apply force in only one direction and require gravity or some other external load for return motion. Double acting cylinders can be used for actuation in both directions, although the differing areas over which the hydraulic fluid acts results in different load capacities for the forward and reverse direction.

Metal bellows actuators provide precision over limited motion ranges. Maximum displacements are typically on the order of 1mm and resolution is sub micron. The configuration in Figure 2-13 utilizes a lead screw actuator to compress a small diameter, large length master bellows which is turn transmits fluid to a large diameter, small length slave bellows. The slave extends a fraction of the lead screw actuator displacement.

Hydraulic systems rely on a primary pressure/flow source. In the bellows example below the lead screw actuator and small diameter bellows act as a flow source. For hydraulic cylinders a pump and servo valve are used. These additional elements add complexity and maintenance requirements, unlike magnetostrictive, piezo and magneto-coil actuators which can be driven directly by an electrical signal.

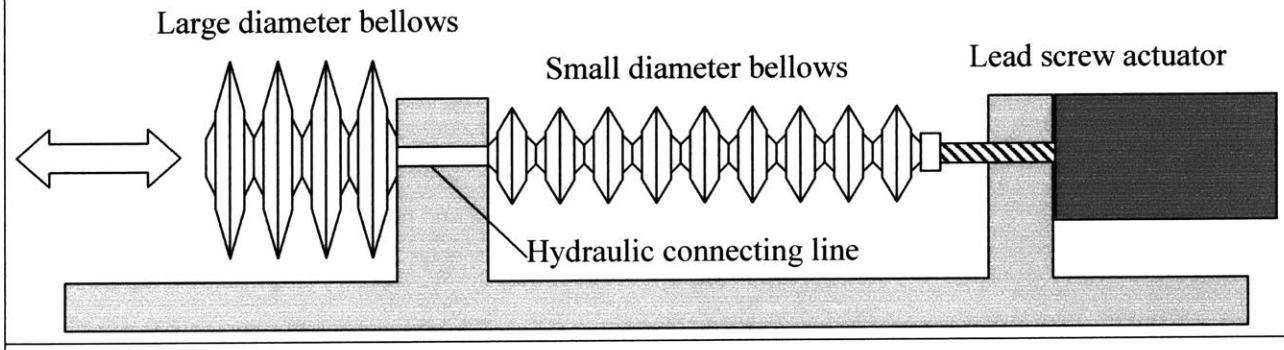


**Figure 2-13 Bellows actuator system (adapted from Slocum [10] )**

Smith [11] observes that most commercial systems are only capable of operating at frequencies of a few Hertz, so high bandwidth applications are not favored. Hydraulic systems are used where their high stiffness and large force per unit size can be exploited.

**Poisson Ratio Drives**

As the name suggests these actuators use the Poisson effect (see equation below) to generate axial strains in a shaft from an applied radial pressure.

$$\varepsilon_x = \frac{\sigma_x - \nu(\sigma_y + \sigma_z)}{E} \quad \textbf{(2-40)}$$

$\varepsilon_x$ = strain along x axis

$E$ = Young's modulus

$\nu$ = Poisson's ratio

$\sigma_x$ = applied stress along x axis

$\sigma_y$ = applied stress along y axis

$\sigma_z$ = applied stress along z axis

Typically the shaft is bored out to form a cylinder whose walls are exposed to a radial hydrostatic pressure. Micron level displacements and stiffnesses on the order of 10GN/m are typical. A variant using a C clamp arrangement to stress a solid shaft has been successfully tested by Jones [21] in positioning a flexural stage to within 1nm.

# Chapter 3 Design

## *3.1 Requirement Specification*

| Table 3-1: Design requirements for the six-axis nano-manipulator | |
|---|---|
| Coarse work volume for Micro-manipulation | 100μm x 100μm x 100μm |
| Fine work volume for nano-manipulation | 100 nm x 100 nm x 100 nm |
| Resolution | < 5 nm |
| Repeatability | 5nm |
| Open loop accuracy: micro-manipulation | 150 nm |
| Start-up drift | < than 100 nm over 30 minutes |

## 3.2 Concept Selection Process

Characterizing actuators is difficult due to the wide range present, and the significant variation within each type of actuator. Nevertheless Figure 3-1 provides an overview of range vs. accuracy for the actuators under consideration.

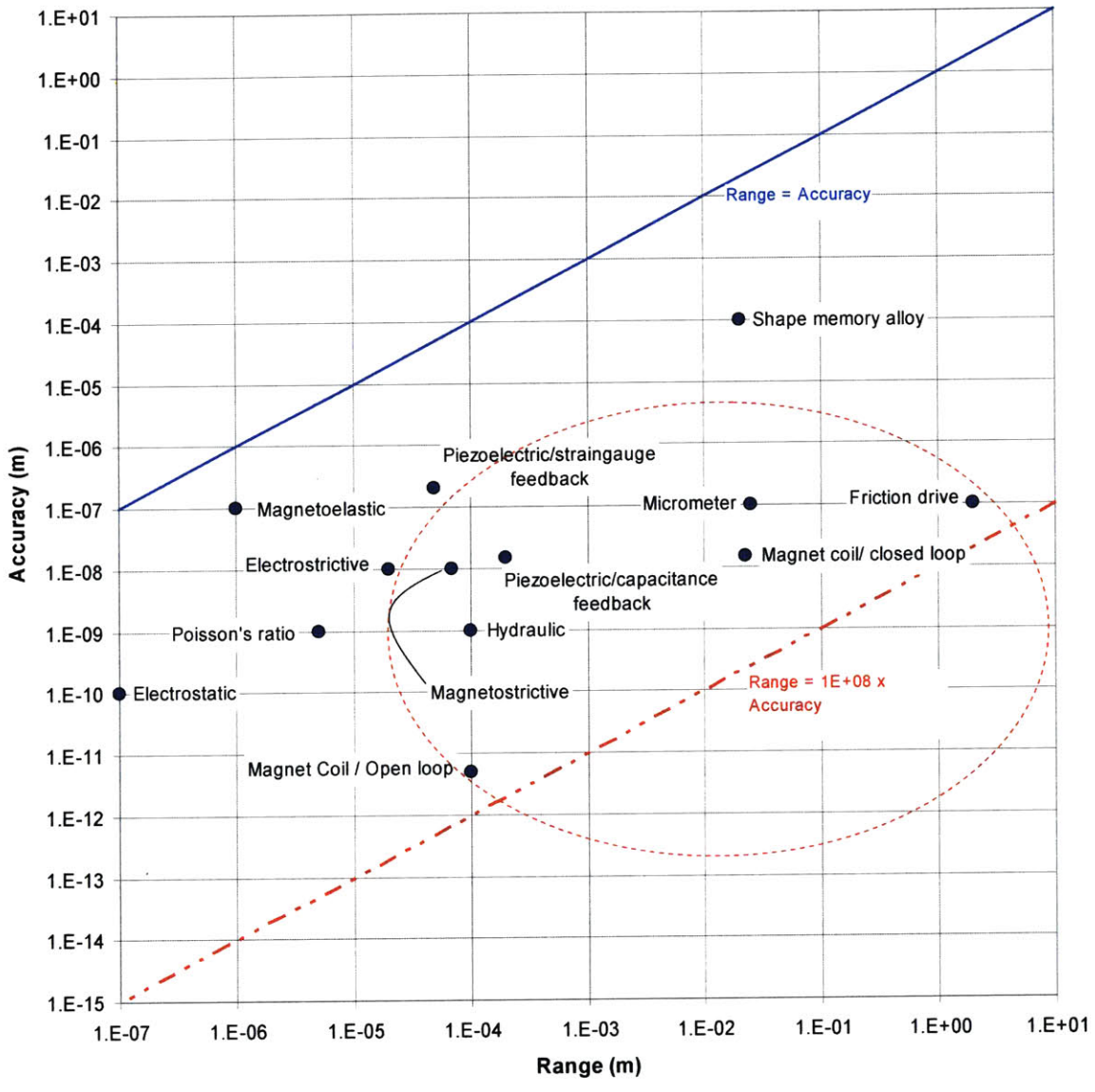


**Figure 3-1 Actuator range vs. accuracy**

The region within the dotted boundary contains possible Hexflex actuator candidates. The electrostatic and Poisson actuators were excluded because their ranges were insufficient. The actuators closest to the lower (dashed) diagonal posses the greatest range: accuracy ratio. The chart shows that the friction drive and magnet coil are the most attractive is this regard.

The selection criteria follow:

**Cost**

- A relatively low cost micrometer actuator can be assembled from a micrometer head, stepper motor and flexural coupling for under $250 [27].
- Hydraulic actuators require a pressure or flow source and high pressure seals making them potentially the most costly actuator. Estimated price is over ~ $1000 per actuator.
- An 80 μm range piezo element costs on the order of $700 [15].
- Although a magnet-coil actuator would have to be custom manufactured, it is anticipated that the cost per unit will be below $500.
- Magnetostrictive actuators are available from *Etrema Inc* – price for a 70μm device is $1500 [16].
- Friction drives are more complicated, requiring at a minimum a direct drive servomotor, drive rollers/capstan and a drive rod or cable. Cost is estimated at well over $1000 per unit. Intuitively, a friction drive (with its long range capability) does not match a small range of motion flexure.

**Accuracy**

For actuators under closed loop positional control, the accuracy limit is generally determined by the feedback positioning sensor which is on the order of 10nm for capacitive sensors. The maximum accuracies given for the magnet-coil (under closed loop control for long range), electrostrictive and piezo actuator in Figure 3-1 are so

governed. Magnet-coil actuators can achieve the extreme accuracy of 0.01nm when operated open loop for ranges less than 100μm [11].

**Range**

The Hexflex is designed with centroid output to actuator input ratios of less than one, which establishes a lower bound on actuator range on the order of 100 μm (equal to the working range). Slocum's[10] criterion of monolithic flexure motion being at best 1/100 of the overall length can be used to provide an order of magnitude estimate on the upper bound of usable actuator range. The characteristic dimension of the Hexflex is 150mm, so the order of magnitude of the upper range bound is 1.5 mm.

**Stiffness**

In the case of the Hexflex, a large actuator stiffness will decrease the sensitivity of the centroid position to disturbance forces.

**Disturbance Generation**

Resistive heat losses of the electromagnetic actuator are a possible disturbance source. The shape memory actuator has similar problems. Piezo and magnetostrictive actuators are benign.

**Compatibility with Hexflex (mounting)**

Coupling the actuator to the Hexflex tab poses a problem. The actuator is to impose tab displacement along a singe axis, while not restraining motion along the two orthogonal axes perpendicular to the drive direction. Three possible attachment configurations have been identified.

*Sphere and flat.* In the configuration shown in Figure 3-2 balls are fixed to the flexure at the contact point of the flat head of the piezo actuator. Problems with this design include the compliance in the direction of drive so that the displacement of the actuator does not match the displacement of the tab. Any surface irregularities or debris on the flat will create error motions as the ball slides over the flat on the piezo head. In addition, the frictional force between a ball and contact pad of one actuator while the other is driven gives rise to undesirable forces and moments in the system.

*Flexural Coupling.* Attaching the actuator to the tabs by flexural links in Figure 3-3 solves some of the problems of the ball on flat coupling, but the non zero stiffness of the flexures perpendicular to the direction of actuation will change the input-output transmission ratios. The flexures will introduce a new source of manufacturing error which may lead to additional parasitic motions. The flexural links violate the "planar flexure" principle of the Hexflex, unless they can somehow be incorporated into the planar tabs themselves.

*Non contact electromagnetic field coupling.* Figure 3-4 shows non-contact coupling between actuator and tab with zero transverse stiffness. Cross talk between in-plane and out-of-plane actuators will be a minimum. The low effective stiffness of the unit accommodates misalignment errors between the tab and actuator without introducing parasitic motion to the extent of the "ball and flat" or "flexural link".

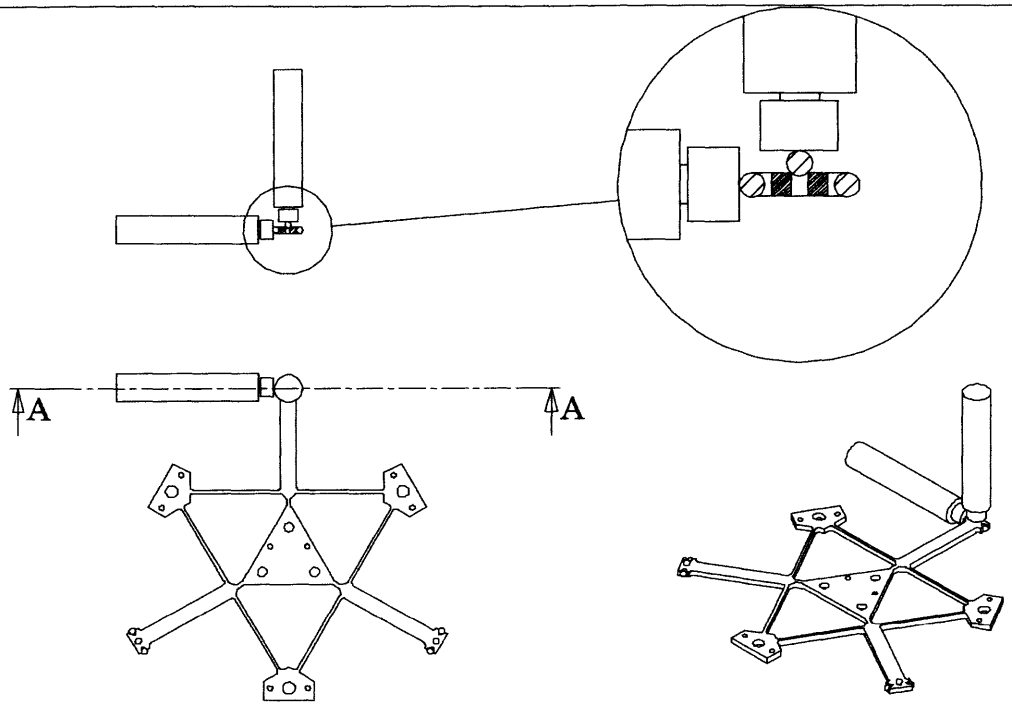


**Figure 3-2 Sphere and flat coupling**

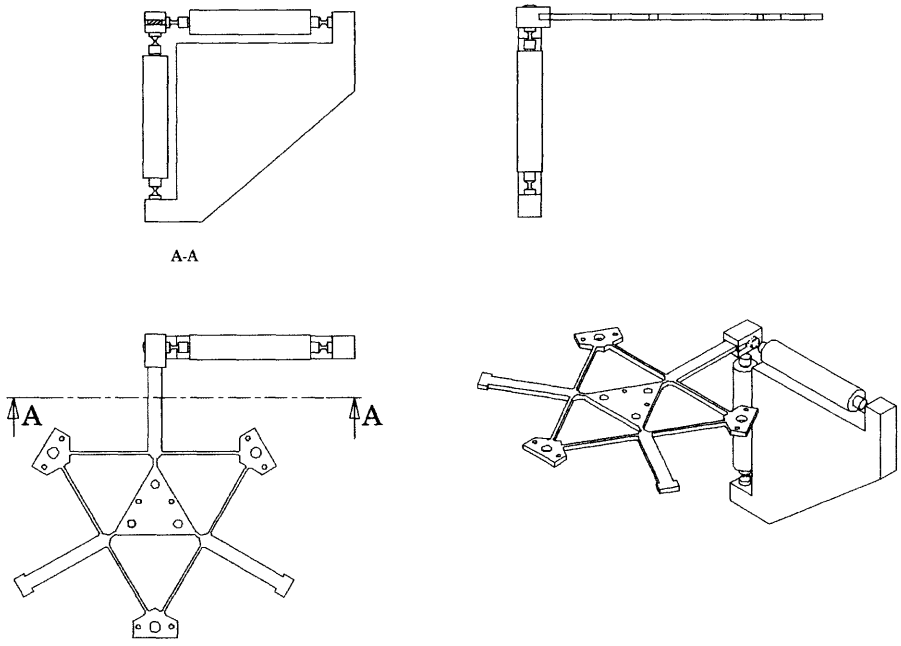


**Figure 3-3 Flexural joint coupling**

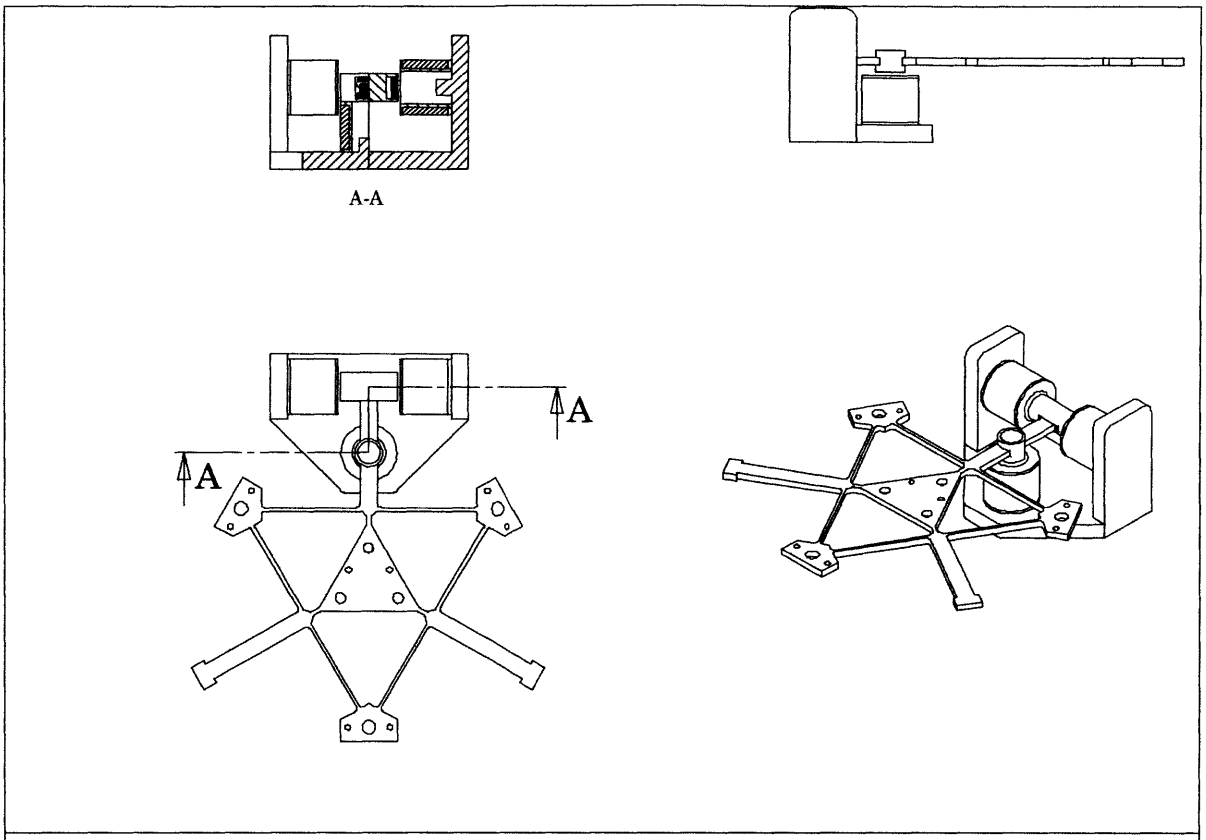


**Figure 3-4 Electromagnetic field coupling**

**Table 3-2 Actuator attribute summary**

| | **Piezoelectric** | **Electromagnetic** | **Hydraulic** |
|---|---|---|---|
| **Cost** | $700 | <$500 | >$1000 |
| **Accuracy** | Determined by feedback sensor ~ 0.010μm | If determined by feedback sensor ~ 0.010μm. Open loop accuracy may be has low as 0.01nm | 0.001μm |
| **Range** | 80 μm | 20 000μm | 100μm |
| **Stiffness** | High | Low | Very high |
| **Compatibility** | Requires flexural connection to actuator tab | Non contact, requires no physical connection, accommodating of motion perpendicular to drive | Requires flexural connection to actuator tab |
| **Disturbance generation** | Excellent | Poor | Moderate |

| Table 3-2 Actuator attribute summary contd. | | | | |
|---|---|---|---|---|
| | **Friction Drive** | **Shape memory** | **Micrometer** | **Magnetostrictive** |
| **Cost** | >$1000 | <$100 | $250 | $1500 |
| **Accuracy** | 0.100μm | 100μm | 0.100μm | Determined by feedback sensor ~ 0.010μm |
| **Range** | 2 000 000μm | 20 000μm | 25 000μm | 70 μm |
| **Stiffness** | Moderate | High | Moderate | High |
| **Compatibility** | Difficult to implement two orthogonal actuators for driving the same tab | Requires flexural connection | Requires flexural, sliding ball contact | Requires flexural connection to actuator tab |
| **Disturbance generation** | Moderate | Very poor | Moderate | Excellent |

| Table 3-3 Actuator selection chart | | | | | | | | |
|---|---|---|---|---|---|---|---|---|
| | **Ranking** | **Piezo** | **Electro-magnetic** | **Hydraulic** | **Friction Drive** | **Shape memory** | **Micrometer** | **Magneto-strictive** |
| **Cost** | 1 | 0 | 0 | - | - | + | + | 0 |
| **Accuracy** | 3 | 0 | 0 | + | - | - | - | 0 |
| **Range** | 3 | - | + | - | + | + | + | - |
| **Stiffness** | 1 | + | - | + | 0 | + | + | + |
| **Compatibility** | 2 | - | + | - | - | - | - | - |
| **Disturbance generation** | 2 | + | - | - | 0 | - | 0 | + |
| **Total** | | -2 | 2 | -4 | -3 | -2 | 0 | -2 |

## 3.3 Analysis

### CoMeT

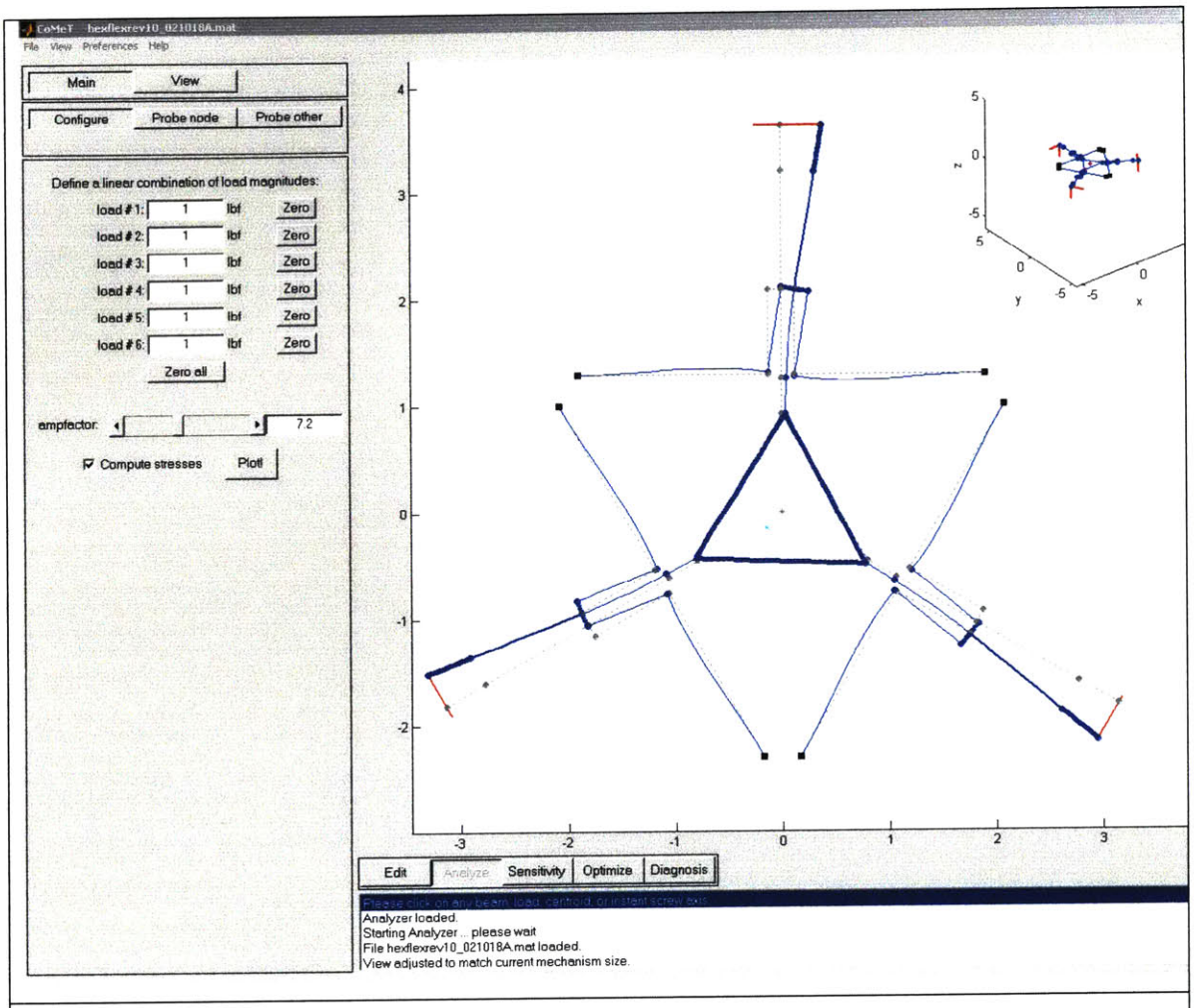


**Figure 3-5 Comet screen capture**

The necessary actuator force and displacements were determined by the $\mathbf{S_F}$ and $\mathbf{S_X}$ matrices from CoMeT. The matrices are consistent for units of microns, μradians, and N.

$$\mathbf{S_f} = \begin{bmatrix} 25.71 & -12.73 & -12.73 & 0 & 0 & 0 \\ 0 & -22.10 & 22.10 & 0 & 0 & 0 \\ 0 & 0 & 0 & 20.91 & 20.91 & 20.91 \\ 0 & 0 & 0 & 2022 & -1007 & -1007 \\ 0 & 0 & 0 & 0 & 1740 & -1740 \\ -477.2 & -477.2 & -477.2 & 0 & 0 & 0 \end{bmatrix} \quad (3\text{-}1)$$

$$\mathbf{S}_x = \begin{bmatrix} 0.0775 & -0.0385 & -0.0385 & 0 & 0 & 0 \\ 0.0001 & -0.0668 & 0.0669 & 0 & 0 & 0 \\ 0 & 0 & 0 & 0.0648 & 0.0645 & 0.0644 \\ 0 & 0 & 0 & 3.6732 & -1.8346 & -1.8346 \\ 0 & 0 & 0 & 0 & 3.1811 & -3.1772 \\ -1.2717 & -1.2717 & -1.2717 & 0 & 0 & 0 \end{bmatrix} \quad (3\text{-}2)$$

The required translation (in μm) is:

$$\mathbf{X_{C\_MAX}} = [50 \quad 50 \quad 50 \quad 0 \quad 0 \quad 0]^T \quad (3\text{-}3)$$

$F_{A\_MAX}$ gives the maximum actuator force (N):

$$\mathbf{F_{A\_MAX}} = \mathbf{S_F^{-1}X_{C\_MAX}} \quad (3\text{-}4)$$

$$\mathbf{F_{A\_MAX}} = [1.301 \quad -1.7816 \quad 0.4809 \quad 0.7950 \quad 0.7981 \quad 0.7981]^T$$

$X_{A\_MAX}$ gives the maximum tab displacement (μm):

$$\mathbf{X_{A\_MAX}} = \mathbf{S_X^{-1}X_{C\_MAX}} \quad (3\text{-}5)$$

$$\mathbf{X_{A\_MAX}} = [431.0 \quad -589.3 \quad 158.3 \quad 257.9 \quad 258.1 \quad 258.3]^T$$

From ( 3-4) and ( 3-5) the maximum actuator force is in the region of ±1.8N and the required range is ± 0.6mm.

**Actuator**

The magnet coil equations of section 2.2 are revisited.

The magnetic field along the coil axis inside the coil for $z < a_1\beta$ is

$$B_{z0}(z) = \frac{\mu_0 NI}{4a_1\beta(\alpha-1)}\left[f(\alpha,\beta+z/a_1)+f(\alpha,\beta-z/a_1)\right] \quad \textbf{(3-6)}$$

for the magnetic field along the coil axis outside the coil for $z > a_1\beta$ is

$$B_{z0}(z) = \frac{\mu_0 NI}{4a_1\beta(\alpha-1)}\left[f(\alpha,\beta+z/a_1)-f(\alpha,z/a_1-\beta)\right] \quad \textbf{(3-7)}$$

where

$$f(\alpha,\nu) = \nu \ln\left[\frac{\alpha+\left(\alpha^2+\nu^2\right)^{1/2}}{1+\left(1+\nu^2\right)^{1/2}}\right] \quad \textbf{(3-8)}$$

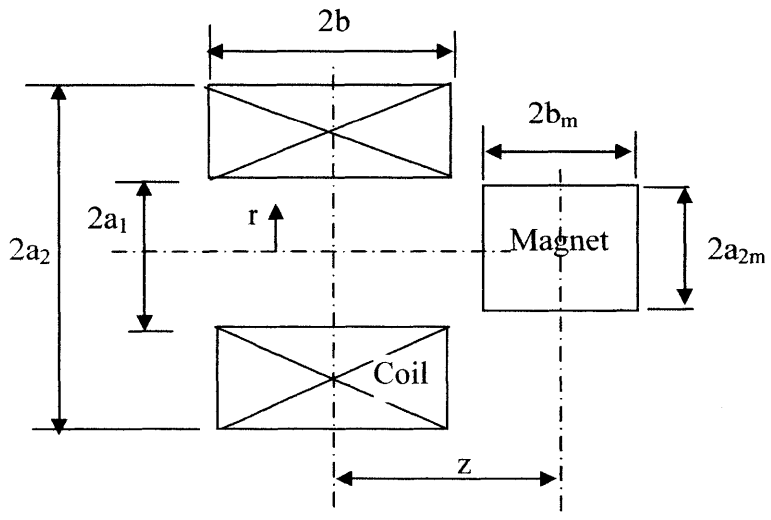


**Figure 3-6 Single-coil actuator**

The force on a magnet positioned between two coils may be evaluated by superposition. For convenience the origin is redefined as being between the two coils.

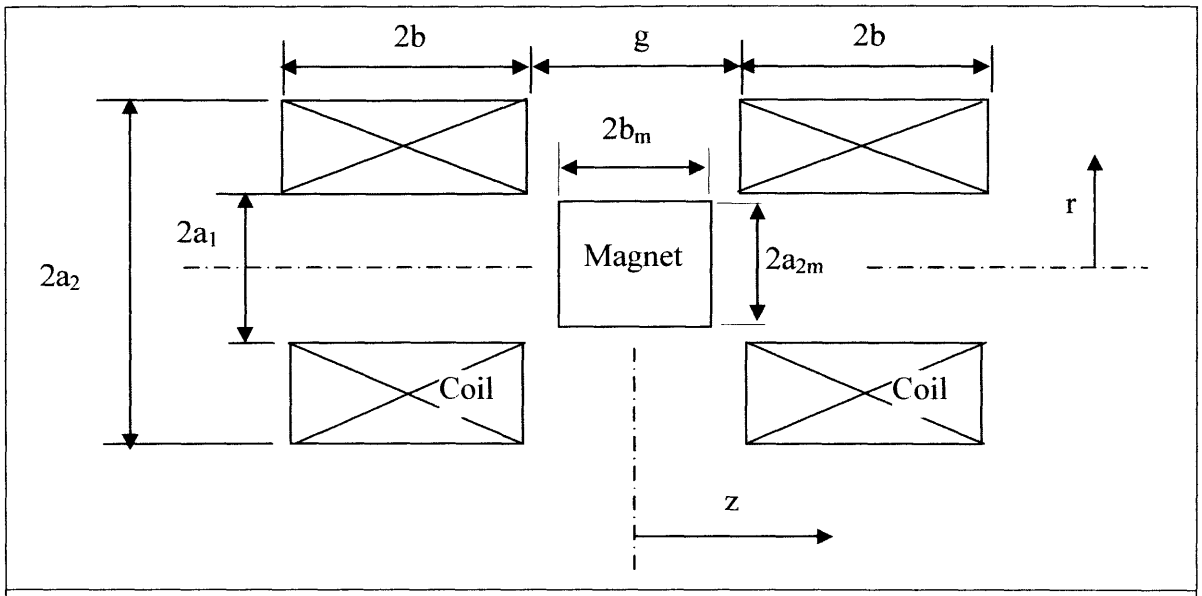


**Figure 3-7 Dual-coil actuator**

The magnetic flux density along the coil axis is:

for $|z| < g/2$ or $|z| > g/2 + 2\beta/a_1$

$$B_{z0}(z) = \frac{\mu_0 NI}{4a_1\beta(\alpha-1)}\left[ f(\alpha, 2\beta + g/2a_1 + z/a_1) - f(\alpha, 2\beta + g/2a_1 - z/a_1) \right. \quad \textbf{(3-9)}$$
$$\left. + f(\alpha, g/2a_1 - z/a_1) - f(\alpha, g/2a_1 + z/a_1) \right]$$

for $g/2 < |z| < g/2 + 2\beta/a_1$

$$B_{z0}(z) = \frac{\mu_0 NI}{4a_1\beta(\alpha-1)}\left[ f(\alpha, 2\beta + g/2a_1 + z/a_1) - f(\alpha, 2\beta + g/2a_1 - z/a_1) \right. \quad \textbf{(3-10)}$$
$$\left. - f(\alpha, -g/2a_1 + z/a_1) - f(\alpha, g/2a_1 + z/a_1) \right]$$

The force on an axially magnetized magnet is

$$F_z \approx \frac{B_{rem}A}{\mu_0}\left[B_{z0}(z_m + b_m) - B_{z0}(z_m - b_m)\right] \quad \textbf{(3-11)}$$

The flux density ($B_{z0}$) can also be expressed in terms of the coil geometry and power dissipation ($W$) instead of turns and current ($NI$). Substitution of Eqs (3-12) and (3-13)

with $W = 1$ into (3-11) yields the specific force ($f_z$) which is the force per unit power dissipation.

for $|z| < g/2$ or $|z| > g/2 + 2\beta/a_1$

$$B_{z0}(z) = \frac{\mu_0}{4}\sqrt{\frac{\lambda W}{\pi\rho a_1 \beta(\alpha^2-1)}}\left[ f(\alpha, 2\beta + g/2a_1 + z/a_1) - f(\alpha, 2\beta + g/2a_1 - z/a_1) \right. \quad \textbf{(3-12)}$$
$$\left. + f(\alpha, g/2a_1 - z/a_1) - f(\alpha, g/2a_1 + z/a_1) \right]$$

for $g/2 < |z| < g/2 + 2\beta/a_1$

$$B_{z0}(z) = \frac{\mu_0}{4}\sqrt{\frac{\lambda W}{\pi\rho a_1 \beta(\alpha^2-1)}}\left[ f(\alpha, 2\beta + g/2a_1 + z/a_1) - f(\alpha, 2\beta + g/2a_1 - z/a_1) \right. \quad \textbf{(3-13)}$$
$$\left. - f(\alpha, -g/2a_1 + z/a_1) - f(\alpha, g/2a_1 + z/a_1) \right]$$

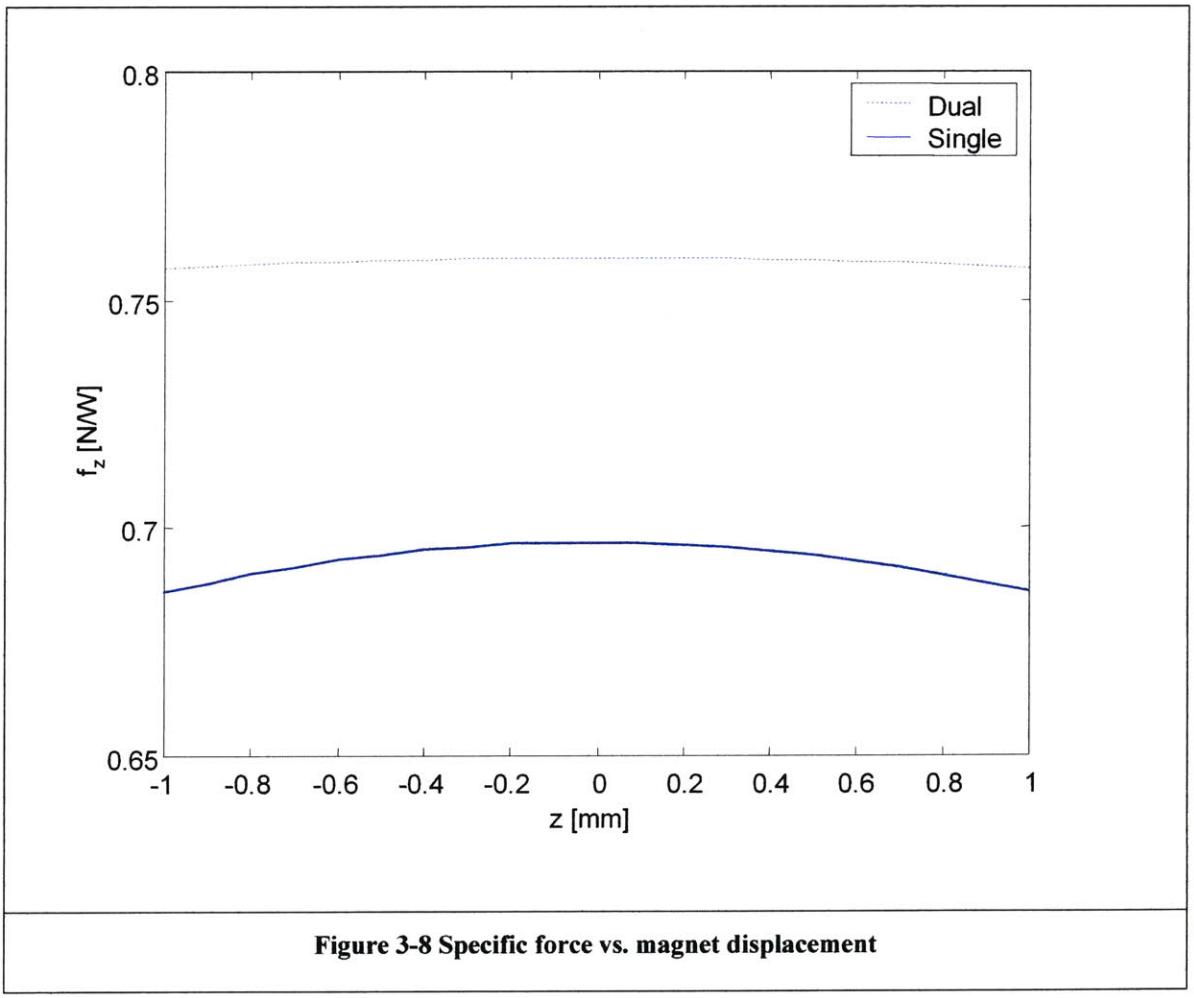


**Figure 3-8 Specific force vs. magnet displacement**

Figure 3-8 shows the dual-coil configuration to be superior both in terms of specific force and constancy of force over a wide displacement range. An actuator with a large specific force minimizes heat dissipation, while constancy of force over range reduces reliance on positional feedback and may make possible accurate 'open loop' operation. The following parameter values were used to generate the plot above:

$\alpha =$ 2.000

$a =$ 6.5 mm

$\beta =$ 0.800

$b_m =$ 6.35 mm

$a_{2m} =$ 4.76 mm

$B_{rem} =$ 1.23 T

$g =$ 14.1 mm

An analytic expression for the off-axis coil flux does not exist; nevertheless the components of the off axis magnet field must be determined so parasitic radial forces on the magnet can be calculated. In addition, determination of the off axis axial flux components will allow the actuator force to be more accurately predicted. The off-axis flux components ($B_r$ and $B_z$) can be determined by the application of the Biot Savart law in Eq. (3-14) to each loop of conductor as shown in Figure 3-9.

$$\vec{\mathbf{B}} = \frac{\mu_0}{4\pi}\int \frac{\vec{\mathbf{I}} \times \vec{\mathbf{r}}}{r^2} dl \qquad \textbf{(3-14)}$$

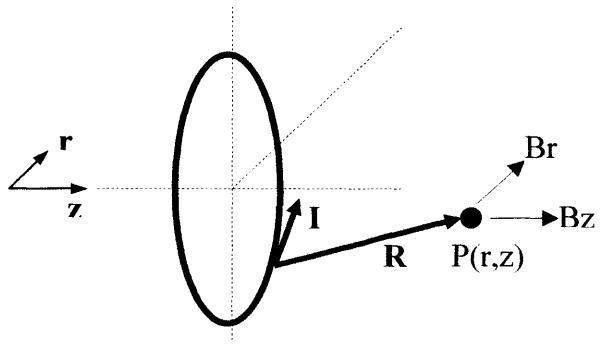


**Figure 3-9 Magnetic flux due to a current loop**

Computation of the integrals for each turn in a 500 turn solenoid coil is inefficient. Garret [22] has compiled a set of alternate elliptic integral equations which yield a faster solution.

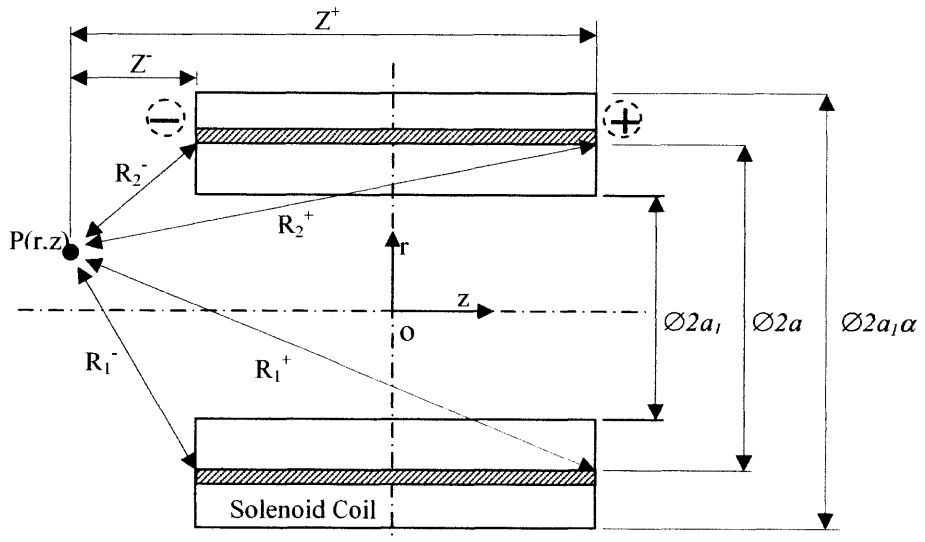


**Figure 3-10 Nomenclature for Garret's equations**

$$B_z(r,z) = B_z^+(r,z) - B_z^-(r,z) \quad \textbf{(3-15)}$$

$$B_z^+(r,z) = \frac{\pi NI \times 10^{-7}}{2a_1^2\beta(\alpha-1)} \int_{a_1}^{a_1\alpha} \frac{Z^+\left(2a+(a-r)\zeta^+_\infty\right)}{(r+a)R_1^+\Lambda^+_\infty} da \quad \textbf{(3-16)}$$

$$B_z^-(r,z) = \frac{\pi NI \times 10^{-7}}{2a_1^2\beta(\alpha-1)} \int_{a_1}^{a_1\alpha} \frac{Z^-\left(2a+(a-r)\zeta^-_\infty\right)}{(r+a)R_1^-\Lambda^-_\infty} da \quad \textbf{(3-17)}$$

$$B_r(r,z) = B_r^+(r,z) - B_r^-(r,z) \quad \textbf{(3-18)}$$

$$B_r^+(r,z) = \frac{\pi NI \times 10^{-7}}{4a_1^2\beta(\alpha-1)} \int_{a_1}^{a_1\alpha} \frac{R_1^+\zeta^+_\infty}{r\Lambda^+_\infty} da \quad \textbf{(3-19)}$$

$$B_r^-(r,z) = \frac{\pi NI \times 10^{-7}}{4a_1^2\beta(\alpha-1)} \int_{a_1}^{a_1\alpha} \frac{R_1^-\zeta^-_\infty}{r\Lambda^-_\infty} da \quad \textbf{(3-20)}$$

The superscripts "+" and "-" refer to values calculated relative to the far side "+" or the near side "-" of the solenoid coil.

$$R_2^{\,2} = (a-r)^2 + Z^2 \qquad \textbf{(3-21)}$$

$$k^2 = 4ar / R_1^{\,2} \qquad \textbf{(3-22)}$$

$$c^2 = 4ar/(a+r)^2 \qquad \textbf{(3-23)}$$

$$R_1^{\,2} = (a+r)^2 + Z^2 \qquad \textbf{(3-24)}$$

$$k'^2 = (R_2/R_1)^2 \qquad \textbf{(3-25)}$$

$$c'^2 = (a-r)^2/(a+r)^2 \qquad \textbf{(3-26)}$$

$\Lambda$ and $\zeta$ are determined by performing iterations of the following equations

$$\Lambda_{i+1} = 0.5(\Lambda_i + \mathrm{B}_i) \qquad \textbf{(3-27)}$$

$$\mathrm{B}_{i+1} = \sqrt{\Lambda_i \mathrm{B}_i} \qquad \textbf{(3-28)}$$

$$S_\infty = \sum_{i=0}^{\infty} 2^{i-1}(\alpha_i - \beta_i)^2 \qquad \textbf{(3-29)}$$

$$\delta_{i+1} = \frac{\mathrm{B}_{i+1}}{4\Lambda_{i+1}}(2 + \delta_i + 1/\delta_1) \qquad \textbf{(3-30)}$$

$$\varepsilon_{i+1} = \frac{\delta_i \varepsilon_i + \zeta_i}{1+\delta_i} \qquad \textbf{(3-31)}$$

$$\zeta_{i+1} = 0.5(\varepsilon_i + \zeta_i) \qquad \textbf{(3-32)}$$

with initial values:

$$\begin{aligned} \Lambda_0 &= 1 \\ \mathrm{B}_0 &= k' \\ \delta_0 &= c'^2/k' \\ \varepsilon_0 &= c^2/c'^2 \\ \zeta_0 &= 0 \end{aligned} \qquad \textbf{(3-33)}$$

The iterations ( 3-27) to ( 3-32) are continued until $\Lambda$ is indistinguishable from $\beta$ and $\delta$ from 1.

The axial and radial forces now follow. The term $z_m$ denotes the z-location of the magnet centroid. The variable for the radial position of each element on the magnet face is $a_m$.

$$F_z(r_m, z_m) = \frac{B_{rem}}{\mu_0} \int_0^{2\pi} \int_{a_{1m}}^{a_{m1}} [B_z(a_m, z_m + b_m) - B_z(a_m, z_m - b_m)]\, a_m\, da_m\, d\theta \qquad \textbf{(3-34)}$$

$$F_r(r_m, z_m) = \frac{B_{rem}}{\mu_0} \int_0^{2\pi} \int_{a_{1m}}^{a_{m1}} [B_r(a_m, z_m + b_m) - B_r(a_m, z_m - b_m)]\, a_m\, da_m\, d\theta \qquad \textbf{(3-35)}$$

**Optimization**

For a given magnet size (with $b_m$ = 12.7 mm and $a_{2m}$ = 4.76 mm) the optimum values of the following parameters need to be determined: $\alpha$, $a_1$, $\beta$ and $g$.

Figure 3-11 shows $f_z$, the maximum specific force from Eq. (3-11) for all $\alpha$ and $\beta$, plotted against $a_1$ and $g$. It is apparent that $f_z$ increases with decreasing clearance and $a_1$. Figure 3-12 depicts the percentage variation in $f_z$ over the actuator's ± 0.6mm operating range. The variation in $f_z$ has a minimum for certain $a_1/g$ combinations.

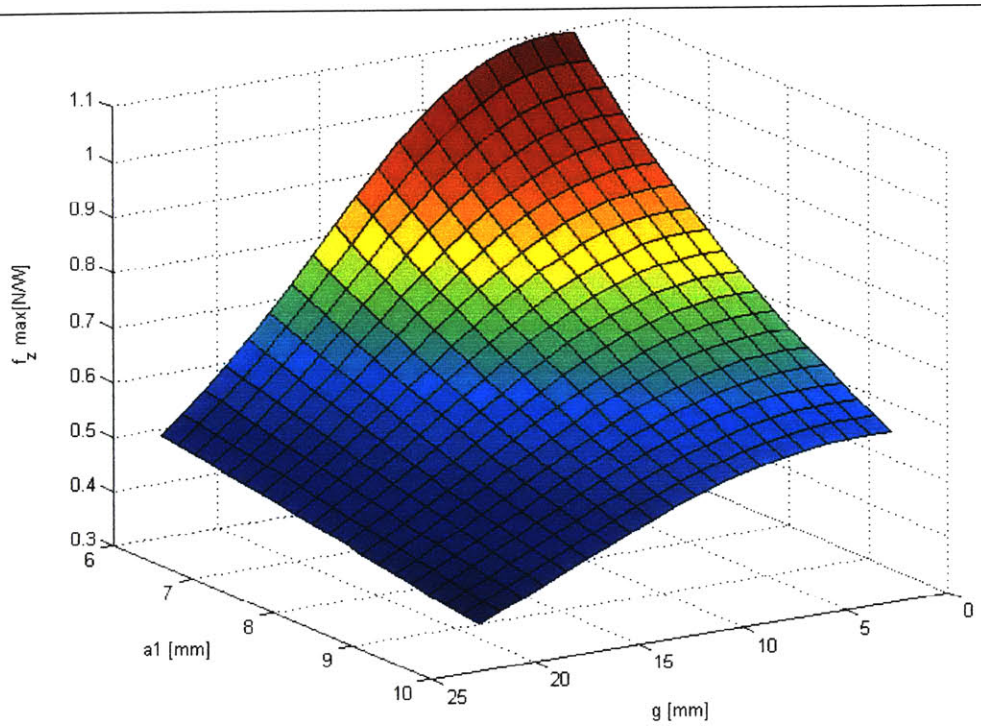


**Figure 3-11 Surface plot of $f_z$ vs. $a_1$ and $g$**

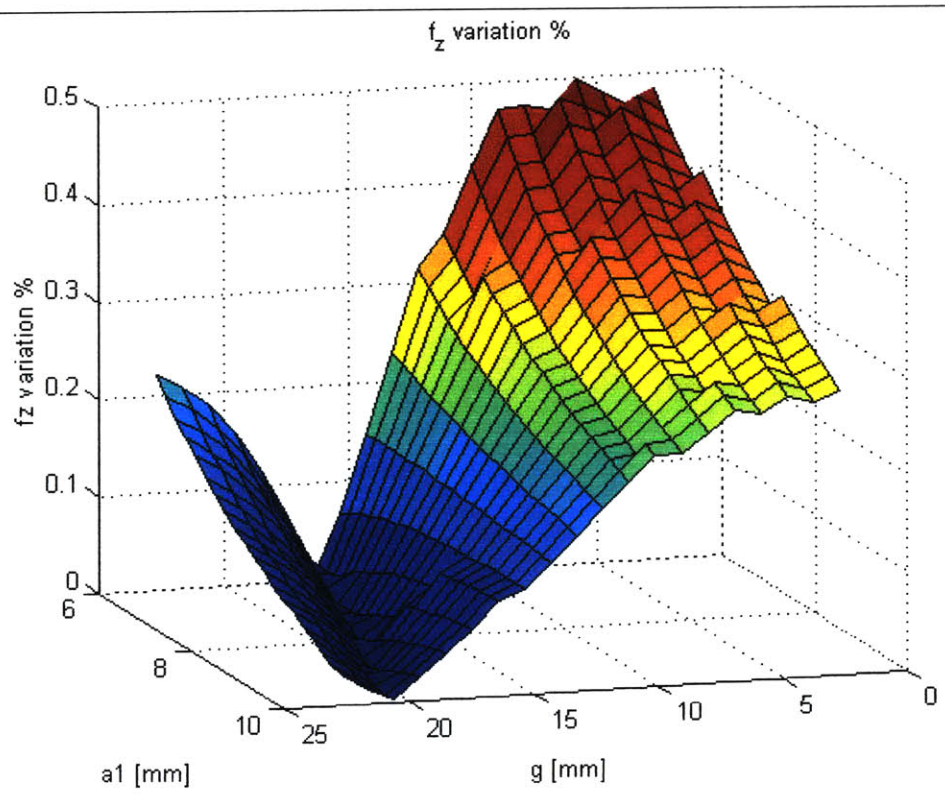


**Figure 3-12 Surface plot of variation in $f_z$ vs. $a_1$ and $g$**

Figure 3-11 and Figure 3-12 are used to select the $a_1$ / $g$ combination that results in an adequate specific force with near zero variation over the axial operating range. Allowances for the wall thickness of the mandrel and clearance between the mandrel ID and the magnet OD limits the minimum value of $a_1$ to 6.5mm. The corresponding coil separation ($g$) from Figure 3-12 which minimizes $f_z$ variation is 16mm.

Now for these values of $a_1$ and $g$, the corresponding values of $\alpha$ and $\beta$ for maximum $f_z$ were 2.38 and 0.723 respectively. The sensitivity of $f_z$ to variations in $\alpha$ and $\beta$ is shown in Figure 3-13. The surface plot shows that the diameter of the actuator can be reduced (i.e. $\alpha$ made smaller ) without an appreciable loss of performance.

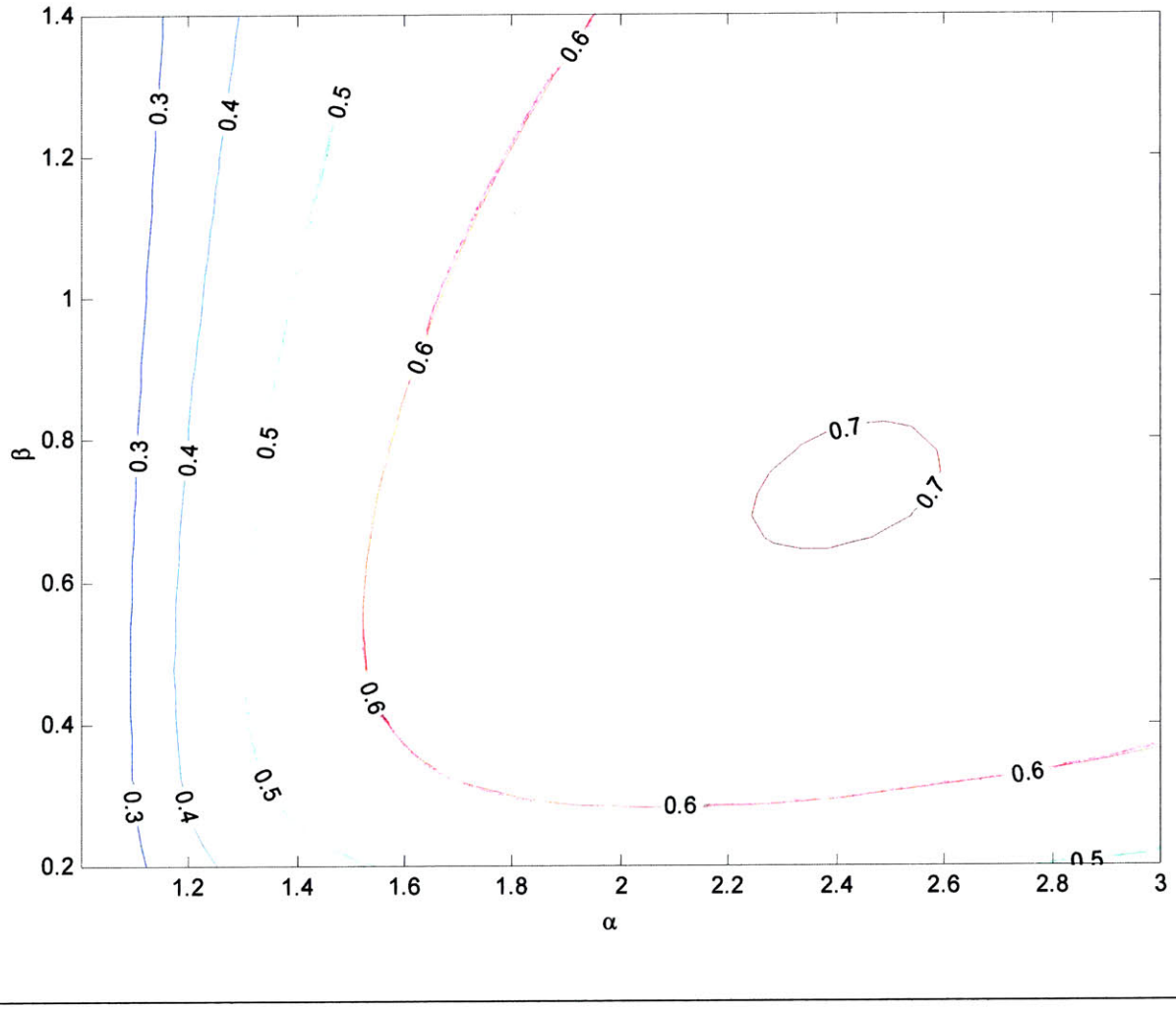


**Figure 3-13 Specific force vs. $\alpha$ and $\beta$**

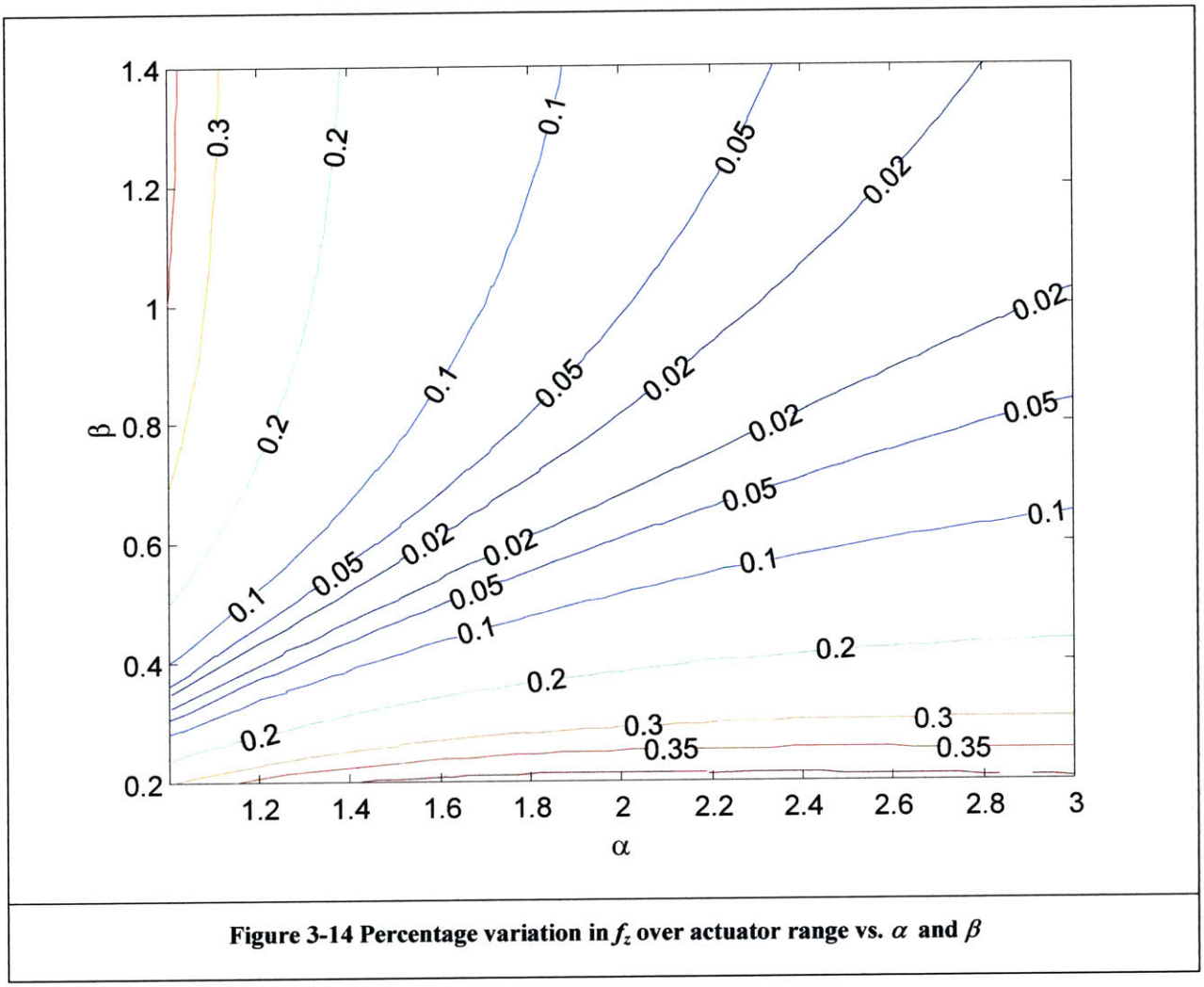


**Figure 3-14 Percentage variation in $f_z$ over actuator range vs. $\alpha$ and $\beta$**

Selection of parameters $\alpha$ =2 and $\beta$ = 0.8 locates the operating point on the "plateau" of Figure 3-13 where $f_z$ = 0.681 N/W and the "valley" of Figure 3-14 where the variation is 0.02%.

The preceding analysis is purely 1 dimensional and takes no account of the radial magnetic field around the coil pair or the off axis axial magnetic fields.

For fine tuning of the actuator a more detailed analysis follows using the numerically evaluated Eq. ( 3-34) to investigate variation in force with radial and axial displacement of the magnet within the coil.

The plot in Figure 3-15 shows the percentage deviation of the axial force for a 0.6mm radial displacement for different values of $g$.

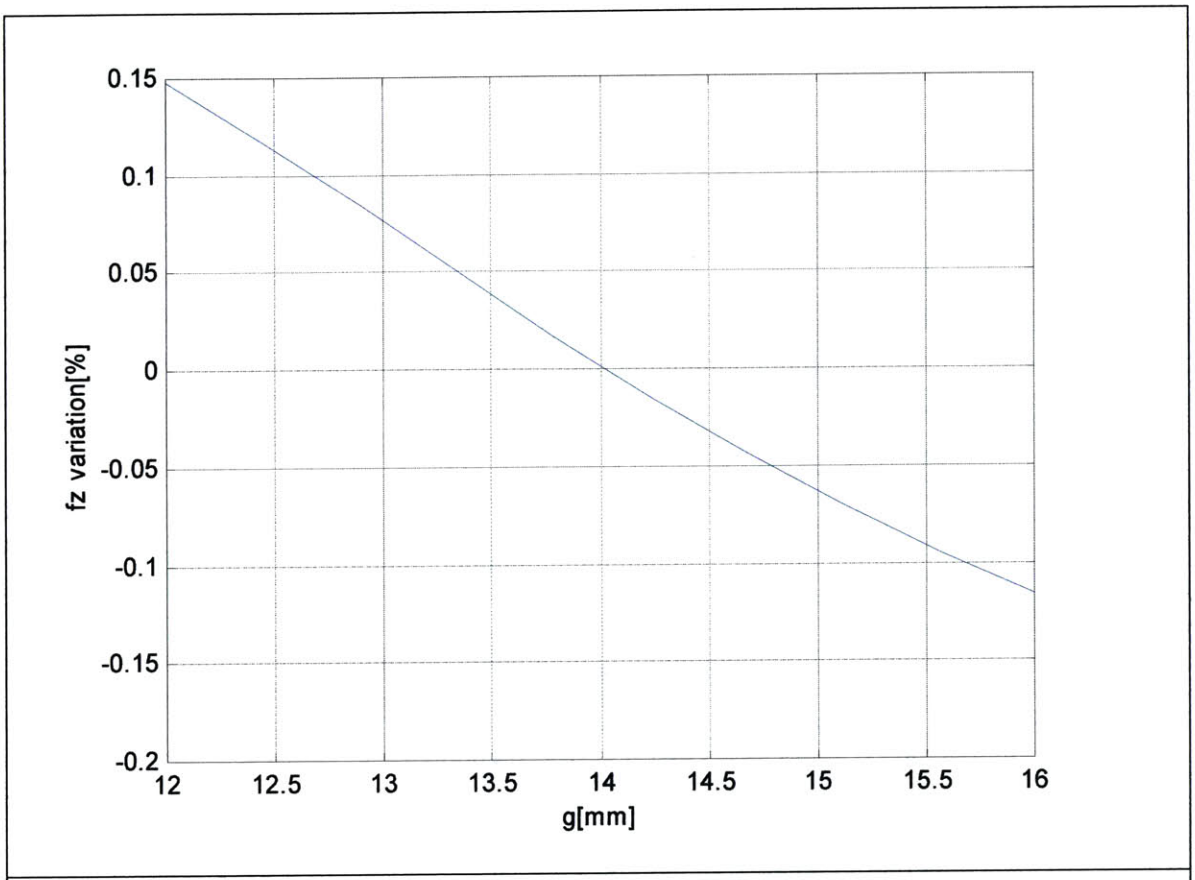


**Figure 3-15 Variation in $f_z$ over a ±0.6mm radial operating range vs. coil separation ($g$)**

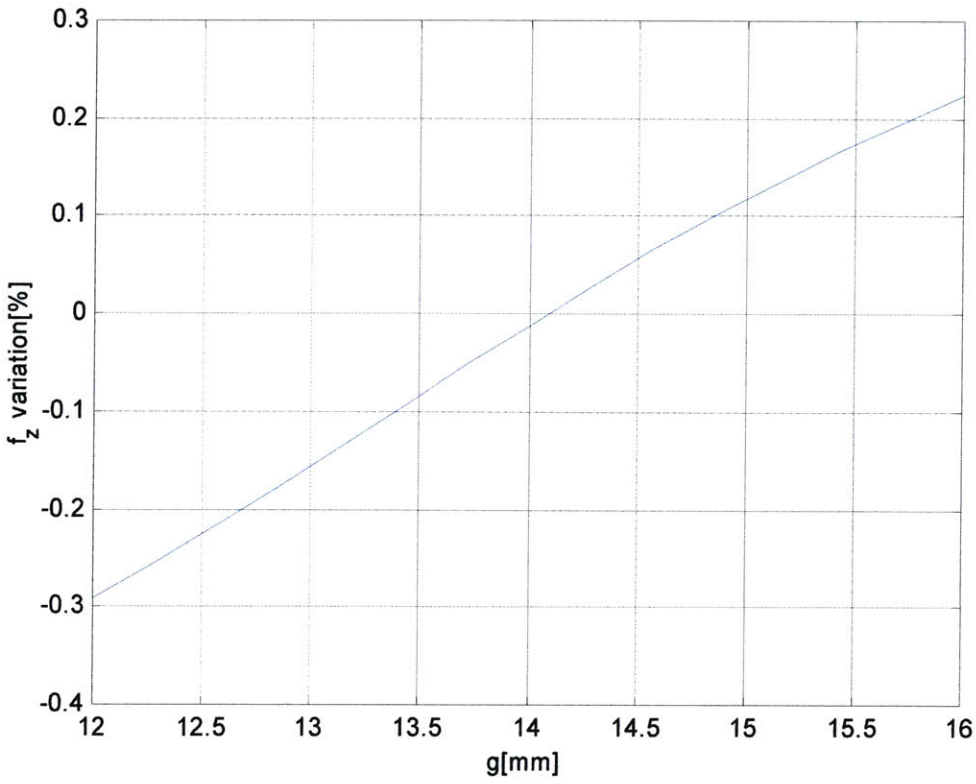


**Figure 3-16 Variation in $f_z$ over a ±0.6mm axial operating range vs. coil separation ($g$)**

The plot in Figure 3-16 shows the percentage deviation of the axial force for a 0.6mm axial displacement. Conveniently the point of zero variation lies at g = 14.1 mm for both radial and axial displacement of the magnet within the axially symmetric dual-coil field (instead of 16mm as predicted by the less accurate one dimensional analytic model). For the new value of g=14.1 mm the numerically integrated axial force from Eq.( 3-34) is 0.77 N/W compared to the 0.76 N/W of the analytic solution in Eq. (3-11).

The sensitivity of the axial force $f_z$ to position of the magnet is given by the contour plot in Figure 3-17. It is useful not only for determining the force variation over the magnet stroke, but also the sensitivity to assembly errors where the magnet is not placed symmetrically in the coil zone.

The chart shows that provided the operating point stays within a sphere of radius 1.6mm, the variation in the force with operating point deviation is less than 0.1%.

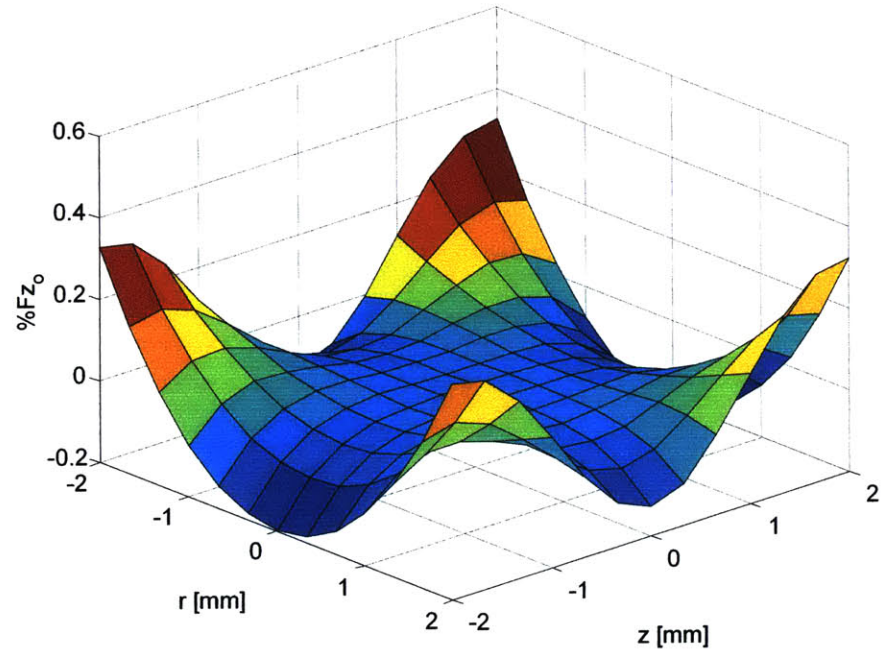


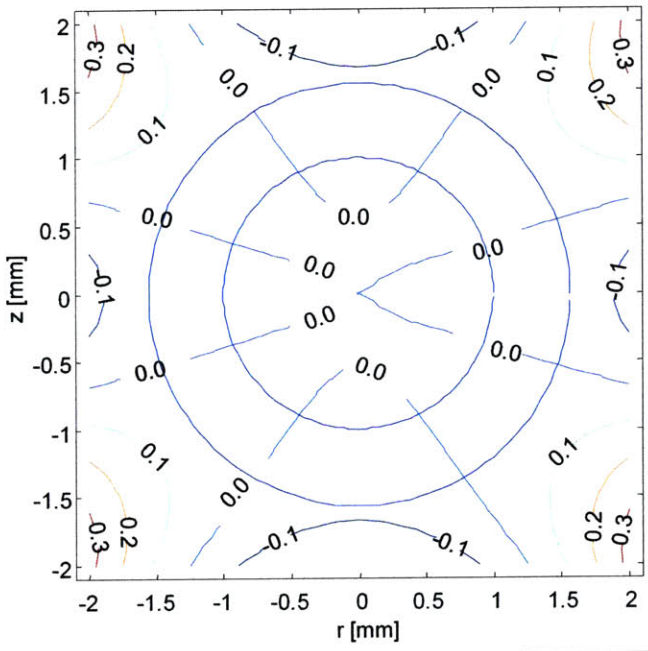


**Figure 3-17 Contour plot of percentage variation in $f_z$ vs. r and z – note circles of radius 1mm and 1.6mm which define the operating region.**

## Coil Arrangement

Having designed the coils, it now remains to arrange them in a manner which minimizes cross-talk so the coils for in-plane actuation do not cause out-of-plane motion and vice versa.

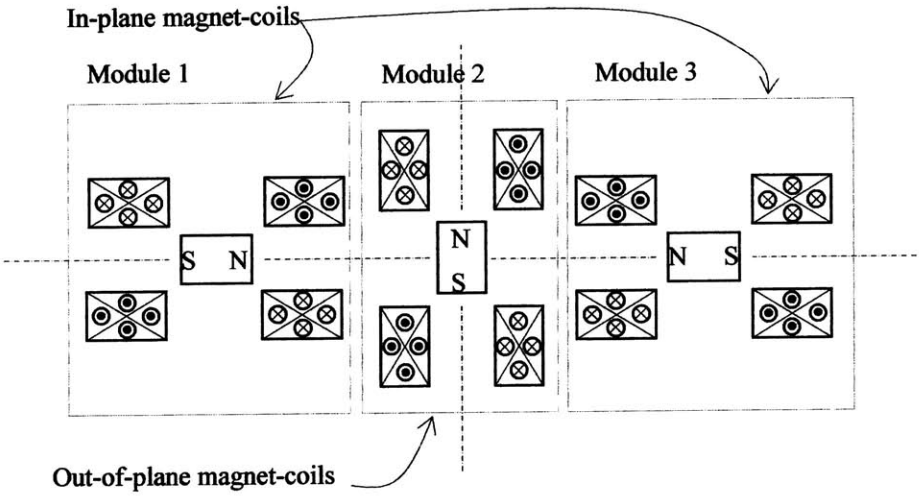


**Figure 3-18 Coil configuration in dual axis actuator**

The arrangement has two desirable characteristics:

1. Parasitic force cancellation. The effects of magnetic fields from modules 1 and 3 cancel in the region of module 2's magnet, minimizing cross talk. Similarly the symmetric arrangement of the magnets in modules 1 and 3 mitigates cross-talk from module 2.
2. A low profile. The dual axis actuator is approximately three times as wide as it is high, exploiting the planar nature of Hexflex.

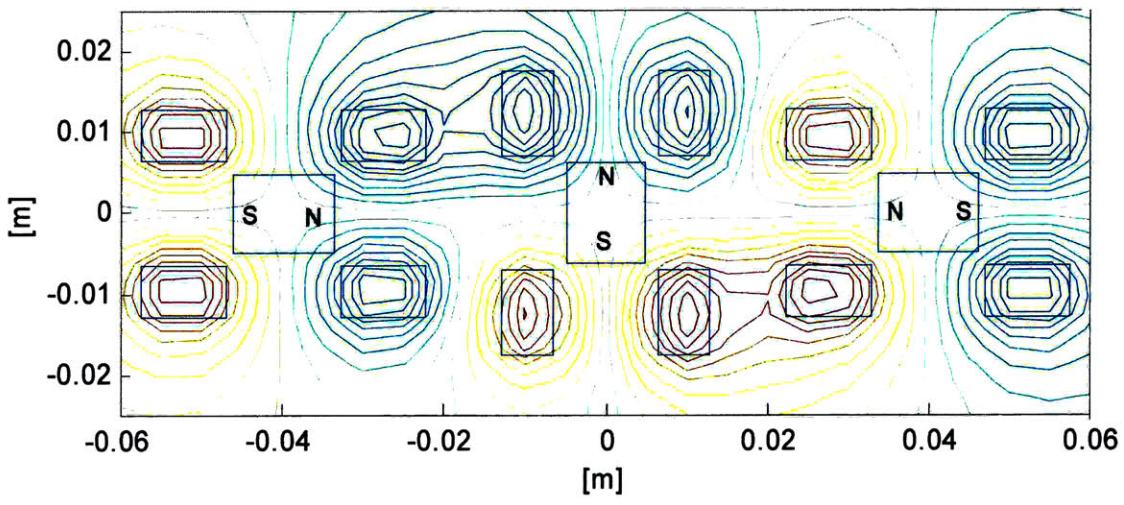


**Figure 3-19 Magnetic flux lines for 1 amp coil current**

The following tables summarize the force and moment contributions of each coil pair on each magnet. Shaded cells contain parasitic forces. Ideally they should sum to zero. Values represent a worst case situation where the actuator is simultaneously displaced 0.6mm in-plane and 0.6mm out-of-plane and current is 1 A for each module.

**Table 3-4 Out-of-plane force contributions**

| | **Coil Pair 1** | **Coil Pair 2** | **Coil Pair 3** |
|---|---|---|---|
| **Magnet 1** | **-0.0003 N** | **-0.0015 N** | **0.0000 N** |
| **Magnet 2** | **0.0421 N** | 2.3914 N | **-0.0478 N** |
| **Magnet 3** | **0.0000 N** | **-0.0013 N** | **-0.0003 N** |
| | | | |
| | **Sum parasitic** | | -0.0090 N |
| | **Parasitic/Desired Force** | | 0.3775% |

| Table 3-5 In-plane force contributions | | | |
|---|---|---|---|
| | **Coil Pair 1** | **Coil Pair 2** | **Coil Pair 3** |
| **Magnet 1** | 2.3914 N | -0.0684 N | -0.0028 N |
| **Magnet 2** | -0.0027 N | -0.0003 N | 0.0031 N |
| **Magnet 3** | -0.0026 N | 0.0620 N | 2.3914 N |
| | | | |
| | **Sum parasitic** | | -0.0063 N |
| | **Parasitic/Desired Force** | | 0.1319% |

| Table 3-6 Clockwise moment contributions about the tab longitudinal axis | | | |
|---|---|---|---|
| | **Coil Pair 1** | **Coil Pair 2** | **Coil Pair 3** |
| **Magnet 1** | -0.0126 Nmm | 0.0155 Nmm | 0.0018 Nmm |
| **Magnet 2** | 0.7747 Nmm | 0.0000 Nmm | -0.8554 Nmm |
| **Magnet 3** | 0.0017 Nmm | 0.0138 Nmm | 0.0126 Nmm |
| | | | |
| | **Sum** | | -0.0478 Nmm |

**Thermal Analysis**

*COSMOS/Works* was used to assess the effect of heat dissipation. The maximum heat generated from each coil is 1.64W. The plots in the figure below show temperature distributions for various materials and geometries. Ambient temperature was set at 25°C. The convective heat transfer coefficient was defined as 5 $W/m^2/K$ which yields very conservative results. The material combination of Figure 3-22 was selected since it resulted in no detectable temperature change in the aluminum base and flexure.

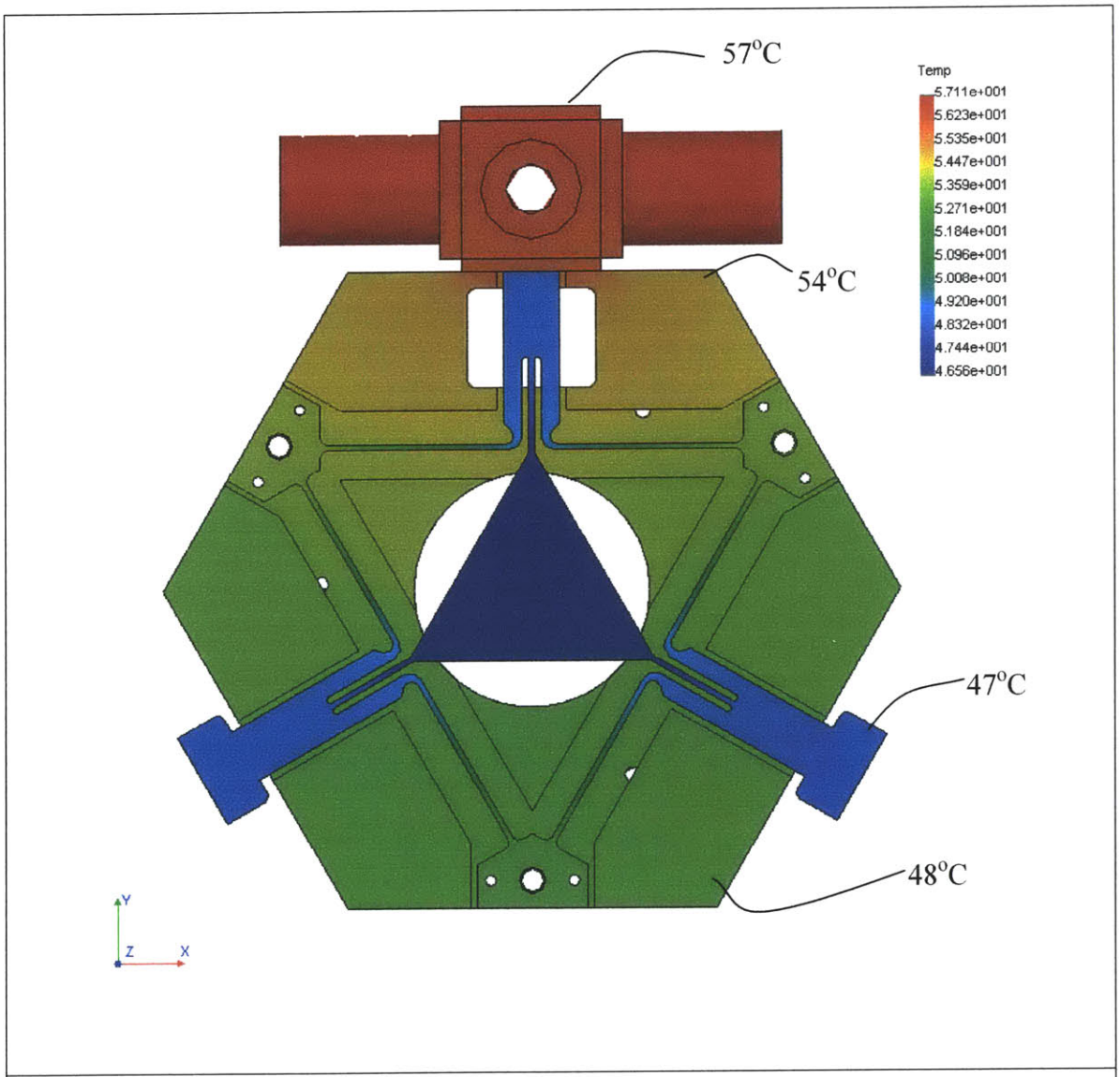


**Figure 3-20 Temperature distribution with all aluminum construction**

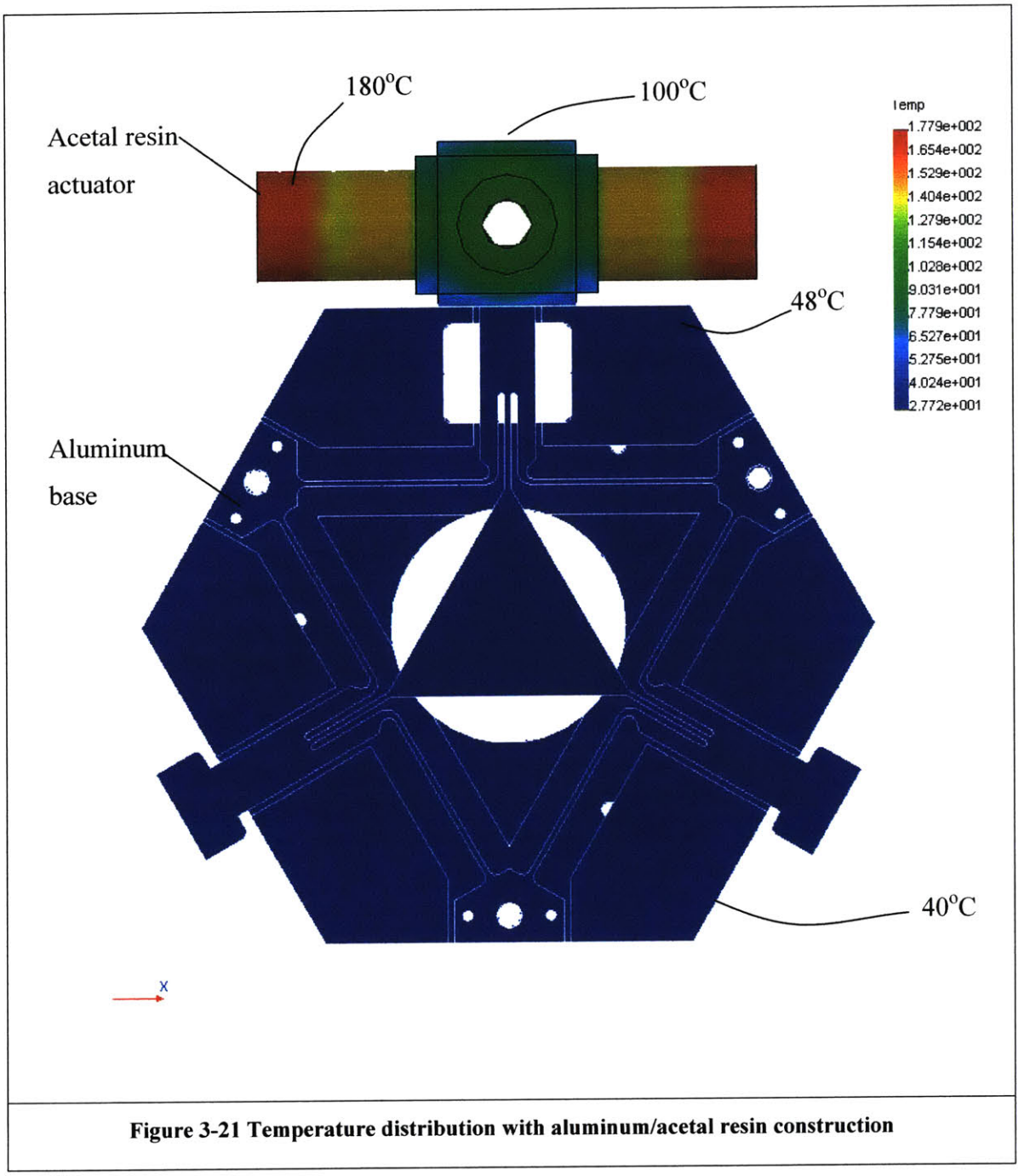


**Figure 3-21 Temperature distribution with aluminum/acetal resin construction**

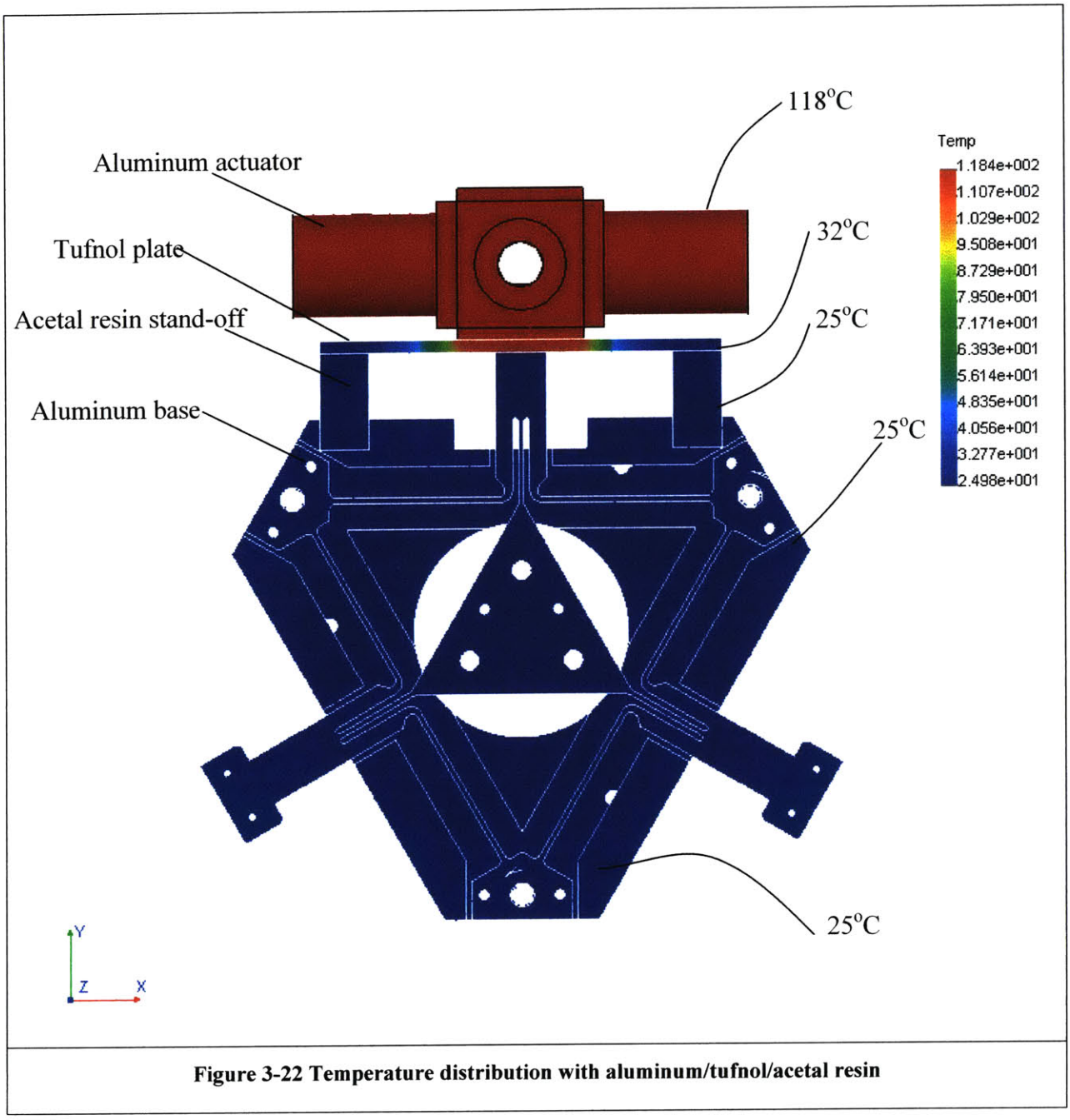


**Figure 3-22 Temperature distribution with aluminum/tufnol/acetal resin**

## 3.4 Error Estimate

| Table 3-7 Error estimate | | |
|---|---|---|
| | **In-plane** | **Magnitude** |
| 1. | Non linearity due to variation in actuator force over full stroke with axial and radial assembly errors of 0.25mm | 0.009 μm |
| 2. | Cross-talk from out-of-plane actuator | 0.099 μm |
| 3. | Quantization error from 16 bit D/A converter | 0.001 μm |
| | | |
| | **Sum errors** | 0.109 μm |
| | **RSS errors** | 0.099 μm |
| | **Ave** | 0.104 μm |
| | | |
| | **Out-of-plane** | |
| 1. | Non linearity due to variation in actuator force over full stroke with axial and radial assembly errors of 0.25mm | 0.004 μm |
| 2. | Cross-talk from in-plane actuator | 0.045μm |
| 3. | Quantization error from 16 bit D/A converter | 0.0003 μm |
| | | |
| | **Sum errors** | 0.050 μm |
| | **RSS errors** | 0.045 μm |
| | **Ave** | 0.047 μm |

## 3.5 General Arrangement

Views of the manipulator are provided in Figure 3-23, Figure 3-24 and Figure 3-25. The manipulator has four major sub-systems: the base (monolithic, aluminum), the Hexflex mechanism (monolithic, aluminum), thermal stand-offs (acetal resin) and dual axis electromagnetic actuators (aluminum mandrels and copper windings). These low-cost, high thermal expansion materials may be used due to the inherent thermal stability of the mechanism and the system's insensitivity to actuator-mechanism misalignment. Note that making the base and mechanism from the same, high thermal diffusivity material prevents thermally driven out-of-plane buckling.

The tabs of the Hexflex mechanism are fitted with two sets of magnets, one for each axis. The actuators are attached to the aluminum base with acetal resin standoffs and Tufnol attachment plates. The non-metallic components prevent conductive heat transfer from the actuators to the base. Each actuator consists of two sets of coils; a horizontal set for in-plane actuation and a vertical set for out-of-plane actuation. Capacitance probes, attached to the base with flexure clamps, measure the displacement between the base and the probe target. The position sensor shown in Figure 3-24 was not used in any of the tests described in this work.

*A:*

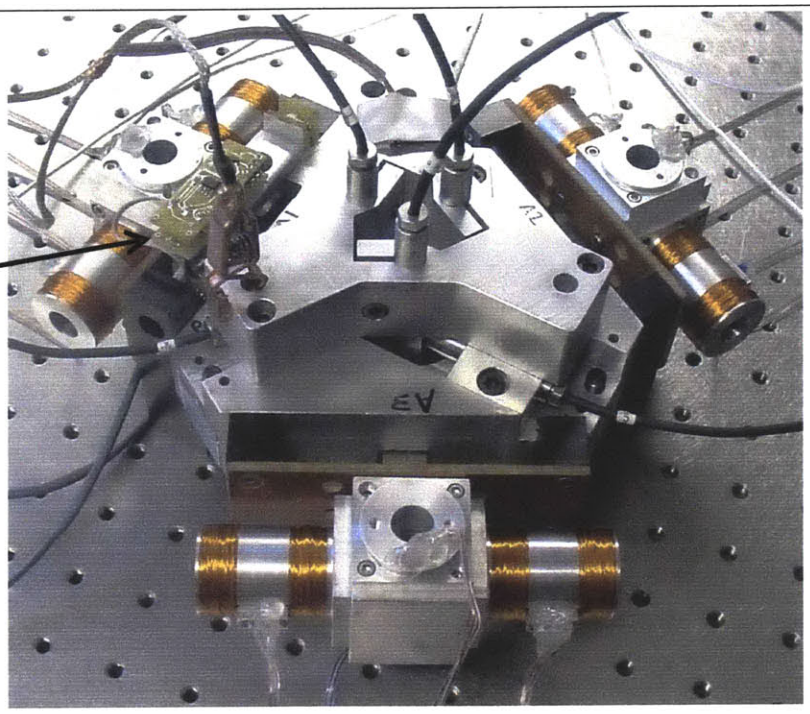


*B:*

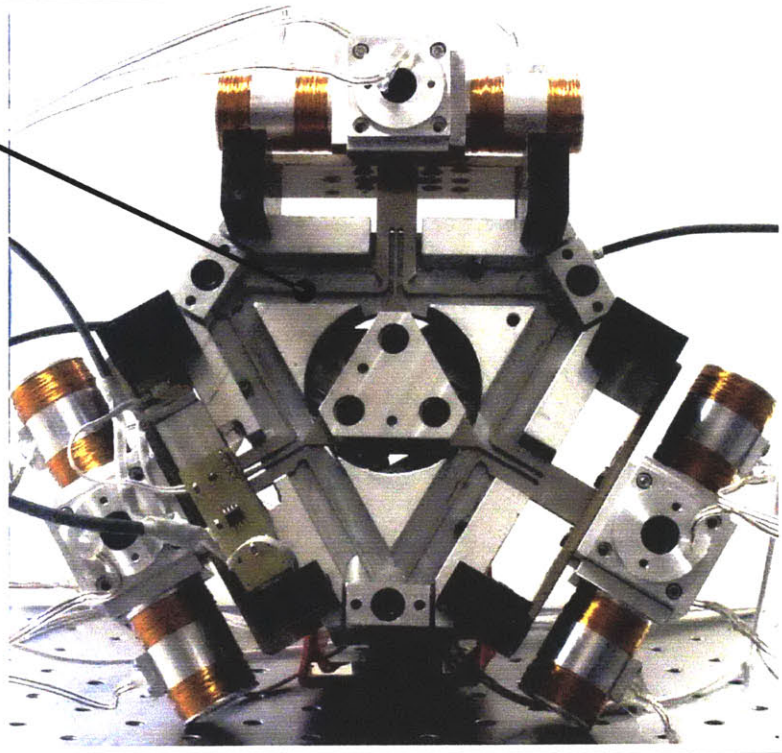


**Figure 3-23 Positioning stage**

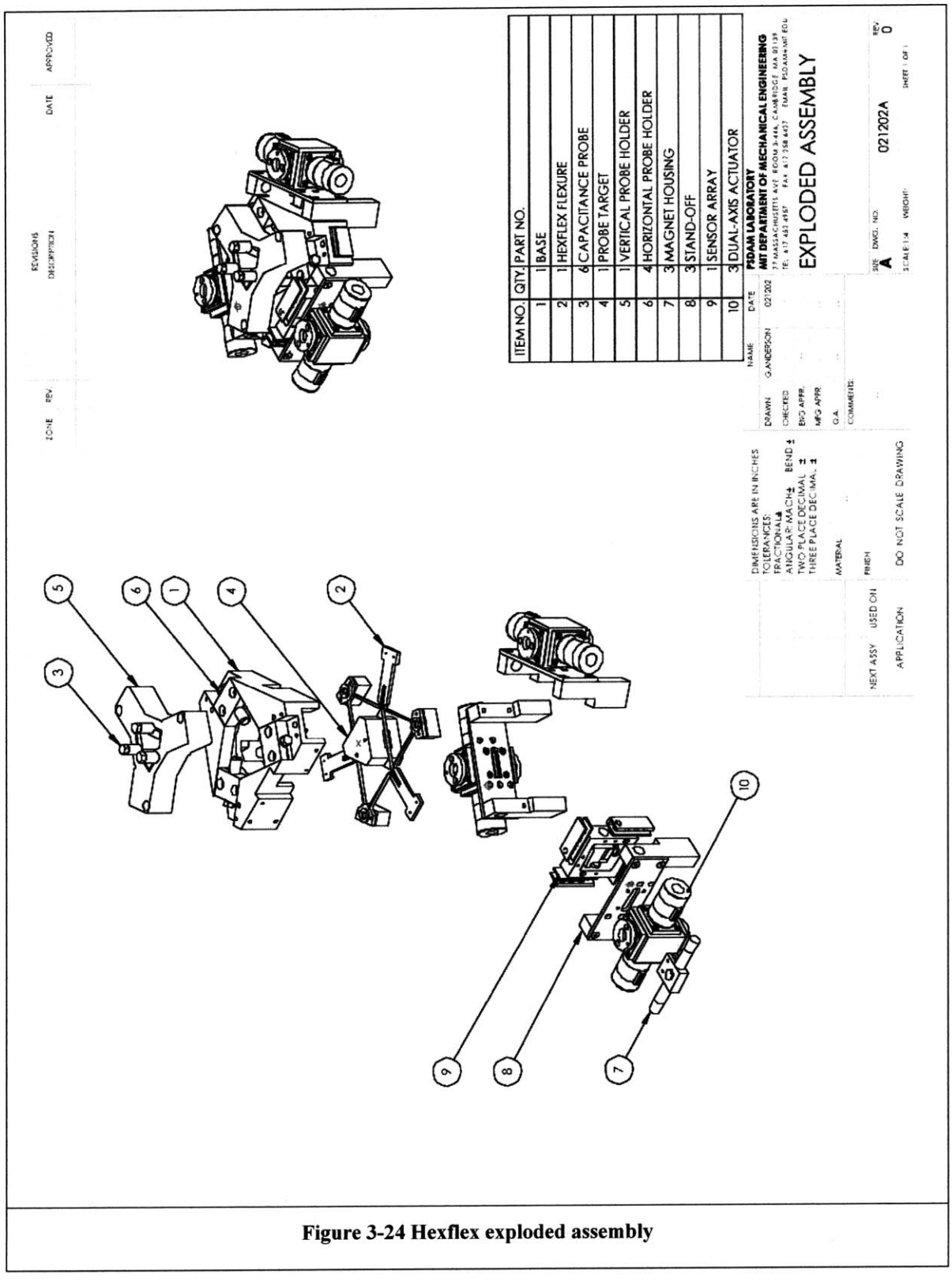


**Figure 3-24 Hexflex exploded assembly**

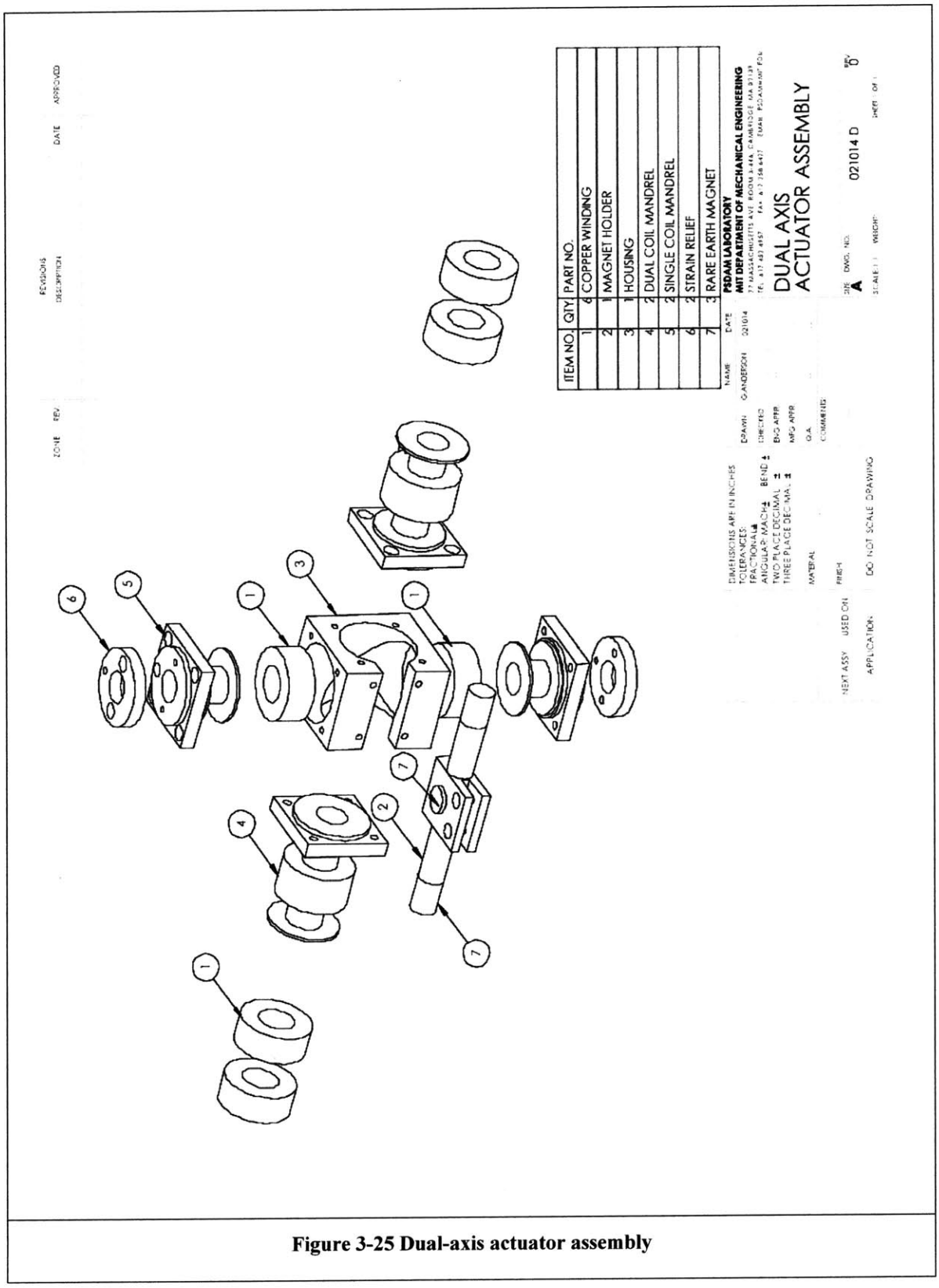


**Figure 3-25 Dual-axis actuator assembly**

## 3.6 Cost Summary

| Table 3-8 Manufacturing costs | | | |
|---|---|---|---|
| **Item** | **Quantity** | **Unit Cost** | **Total** |
| | | | |
| *Hardware* | | | |
| Magnet | 9 | $8 | $72 |
| Base | 1 | $50 | $50 |
| Flexure | 1 | $8 | $8 |
| Housing | 3 | $3 | $9 |
| Single-coil mandrel | 6 | $2 | $12 |
| Dual-coil mandrel | 6 | $4 | $24 |
| Copper winding | 1 | $14 | $14 |
| Delrin stand off | 6 | $0.5 | $3 |
| Machining and assembly | 37 hours | $50/hour | $1,850 |
| **Total** | | | $2,042 |

# Chapter 4 Testing

## 4.1 Instrumentation

Six Lion Precision model C1-C capacitance probes recorded the position of the triangular target fixed to the Hexflex centroid. The peak to peak resolution of the probes is on the order of 20nm for the high sensitivity setting or 100nm for low sensitivity. The high sensitivity range is 75 to 125 μm with a probe standoff of 100 μm, output sensitivity of 0.4V/μm and a maximum linearity error of 0.50% full scale. On the low sensitivity setting, range is 125 to 375 μm, probe standoff 250 μm, sensitivity 0.08V/μm and maximum linearity error is 0.30%.

The six ±10V capacitance probe signals were sampled with a DSPACE DS 1104 controller board using 2 channels on a multiplexed 16 bit analogue-to-digital converter (A/D) and 4 channels on dedicated 12 bit A/Ds. The 12 bit A/D limits the effective resolution to ±6nm for the high sensitivity capacitance probe range and ±30 nm for the low sensitivity setting.

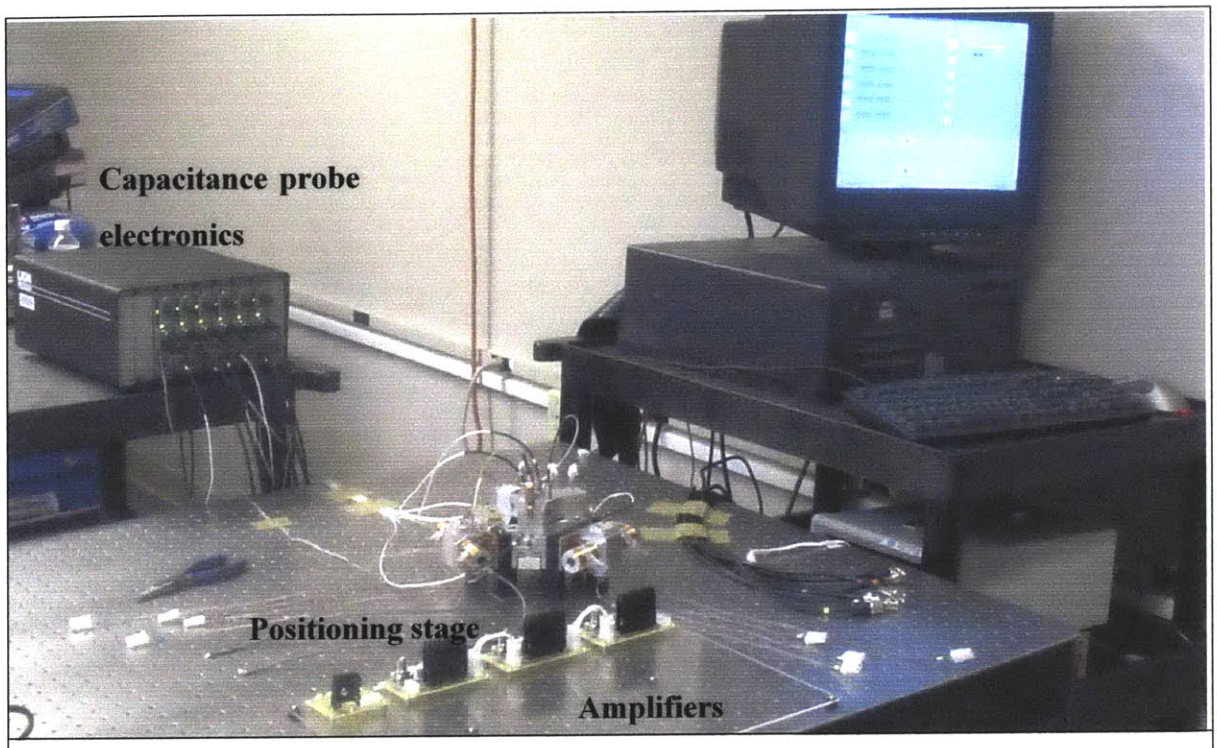


**Figure 4-1 Apparatus**

The magnet coils were driven by six voltage controlled current sources based on the Apex PA 26 power amplifier with ±500mA current output for a ±10V control signal from the DSPACE controller's 16 bit digital to analogue converters.

## 4.2 CoMeT Validation

Figure 4-2 and Figure 4-3 record centroid response to the mounting of dead weights to an actuator tab. The errors between the experimental result (20.91μm/N) for the in-plane x-displacement transmission ratio and estimates by *CoMeT* and a standard FEA program(*COSMOS/Works*$^{TM}$) are 3.2% and 8.2% respectively. For the in-plane theta z-rotation transmission ratio (-385.7μrad/N), the corresponding errors are 4.5% and 3.3%. The respective out-of-plane errors for *CoMeT* and *COSMOS/Works* are 12.1% and 1.2%

for the z-displacement transmission ratio(-22.77μm/N) and 13.9% and 7.3% for the theta x-rotation transmission ratio (-2161μrad/N).

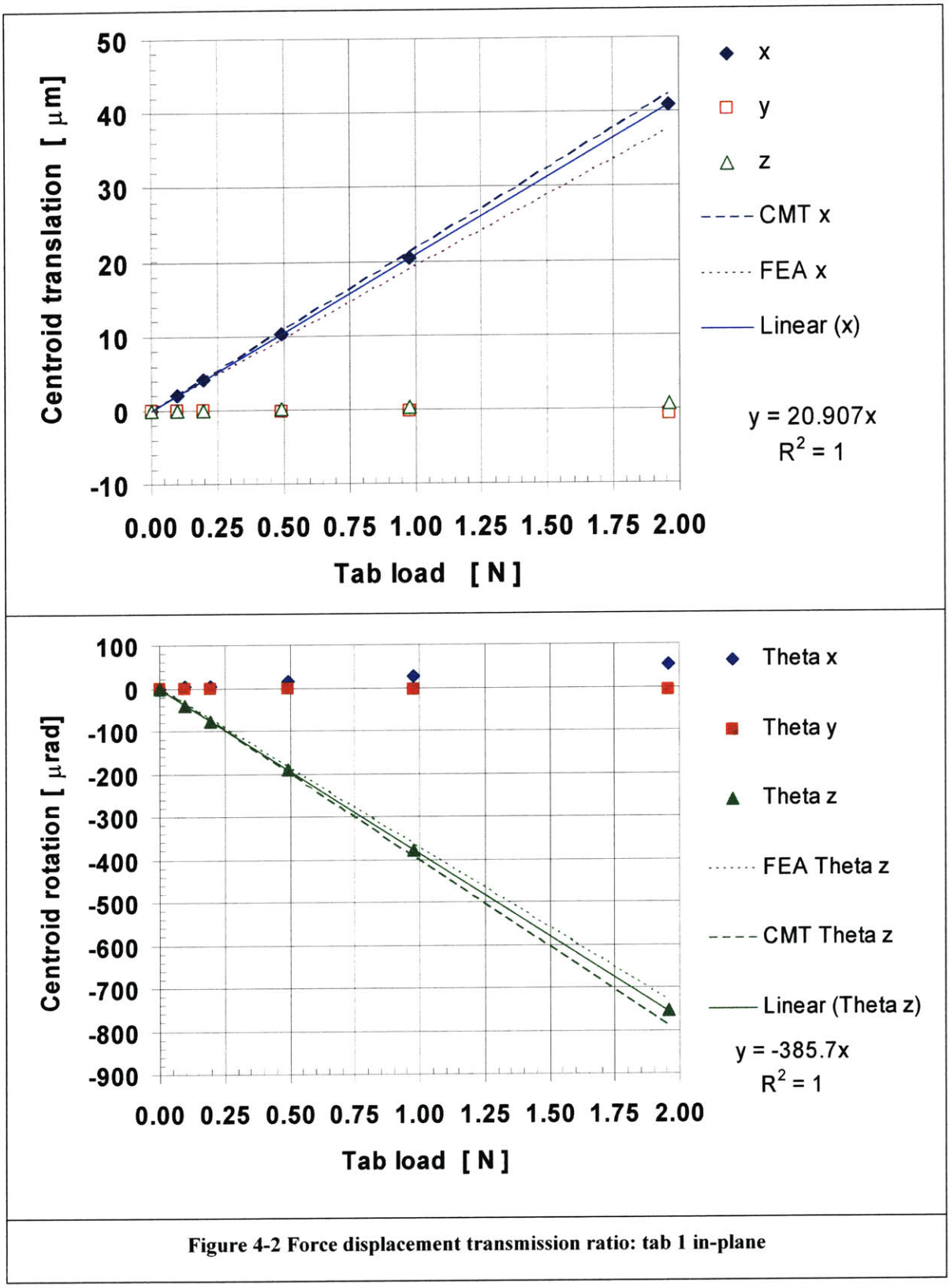


**Figure 4-2 Force displacement transmission ratio: tab 1 in-plane**

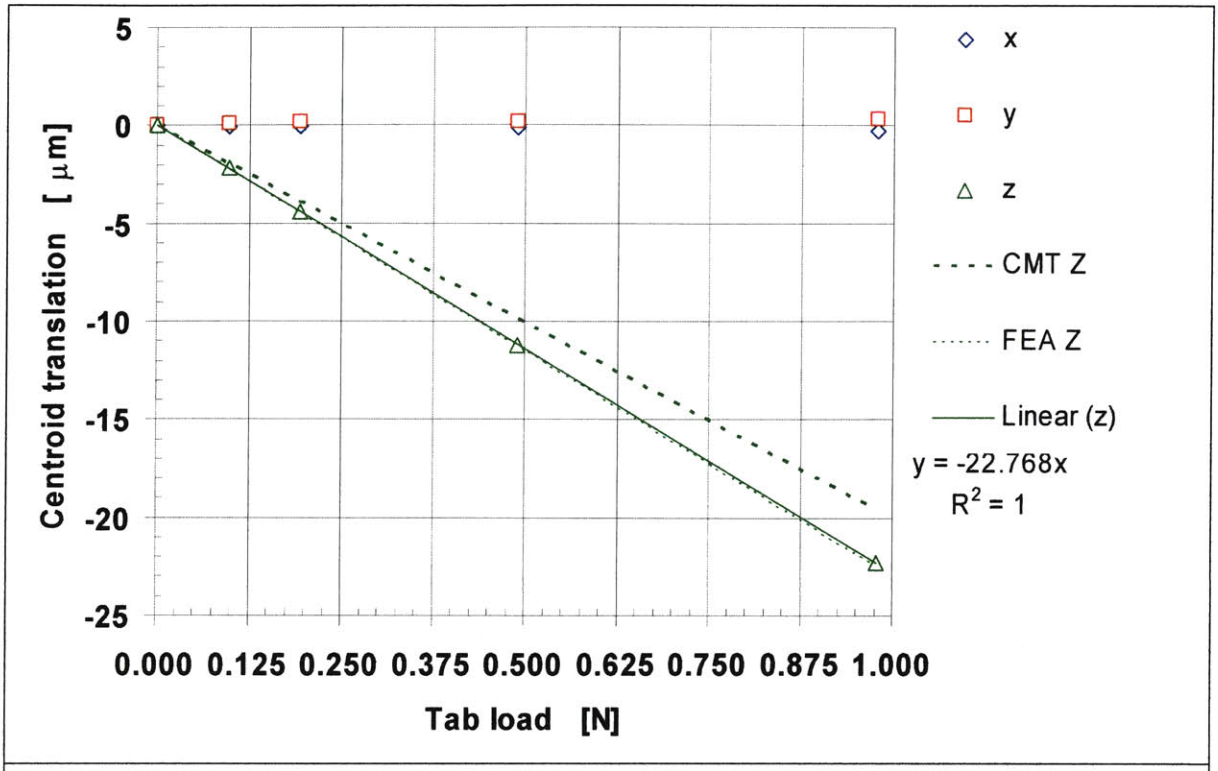


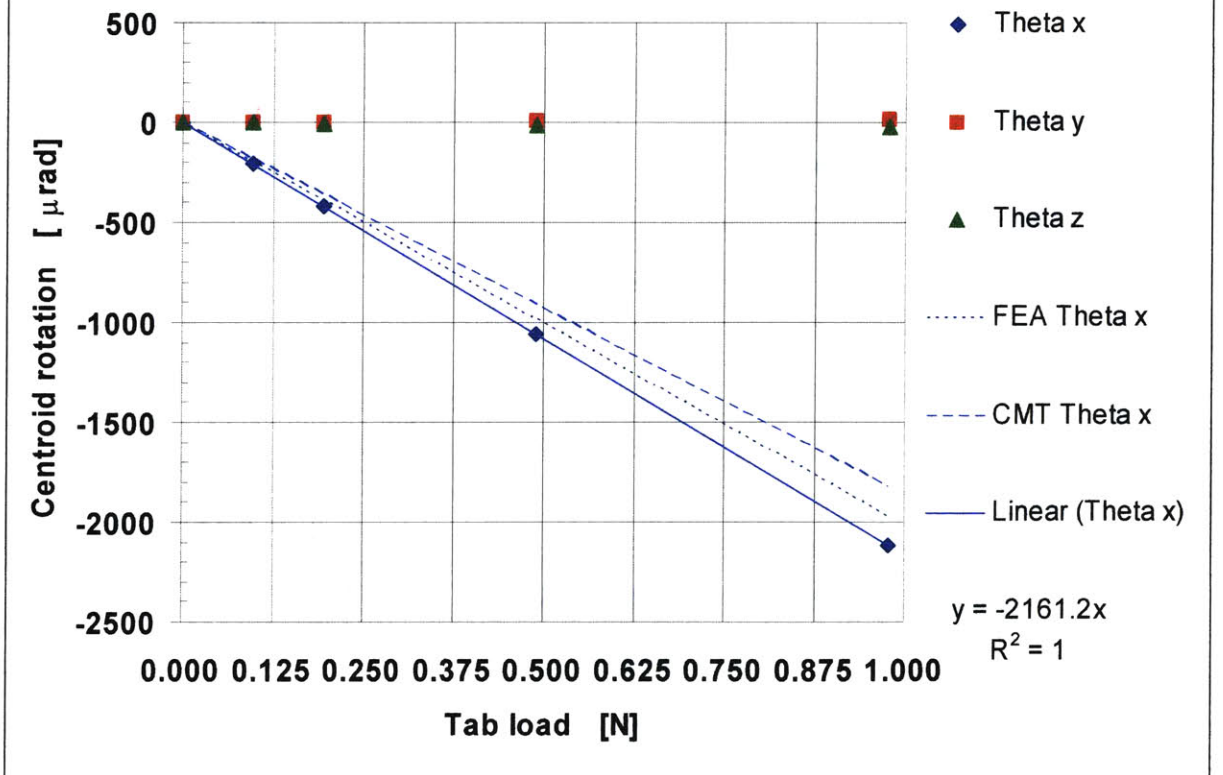


**Figure 4-3 Force displacement transmission ratio: tab 1 out-of-plane**

## 4.3 Actuator analysis validation

The experimentally determined transmission ratios from Figure 4-2 and Figure 4-3 were used to validate the actuator force/current constant given by Eq. ( 3-34) for tab 1. The theoretical combined force current constant for the (500 turn per coil) twin in-plane actuators is 4.79 N/A, compared to 2.33N/A for the (488 turn per coil) single out-of-plane actuator. The product of the transmission ratio and the force/current constant yields the theoretical displacement/current behavior plotted against experimental results in Figure 4-4 and Figure 4-5. The error in actuator performance predicted by Eq. ( 3-34) and reality is 3.4% for the twin in-plane actuators and 6.9% for the single out-of-plane actuator.

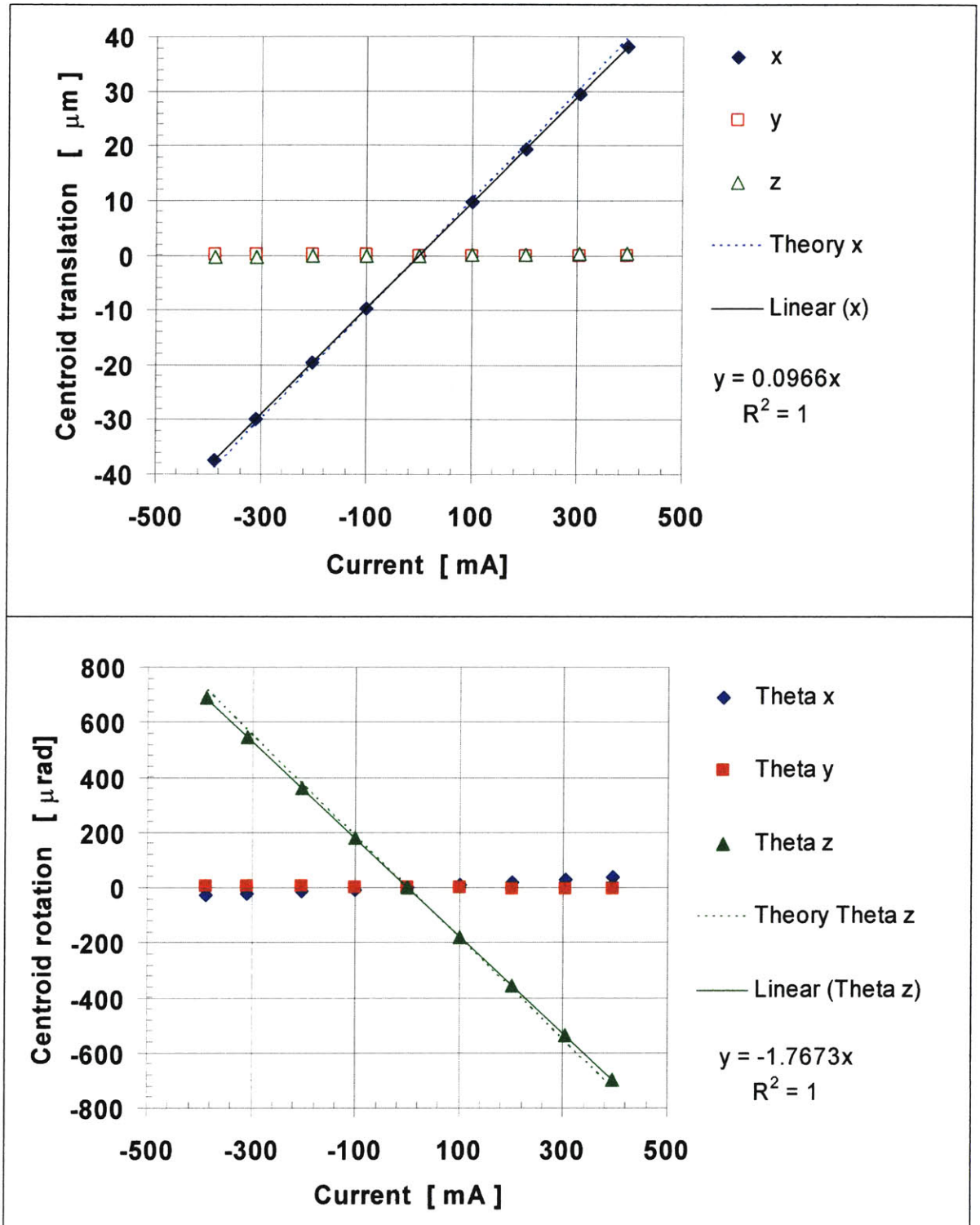


**Figure 4-4 Centroid displacement vs. current: tab 1 in-plane**

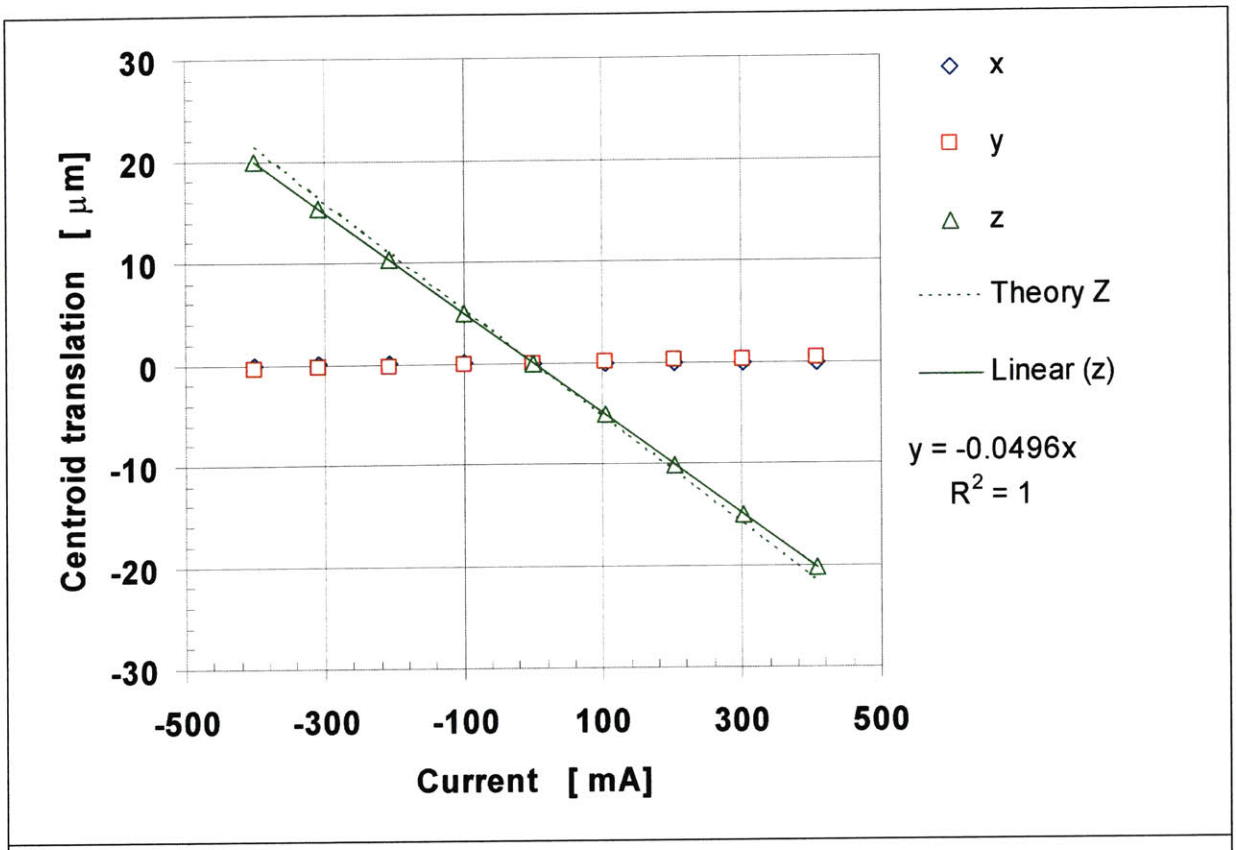


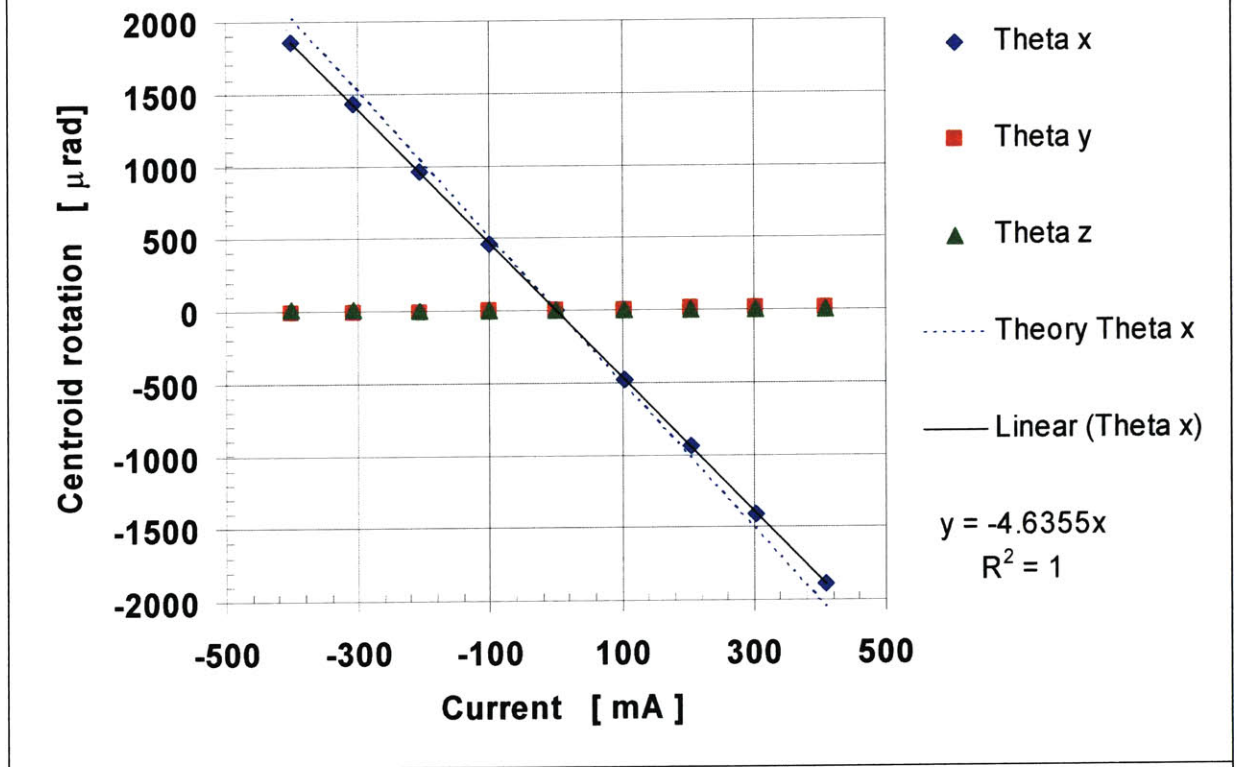


**Figure 4-5 Centroid displacement vs. current: tab 1 out-of-plane**

## 4.4 Calibration

Naturally, the prototypes deformation response varies from design by a small amount due to manufacturing errors, idealizations used in analysis, variation in material properties, etc... The difference between the theoretical and empirical $\mathbf{S_F}$ matrices is shown below.

$$\mathbf{S}_{\text{F\_COMET}} = \begin{bmatrix} 25.71 & -12.73 & -12.73 & 0 & 0 & 0 \\ 0 & -22.10 & 22.10 & 0 & 0 & 0 \\ 0 & 0 & 0 & 20.91 & 20.91 & 20.91 \\ 0 & 0 & 0 & 2022 & -1007 & -1007 \\ 0 & 0 & 0 & 0 & 1740 & -1740 \\ -477.2 & -477.2 & -477.2 & 0 & 0 & 0 \end{bmatrix}$$

$$\mathbf{S}_{\text{F\_EMPIRICAL}} = \begin{bmatrix} 20.25 & -10.48 & -8.725 & 0.4199 & -0.8181 & 0.3215 \\ -0.06913 & -18.31 & 15.45 & -0.5773 & -0.9455 & 0.1892 \\ 0.01579 & -0.1232 & 0.2869 & 20.26 & 22.09 & 20.07 \\ -19.88 & 0.5862 & 4.933 & 1905 & -999.1 & -941.4 \\ -12.48 & 8.381 & -6.339 & 32.57 & 1721 & -1655 \\ -392.6 & -393.3 & -362.3 & 37.17 & 6.229 & 9.178 \end{bmatrix}$$

The values of elements r1c1, r6c1, r3c4 and r4c4 of the $\mathbf{S_{F\_EMPIRICAL}}$ matrix do not correspond to the gradients in Figure 4-4 and Figure 4-5 because of inaccuracies in predicting the actuator force current relationship.

The actuator inputs ($\mathbf{F_A}$) required for a desired stage displacement ($\mathbf{X_C}$) were calculated using $\mathbf{S_{F\_EMPIRICAL}}$ in Eq.(1-3). The stage motion produced by this control technique is discussed in section 4.5.

## 4.5 Displacement results

A first experiment was conducted on the low sensitivity capacitance probe setting within a micro-manipulation work volume (100 x 100 x 100 $\mu m^3$). Parasitic translation error motions were less than 215 nm and angular errors were less then 4.13 μrad. The worst case linearity error for x-translation in Figure A-1 was 0.05% full-scale, y-translation in Figure A-2 was 0.20% and z-translation in Figure A-3 was 0.04%. The maximum linearity error for $\theta_x$ rotation in Figure A-4 was 0.08%, $\theta_y$ rotation in Figure A-5 was 0.12% and $\theta_z$ rotation in Figure A-6 was 0.10%. Micro-manipulation performance can be improved to match the nano-manipulation performance in Figure A-7 to Figure A-9 with closed-loop control.

A second experiment was run on the high sensitivity capacitance probe setting within a nano-manipulation work volume (0.100 x 0.100 x 0.100 $\mu m^3$). Measured displacements versus open-loop displacement commands and off-axis errors are shown in Figure A-7 to Figure A-9. The performance of the probes limits the measurement resolution during this test to 5 nm, which probably accounts for the relatively small (~ 5 nm) deviations from linear behavior seen in the data. Parasitic errors are generally below the resolution of the measurement system (0.005% of the device's full work volume).

**Table 4-1 Error summary (-50μm to 50μm translation and -2000 μrad to 2000 μrad rotation)**

| **Primary motion** | **x** | **y** | **z** | **theta x** | **theta y** | **theta z** |
|---|---|---|---|---|---|---|
| **Range** | -50: 50μm | -50: 50μm | -50: 50μm | -2500 : 2500μrad | -2500: 2500μrad | -2500: 2500μrad |
| **Error motion [μm/μrad]** | | | | | | |
| **x** | **0.045** | 0.056 | 0.075 | 0.033 | 0.052 | 0.126 |
| **y** | 0.055 | **0.198** | 0.035 | 0.054 | 0.025 | 0.158 |
| **z** | 0.064 | 0.067 | **0.038** | 0.054 | 0.054 | 0.213 |
| **theta x** | 3.255 | 4.127 | 2.204 | **3.137** | 1.192 | 1.410 |
| **theta y** | 0.577 | 1.331 | 3.640 | 2.22 | **4.676** | 2.907 |
| **theta z** | 1.746 | 1.554 | 2.019 | 2.002 | 3.108 | **3.913** |

| Table 4-2 Error summary (0 – 0.100 μm translation) | | | |
|---|---|---|---|
| **Primary motion** | **x** | **y** | **z** |
| **Range** | 0: 0.100μm | 0:0.100μm | 0: 0.100μm |
| **Error motion [μm/μrad]** | | | |
| **x** | **0.002** | 0.003 | 0.005 |
| **y** | 0.003 | **0.005** | 0.002 |
| **z** | 0.004 | 0.005 | **0.003** |
| **theta x** | 0.233 | 0.064 | 0.226 |
| **theta y** | 0.120 | 0.0186 | 0.129 |
| **theta z** | 0.532 | 0.544 | 0.247 |

The figures in bold are linearity errors, the remainder record parasitic motion.

It is of concern that the maximum non-linearity for y translation is 0.198μm (0.198% F.S). This exceeds the worst case error estimate of Table 3-7 by a factor of 2.

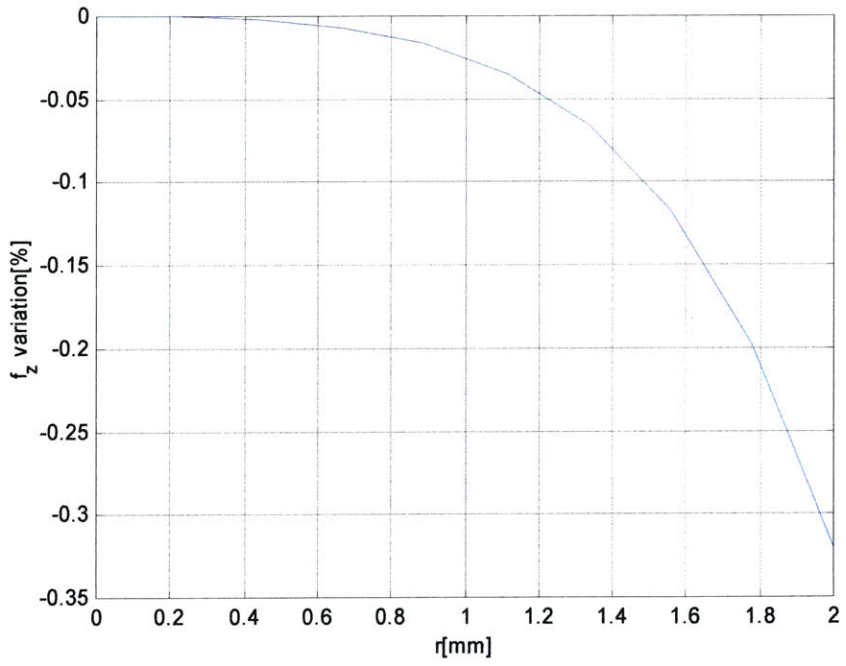


**Figure 4-6 Percentage variation in $f_z$ vs. $r$**

Figure 4-6 suggests that the magnets for in-plane actuation experienced radial displacements of 1.8mm which caused the 0.2% non-linearity. The reason for this phenomenon is that the tabs experience an in-plane rotation in addition to translation. Although the translation does not exceed 0.6mm, the additional rotation causes extra radial displacement which when added to an initial assembly error is sufficient to cause the force variation. Future versions of the Hexflex should have a larger displacement transmission ratio (and hence smaller actuator range) which will reduce sensitivity to assembly misalignment errors and improve the constancy of force over the stroke.

## 4.6 Repeatability

To assess the repeatability of the device, it was stepped over a nominal range of 52 μm from x = y =z =15μm to x =y =z =-15 μm and then back again. The position of the stage was measured each time the device returned to the x =y =z =15μm state.

This process was repeated at 4s intervals 100 times.

The data is summarized by the table below and in Figure B-1.

**Table 4-3 Repeatability results**

| Direction | σ | 3σ |
|---|---|---|
| x | 0.004 μm | 0.013 μm |
| y | 0.002 μm | 0.007 μm |
| z | 0.003 μm | 0.008 μm |

The standard deviation of the cap probe readings themselves taken with respect to a stationary target is 0.002μm to 0.004μm. Therefore the repeatability of the system is at least on the same order as the cap probe measuring devices; however repeatability measurements depend on the circumstances under which they were obtained. In this case measurements represent a best case scenario as the limited testing duration (400s) did not

provide sufficient time for some sources of non-repeatability (like amplifier offset drift, thermal expansion and creep) to become manifest.

## 4.7 Natural Frequency

The response to a manual 'tap' was recorded for a 0.2s interval at a sampling rate of 10kHz. The lowest natural frequency of each axis is shown in Table 4-4.

**Table 4-4 Natural frequency of vibration**

| Direction | Natural frequency |
|---|---|
| **x** | 110 Hz |
| **y** | 110 Hz |
| **z** | 160 Hz |
| **Theta x** | 40 Hz |
| **Theta y** | 40 Hz |
| **Theta z** | 320 Hz |

Frequency spectrum plots are given in Figure C-2.

The relatively low natural frequency tests have identified a key area for future work. Reducing the mass of the magnet housing on the tabs and increasing flexure stiffness is a priority. The magnet mass should be transferred to the base in applications where high natural frequency is more important than stability. Light weight coils can then be mounted on the tabs in the "moving coil" actuator configuration.

## 4.8 Drift

The open-loop start-up drift was measured after a 15 micron displacement in z. The stage was thermally isolated to ensure the only thermal disturbances were due to actuator power dissipation. Plots of drift over a thirty minute start-up period are provided in Figure 4-7. Temperature variation during the drift test is given in Figure 4-8. The maximum thermal drift, 23 nm over 30 minutes (for a 0.1°C temperature change) compares favorably with state-of-the art commercial manipulators which demonstrate 6500 nm drift over 30 minutes [26].

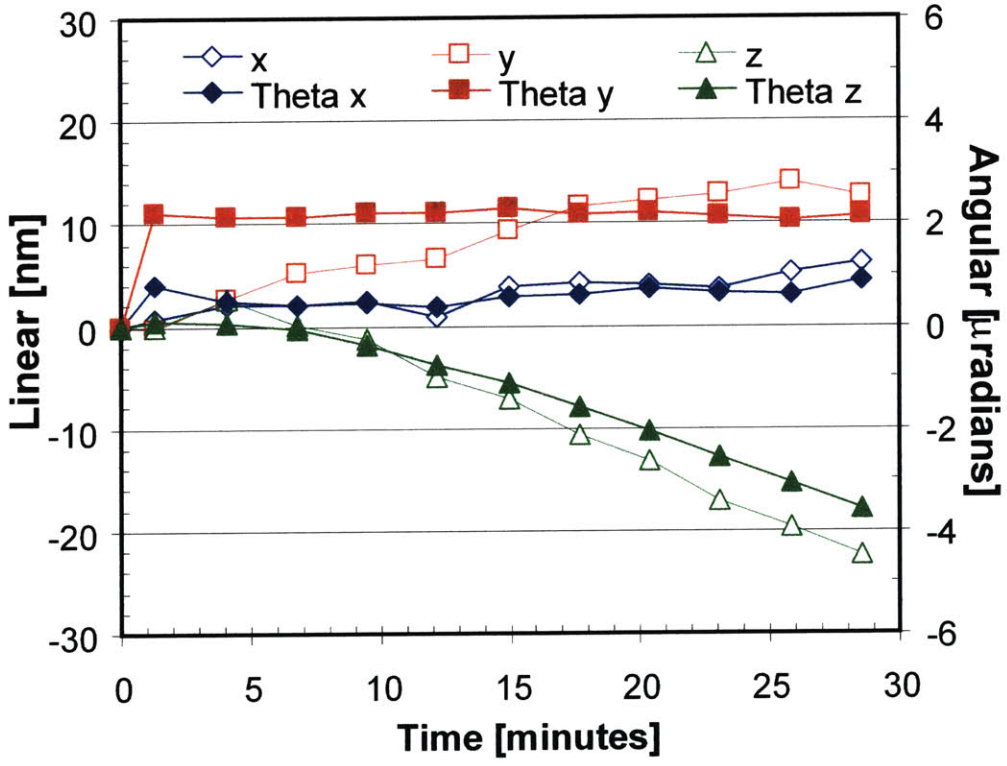


**Figure 4-7 Drift test – position variation**

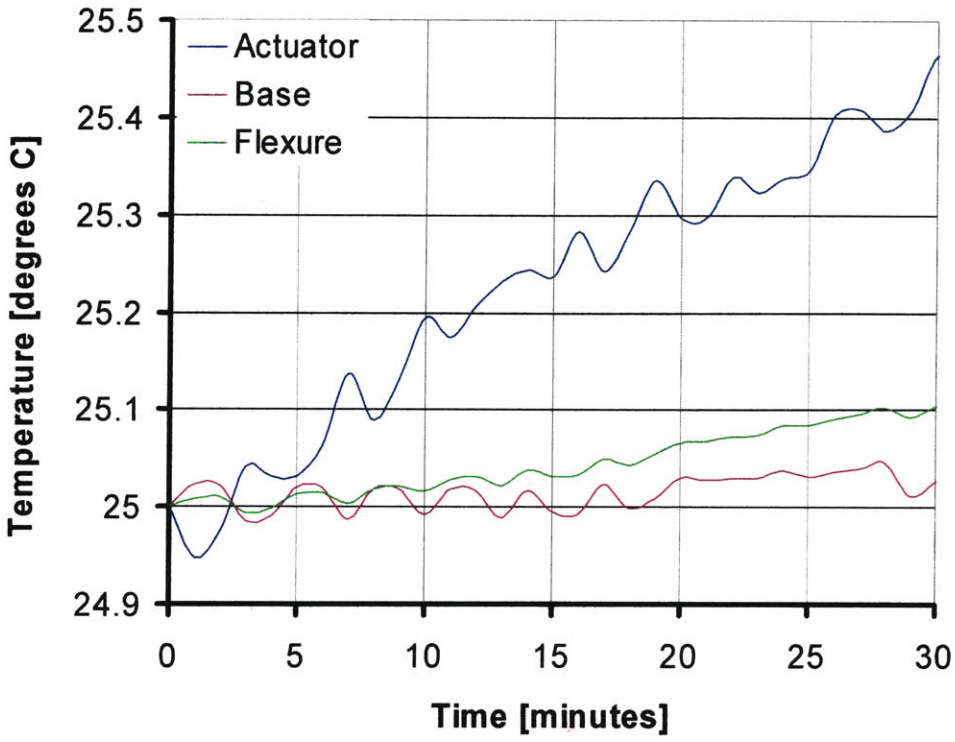


**Figure 4-8 Drift test – temperature variation**

# Chapter 5 Case Study

## 5.1 Introduction

The Hexflex was used to align two single mode optical fibers. The loss detection was performed with an HP 81532 light wave multimeter. The fiber core diameter is 8.5 μm and cladding diameter 125 μm. Wavelength at 1550nm yields a mode field radius of 10.25μm.

Light coupling is limited by the reflection at the glass air boundary in the gap between the fibers. The amplitude reflection coefficient for two different optical media at normal incidence is given by [23]

$$r = \frac{n_t - n_i}{n_t + n_i} \qquad \textbf{(5-1)}$$

For an air glass interface with $n_{glass}$=1.45 and $n_{air}$ =1, r =±0.18. Consequently the power transmission loss through the gap (with two air-glass interfaces) is approximately [23]

$$\begin{aligned} Loss &= 20\log(1-r^2) \\ &= -0.355[dB] \end{aligned} \qquad \textbf{(5-2)}$$

In addition to the loss introduced by reflection, there are losses due to misalignment.

Transverse Offset

$$Loss \cong 4.343\left(\frac{x}{w_0}\right)^2 \text{ [dB]} \qquad \textbf{(5-3)}$$

$w_o$ = mode field radius

$x$= transverse offset

Longitudinal Separation

$$Loss \cong 5.3\left(\frac{z\lambda}{10w_0^2}\right)^2 \text{ [dB]} \quad \textbf{(5-4)}$$

$z$ = longitudinal separation

$\lambda$ = wavelength

Angular Misalignment

$$Loss \cong 8.86\times10^{-9}\left(\frac{w_0\theta}{10\lambda}\right)^2 \text{ [dB]} \quad \textbf{(5-5)}$$

$\theta$ = angular tilt [μrad]

Combined Loss equation [valid for individual losses < 1 dB [25]

$$Loss \cong 4.343\left(\frac{x}{w_0^2}\right)^2 + 5.3\left(\frac{z\lambda}{10w_0^2}\right)^2 + 8.864\times10^{-9}\left(\frac{w_0\theta}{10\lambda}\right)^2 \text{ [dB]} \quad \textbf{(5-6)}$$

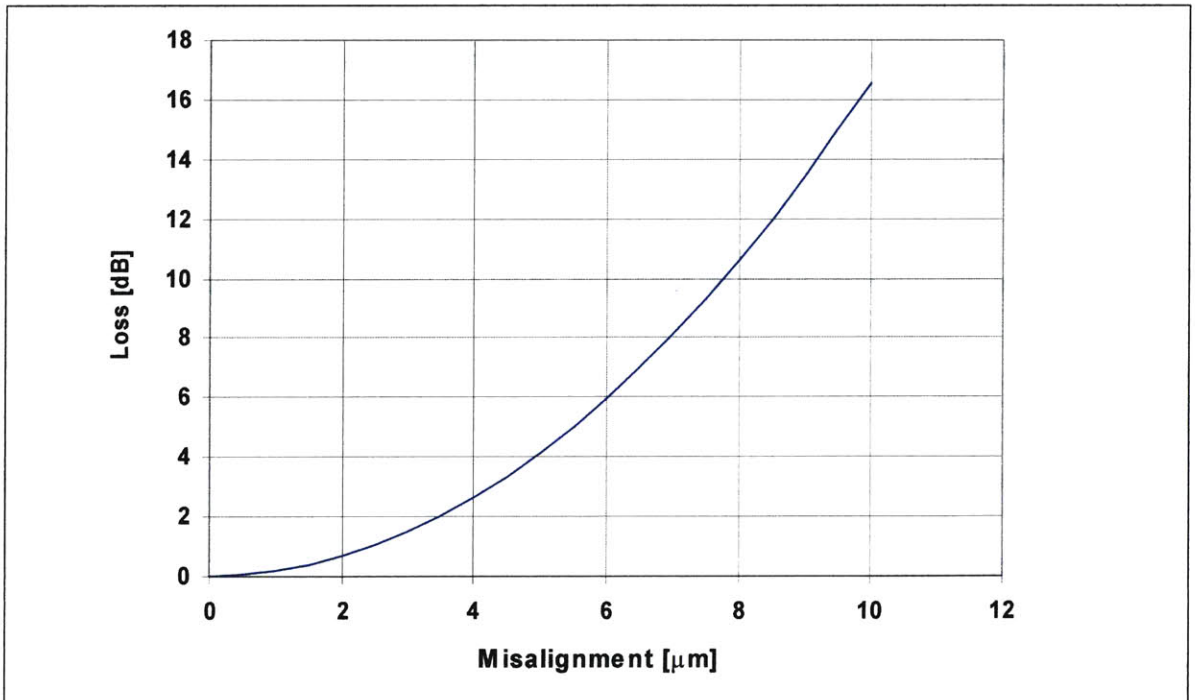


**Figure 5-1 Transverse offset**

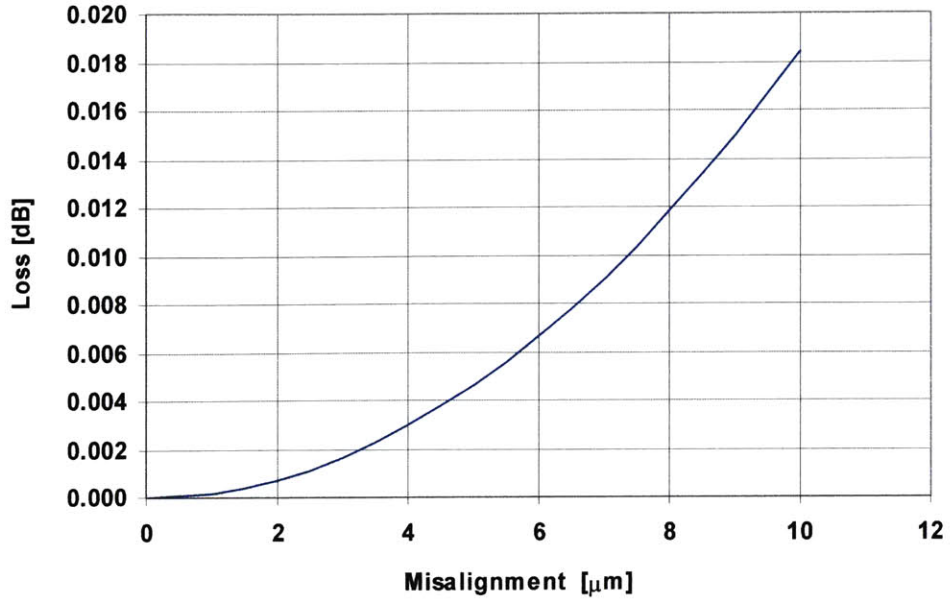


**Figure 5-2 Longitudinal offset**

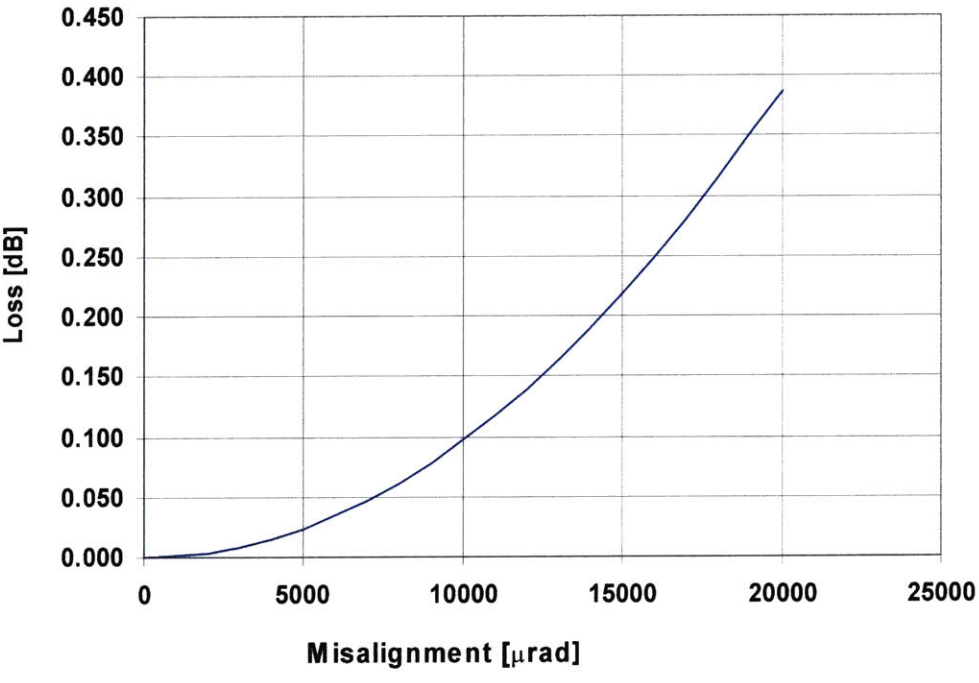


**Figure 5-3 Longitudinal separation**

## 5.2 Testing

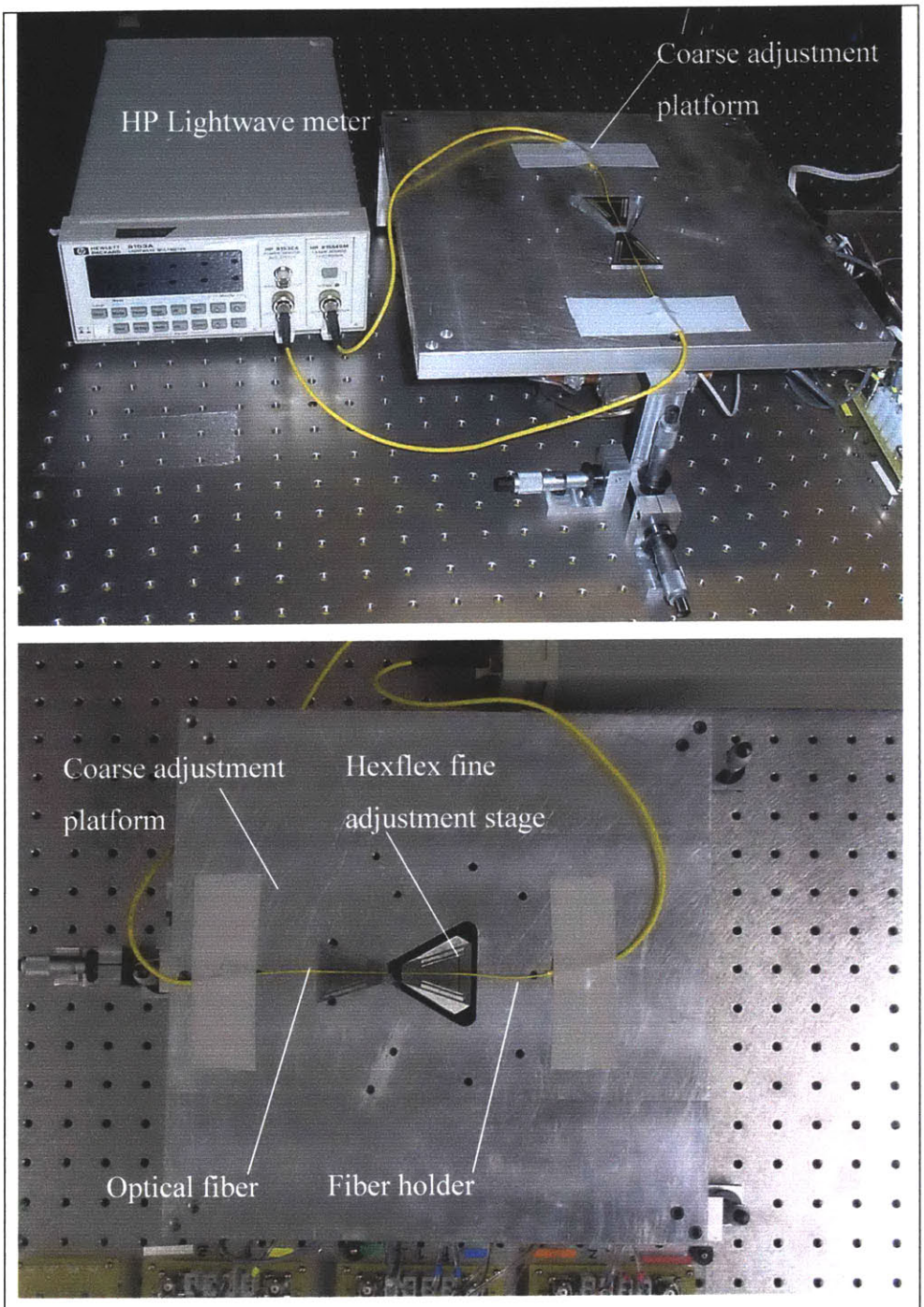


**Figure 5-4 Fiber alignment apparatus**

Figure 5-4 shows the nano-manipulator in use as an ultra-precision fiber aligner. The platform positioned over the Hexflex provides the initial coarse alignment, while the Hexflex acts as the fine motion stage. The probe target (see Figure 3-24) is equipped with a flexure clamp which anchors one fiber to the manipulator. The second fiber is mounted to the stationary platform via a second flexure clamp.

The 100 x 100 x 100 μm working volume of the Hexflex proved adequate for the final linear alignment of the fiber, but the 4000 μrad rotational range was insufficient. The latter limitation necessitated initial coarse alignment to within 0.6° or about 10000 μrad of the ideal value– not easily achieved on a coarse stage designed for translation and not rotation.

By varying the x,y,z and theta z position of the Hexflex, the transmission loss was reduced to the minimum possible attenuation - 0.36dB. The plane of the fiber was 50mm from the Hexflex centroid, making the fiber position very sensitive to drift in theta x and theta y. The chart bellow records the positioning stability.

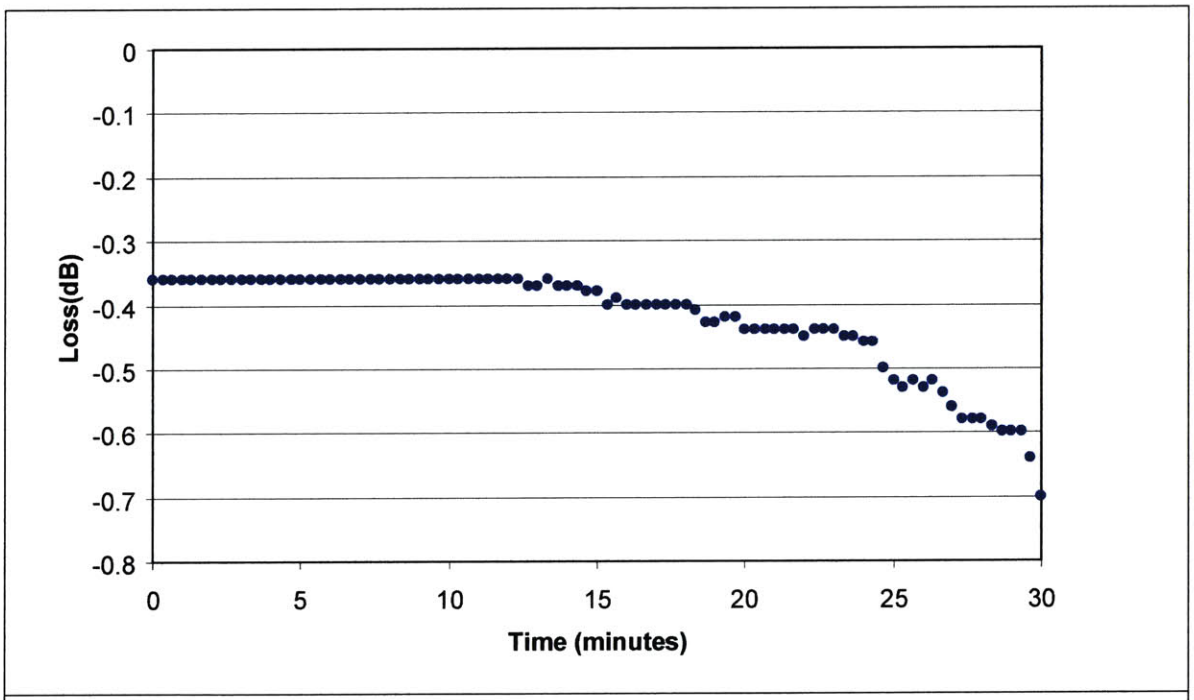


**Figure 5-5 Transmission loss vs. time**

# Chapter 6 Conclusions

This work has shown that the Hexflex can form the basis of a viable positioning system. The six actuator inputs allow for compensation of parasitic errors in all six degrees of freedom. Thus the device is inherently more tolerant of machining and assembly inaccuracy which give rise to these undesired motions. This means low cost, low precision machining techniques such as waterjet machining can be employed.

The actuator design tolerates ±1 mm actuator misalignment with less than 0.1% full-scale position error. Measurements over a 100x100x100nm$^3$ work volume show resolution and error motions better than 5nm. Measurements over a 100x100x100μm$^3$ work volume indicated error motions less than 0.20% full-scale. The mechanism's equilateral symmetry and planar geometry make it inherently stable with respect to uniform temperature changes. The maximum thermal drift was 23 nm and 4 μradians over 30 minutes as the temperature of the base changed 0.1°C. The manipulator, built for $ 2000, was successfully aligned to single mode optical fibers with a transmission loss of -0.36dB. The design requirements of Table 3-1 were satisfied in terms of work volume, resolution and start-up drift. Regrettably the open loop accuracy requirement of 150nm was not met. The worst case inaccuracy was 198nm for y motion as recorded in Table 4-1 and Figure A-2. Improvements to open loop accuracy can be made by reducing the tab range of motion. Not only will it reduce the variation in force shown in Figure 3-17, but also the cross talk from the other coils in the actuator assembly (cross talk forces are zero when the magnets are placed symmetrically between the coils – they increase with magnet displacement).

At present the ratio of working volume to effective volume occupied is 0.001mm$^3$ / 1838510mm$^3$ =5.4 x $10^{-10}$. It is estimated that with higher field density actuators and improvement to flexure design this can be increased by a factor of 10.

Future work should concentrate on increasing the actuator specific force. Air core solenoids were selected because of their superior linearity in open loop control. The

incorporation of ferromagnetic material in the magnetic circuit will increase actuator specific force, natural frequency (smaller magnet housings on tabs) and reduce heat dissipation. Control using position feedback will be necessary because of the hysteretic behavior of the ferromagnetic components. Variants of the magnet coil actuator should also be considered where the coil is now attached to the moving tabs and the magnets are fixed to the base.

# Chapter 7 References


[1] Ryu, J.W., Gweon, D., Moon, K.S., 1997, "Optimal design of a flexure hinge based XYθ wafer stage" Precision Engineering, v21, No.1, pp 18-28.

[2] Nomura, T. and Suzuki, R., Jan 1992, "Six-axis controlled nanometer-order positioning stage for microfabrication" Nanotechnology, Vol.3, No.1, pp 21-28

[3] Taniguchi, M., Ikeda, M., Inagaki, A., Funatsu, R., March 1992, "Ultra Precision Wafer Positioning by Six-axis Micro-motion Mechanism," Int. J. Japan Soc. Prec. Eng., Vol.26, No.1, pp.35-40.

[4] Holmes, M., Hocken, R., Trumper, D., July 2000, "The long-range scanning stage: a novel platform for scanned-probe microscopy," Precision Engineering, v24, No. 3, pp 191-209.

[5] Stewart, D. "A platform with six degrees of freedom," Proc. of the Institute of Mechanical Engineers, London, England, 1965, Vol. 180,pp. 371-386.

[6] Bernhard, J., Benavides, L., and Allen, J., "Planar and Spatial Three-Degree-of-Freedom Micro-stages in Silicon MEMs", Proceedings of the 16th Annual ASPE Meeting, November, 2001.

[7] Dagalakis, N. and Amatucci, E., "Kinematic Modeling of a 6 Degree of Freedom Tri-stage Micro-Positioner", Proceedings of the 16th Annual ASPE Meeting, November, 2001.

[8] Kota, Sridhar, "Exploiting Elasticity in Engineering Design: Synthesis and Applications", Invited Lecture at MIT Fall 2001 Mechanical Engineering Seminars, September 28, 2001.

[9] Culpepper, M., ''Design of a Low-cost Nano-manipulator Using a Monolithic, Spatial Compliant Mechanism", article submitted to the Journal of Precision Engineering, Jan 2003, pp 3,4.

[10] Slocum, A.H. "Precision Machine Design" Society of Manufacturing Engineers, Dearborn, 1992, pp 522 -524.

[11] Smith, S.T. and Chetwynd, D.G., "Foundations of Ultraprecision Mechanism Design" OPA , Amsterdam,1992, pp 189-219.

[12] Gallego-Juarez, J.A., "Piezoelectric ceramics and ultrasonic transducers,"J.Phys E:Sci.Instrum.v22, 1989, pp 804-816.

[13] Hatheway, A.E., Pasadena, California, 91101, (626) 795-0514, www.aehinc.com.

[14] Weck M. and Bispink T., "Examination of high precision slow motion feed drive systems for the sub-micrometer range" Progress in Precision Engineering ed. Seyfried P., Kunzmann H., McKeown P. and Weck M., Springer Verlag, Berlin, 1991.

[15] ETREMA Products, Inc. Worldwide Headquarters 2500 N. Loop Drive Ames, Iowa 50010 U.S.A. (515) 296-8030. www.etrema-usa.com.

[16] Piezosystem Jena, Inc.54 Hopedale Street Hopedale, MA 01747 USA (508) 634-6688 www.piezojena.com.

[17] Yaeger J.R. "A practical shape-memory electromechanical actuator", Mechanical Engineering, 1984,pp 51-55

[18] Jebens R.,Trimmer W.& Walker J.,1989, Micro actuators for aligning optical fibers, Proc. Second IEEE Workshop on Micro-Electromechanical Systems, Salt Lake City, 1989 35-39.

[19] Smith, S.T. and Chetwynd, D.G., "An optimized magnet-coil force actuator and its application to precision elastic systems" Proceedings of the Institute of Mechanical Engineers. Part C, Journal of Mechanical Engineering Science, Mechanical Engineering Publications Ltd, London, 1990, Vol. 204, No. C4, pp 243-253.

[20] Montgomery, D.B. "Solenoid magnet design, 1969 (Wiley Interscience, New York)

[21] Jones R.V., "Instruments and Experiences; Papers on Measurement and Instrument Design', J.Wiley and Sons, NY, pp219-247

[22] Garrett, M W ' Calculation of Fields, Forces and Mutual Inductances of Current Systems by Elliptic Integrals' Journal of Applied Physics V34, No. 9, September 1963. p 2567 -2573.

[23] Hecht, E., "Optics, 4th ed" Addison-Wesley Longman, Reading, Massachusetts, 2002. p 115.

[24] Mickelson, A.R., Basavanhally, N.R.., Lee, Y., "Optoelectronic Packaging" John Wiley & Sons, Inc., New York, p50

[25] Jeunhomme, J.B., "Single-Mode Fiber Optics" Marcel Dekker, Inc., New York, 1983

[26] Polytech PI. F-206 Memo. "Hexapod Thermal Characteristics" October 9th 2001 p1.

[27] McMaster-Carr. P.O. Box 440 New Brunswick, NJ 08903-0440. (732) 329-3200 www.mcmaster.com

# Appendix A Electromagnet Actuation

Six pairs of plots record centroid response to x,y,z, theta x, theta y and theta z command inputs. Range is 100 μm for translation and 4000 μrad for rotation. A second set of 3 pairs of plots record motion for x,y and z command inputs over a 100 nm range.

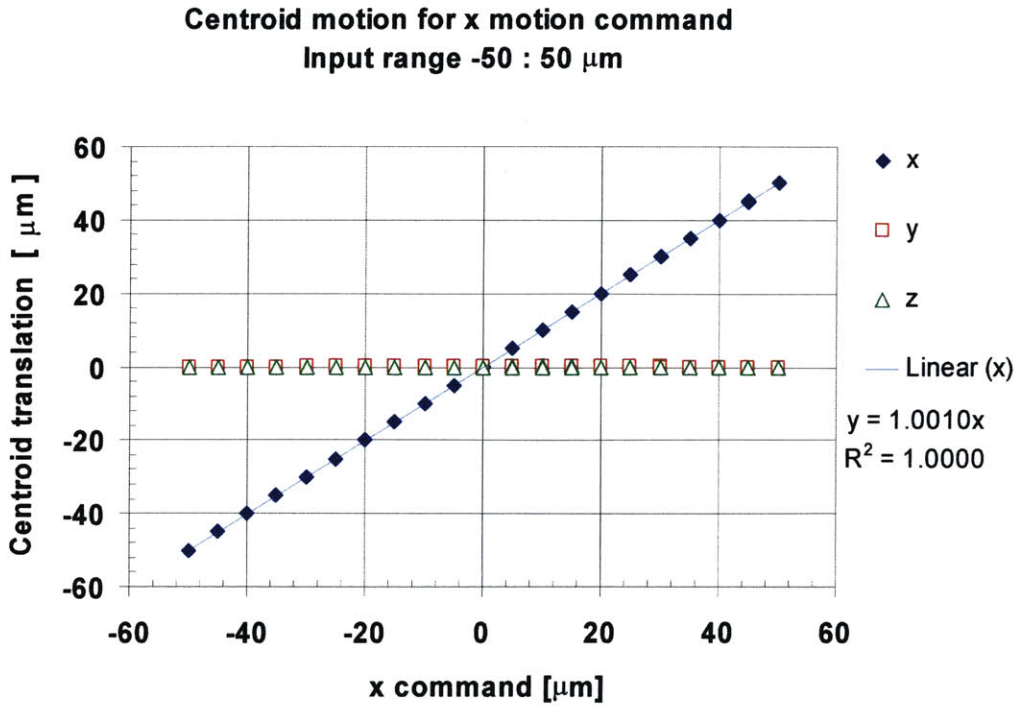


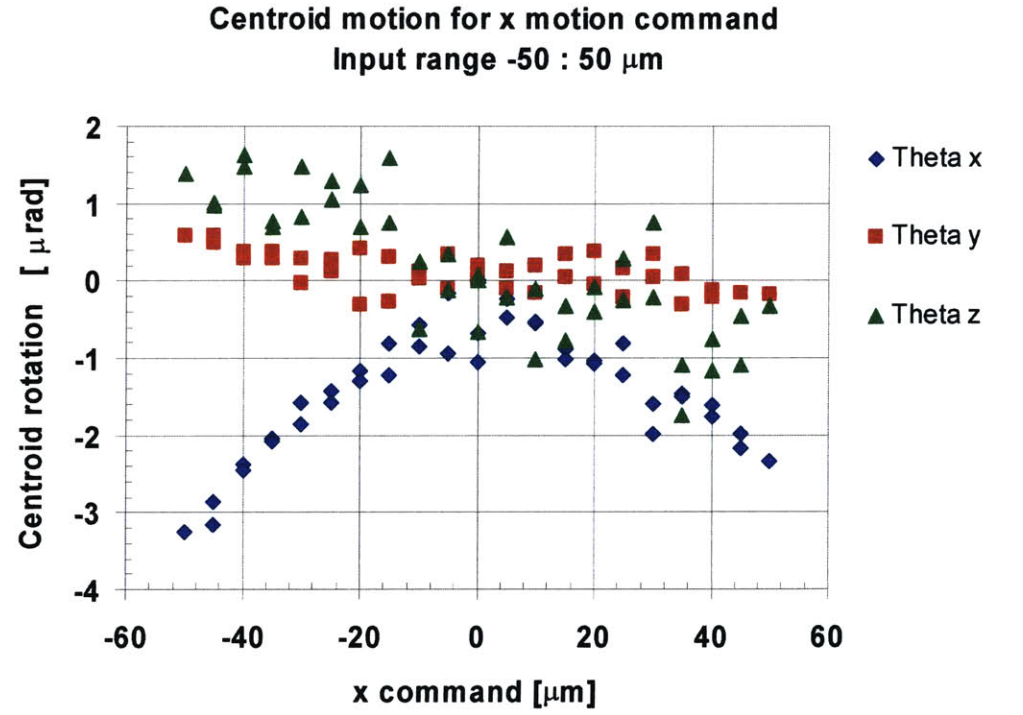


**Figure A-1 Response to x command input (micro-manipulation)**

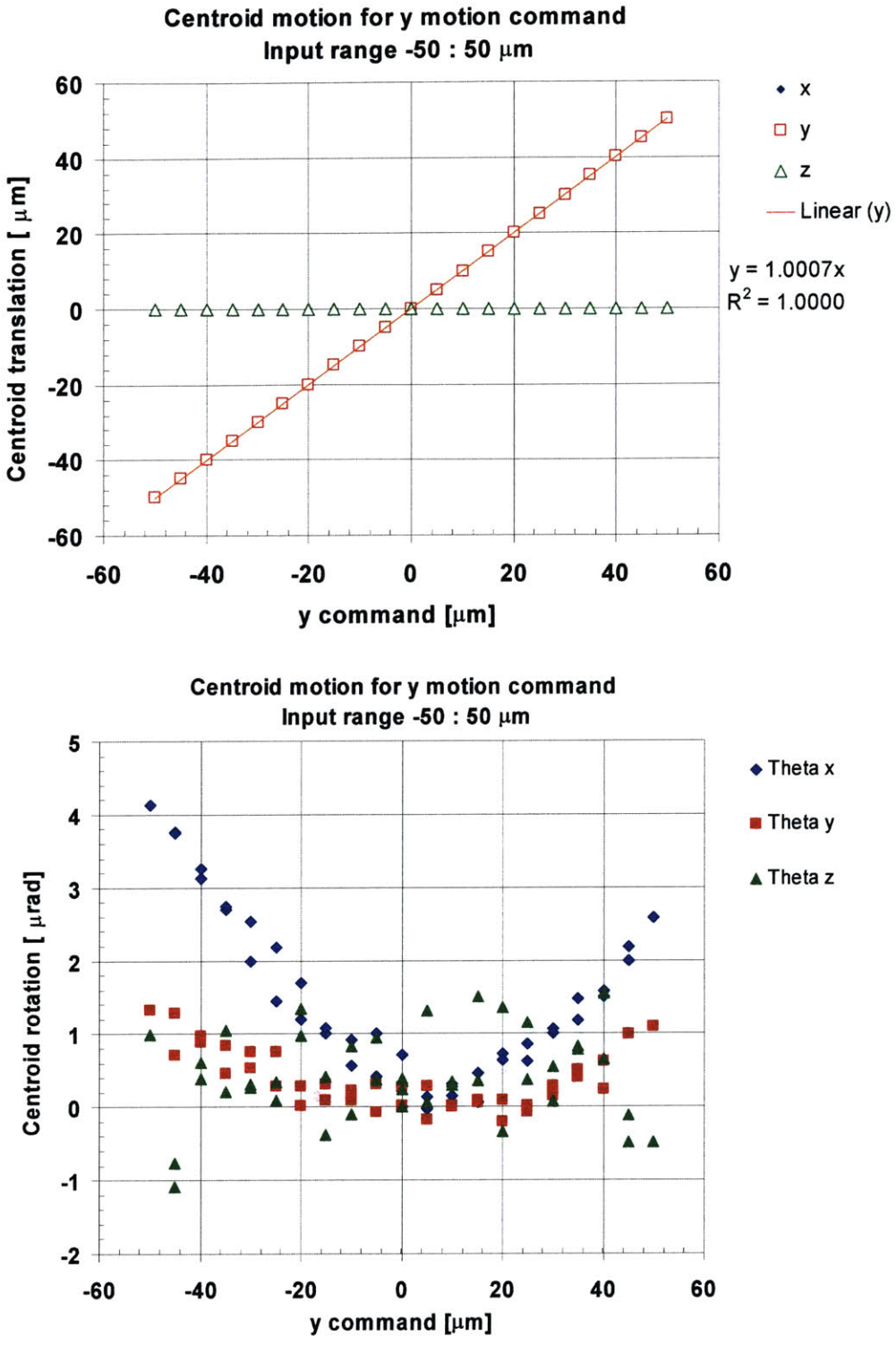


**Figure A-2 Response to y command input (micro-manipulation)**

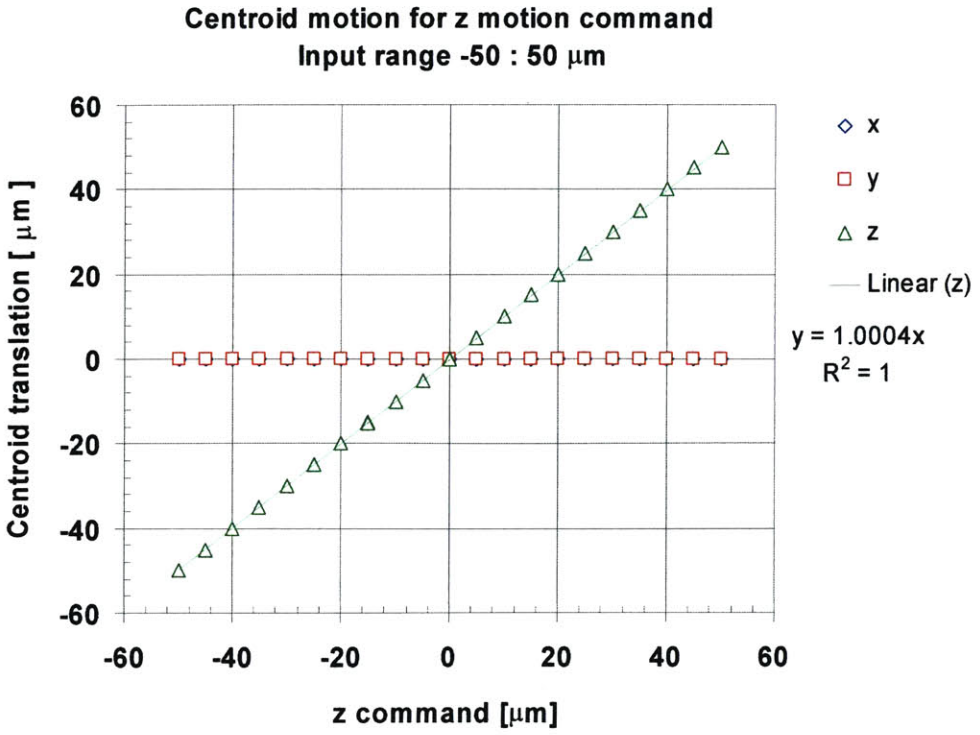


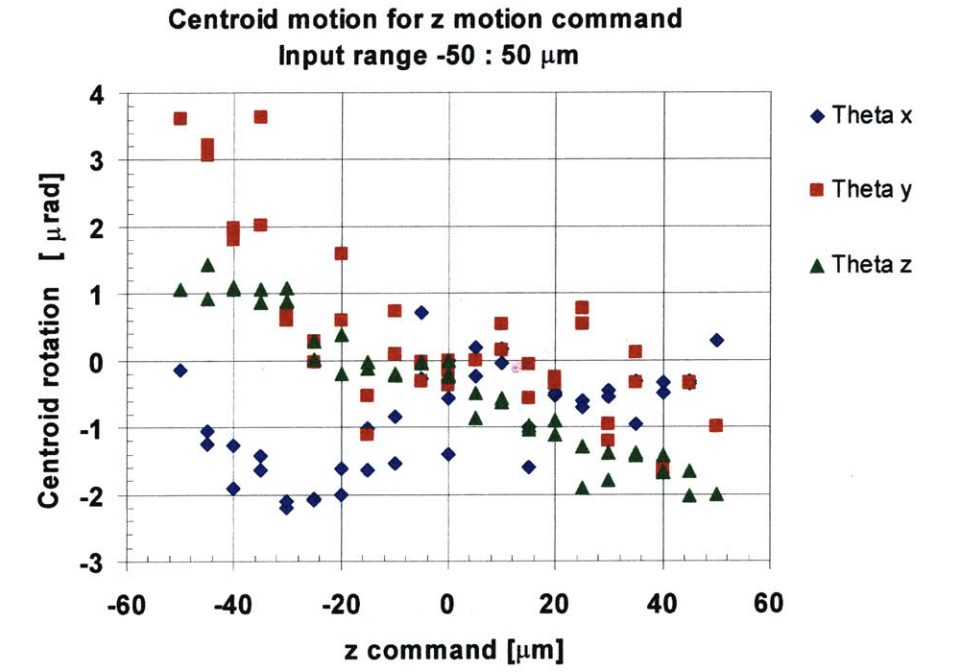


**Figure A-3 Response to z command input (micro-manipulation)**

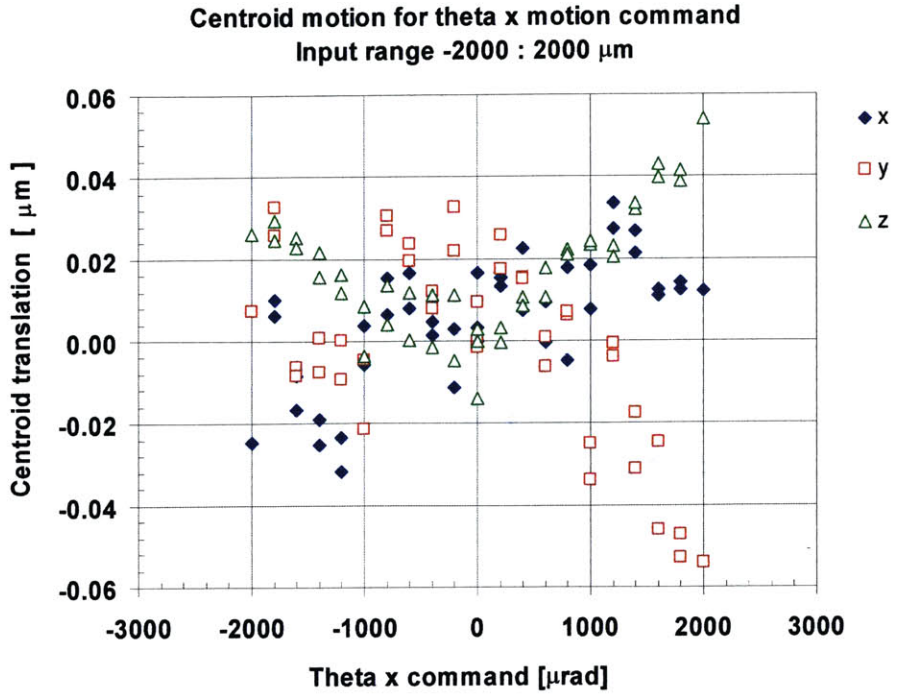


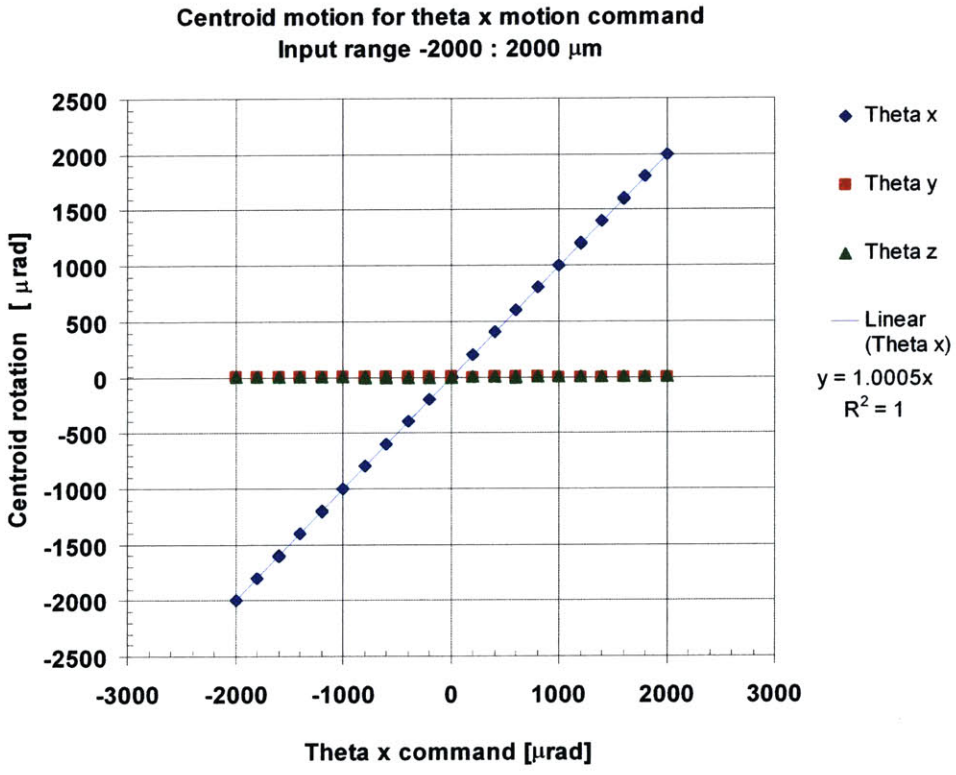


**Figure A-4 Response to theta x command input**

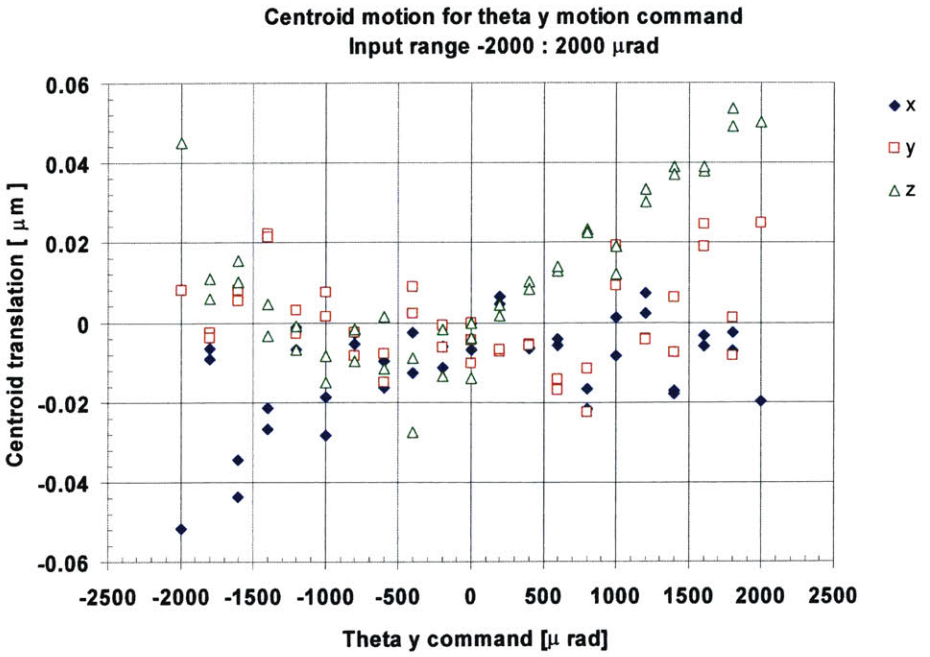


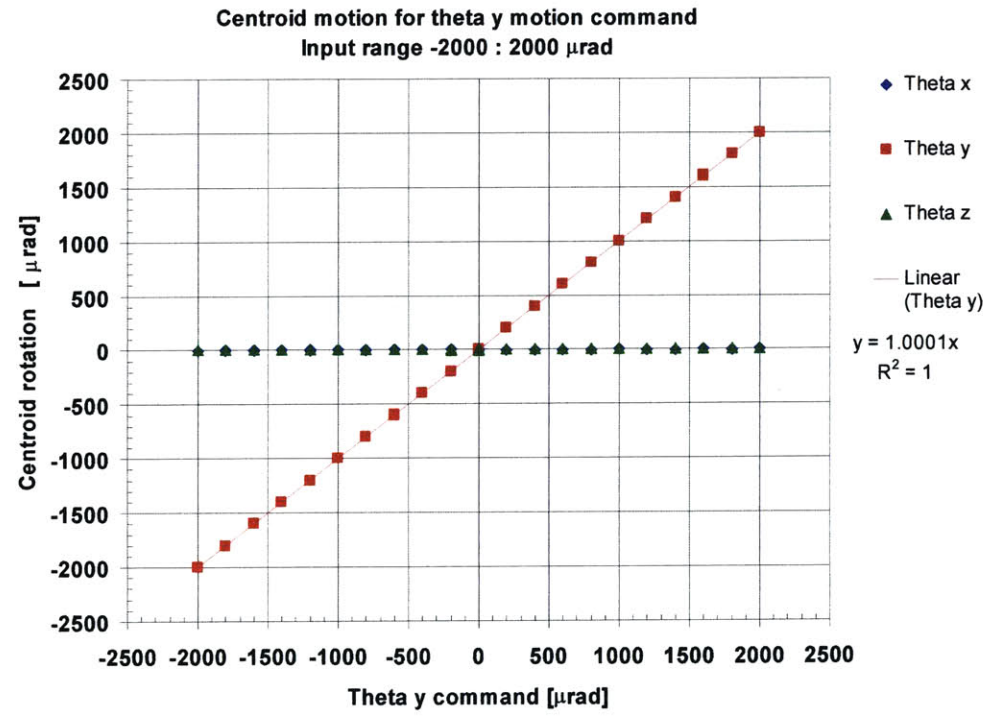


**Figure A-5 Response to theta y command input**

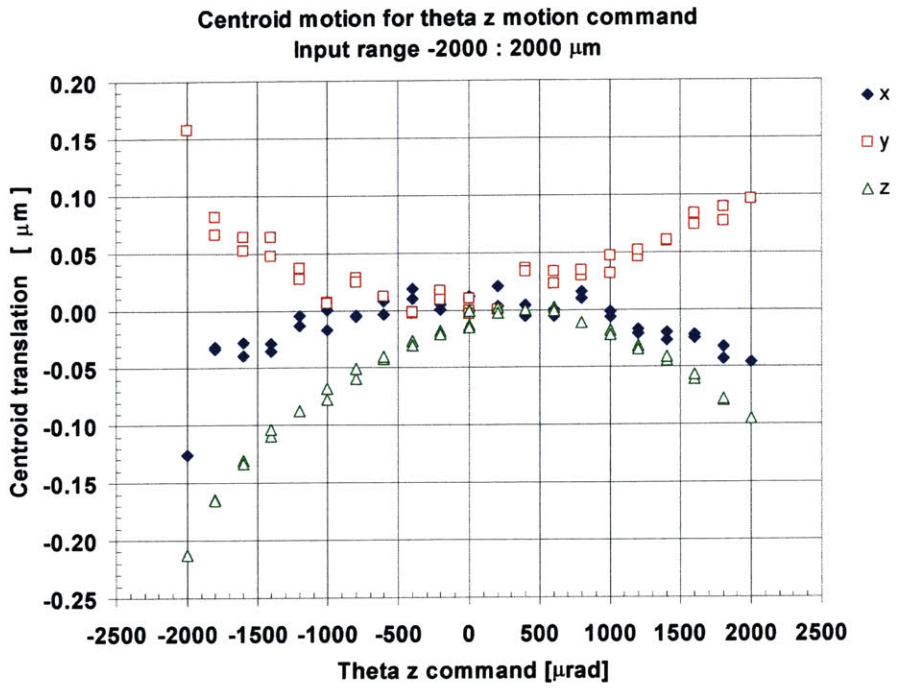


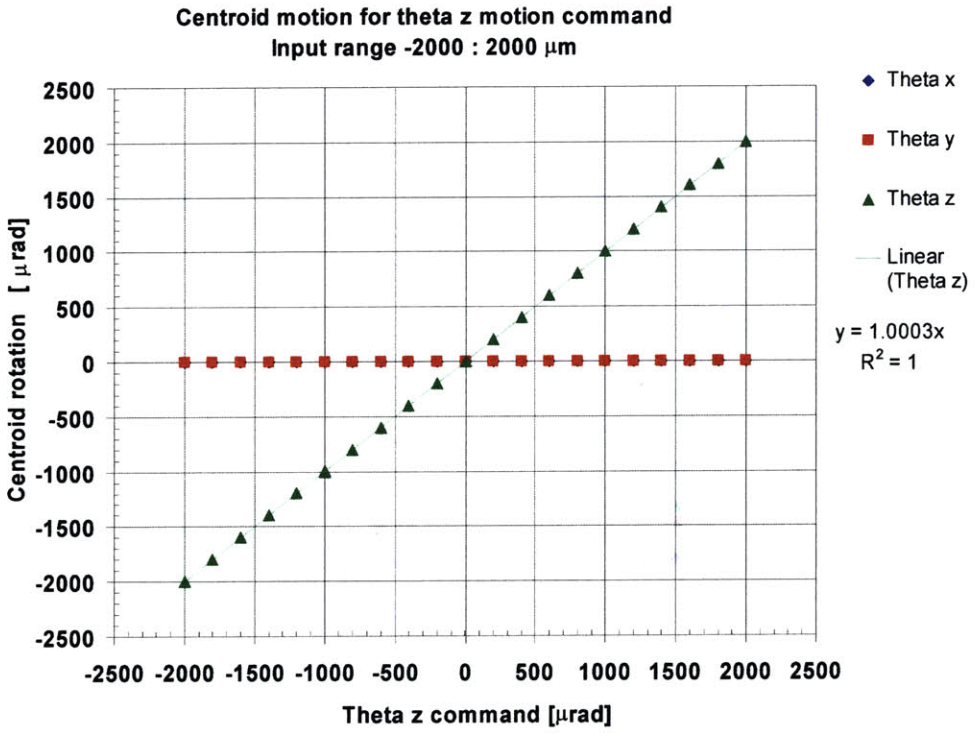


**Figure A-6 Response to theta z command input**

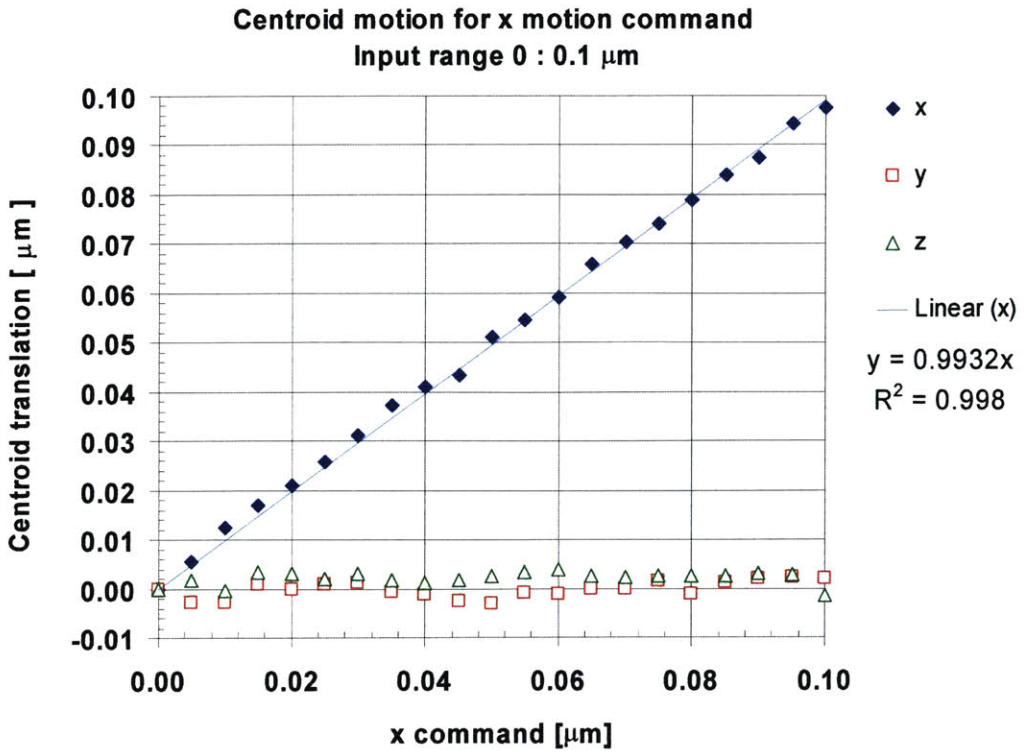


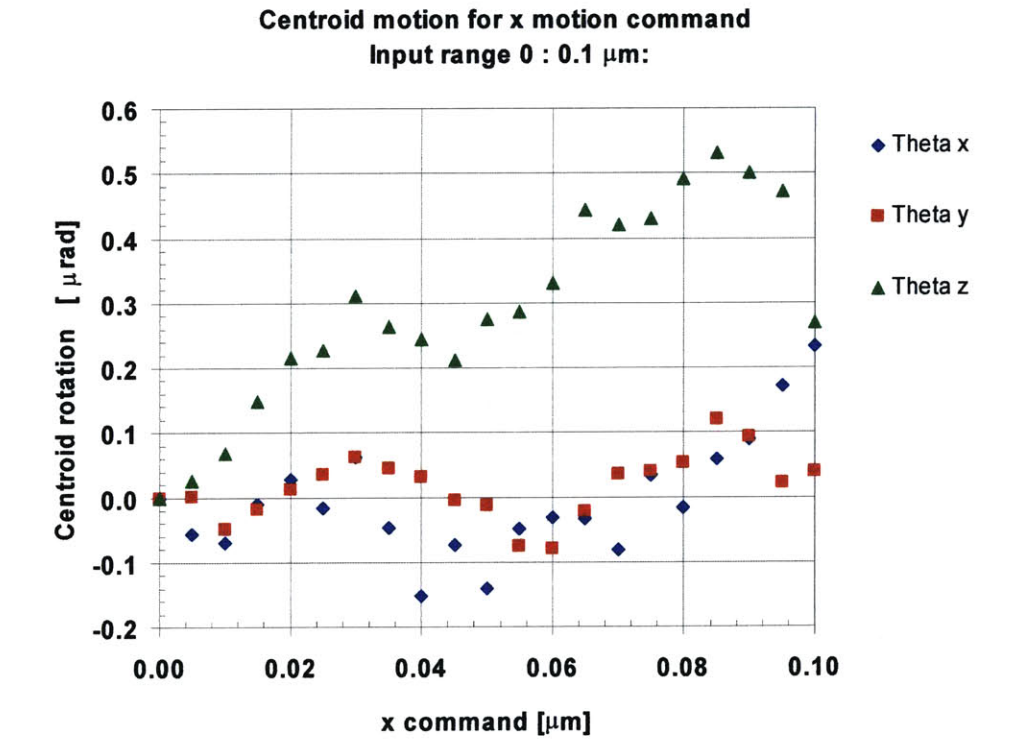


**Figure A-7 Response to x command input (nano-manipulation)**

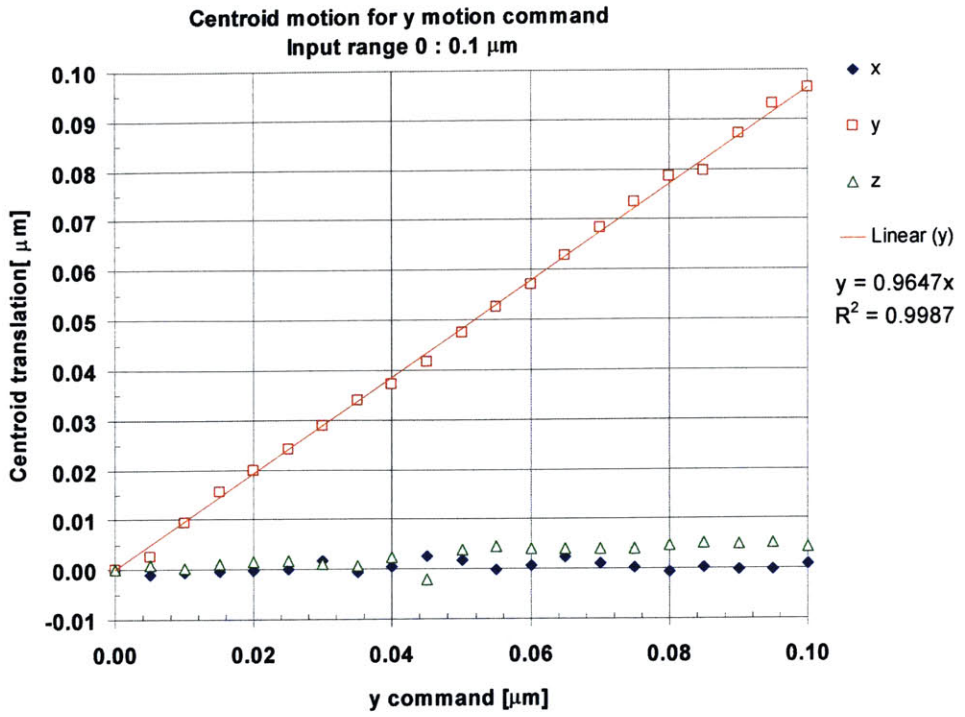


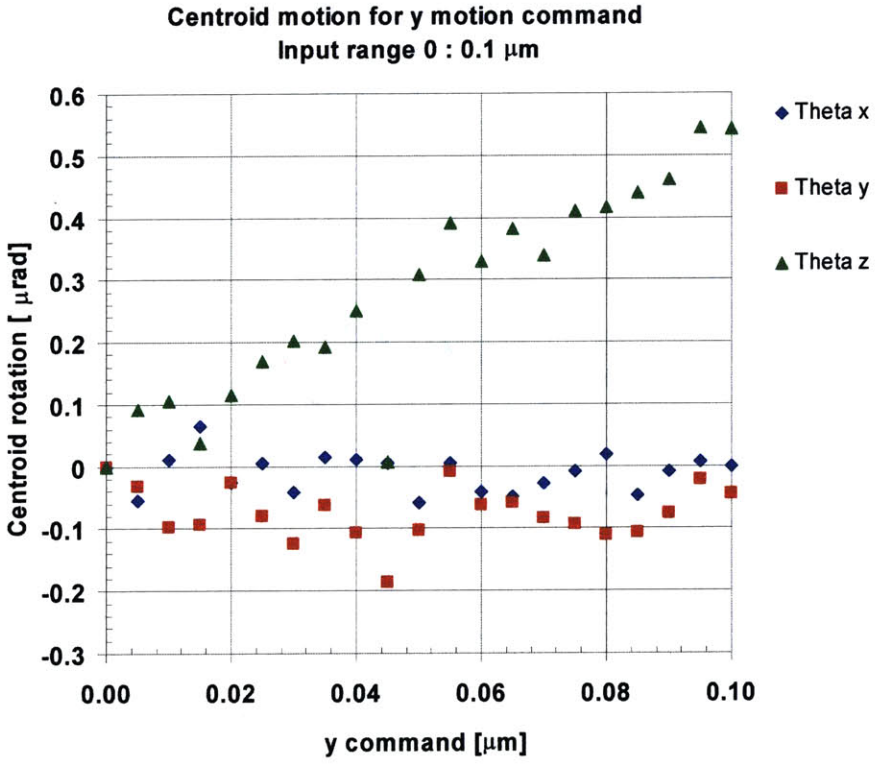


**Figure A-8 Response to y command input (nano-manipulation)**

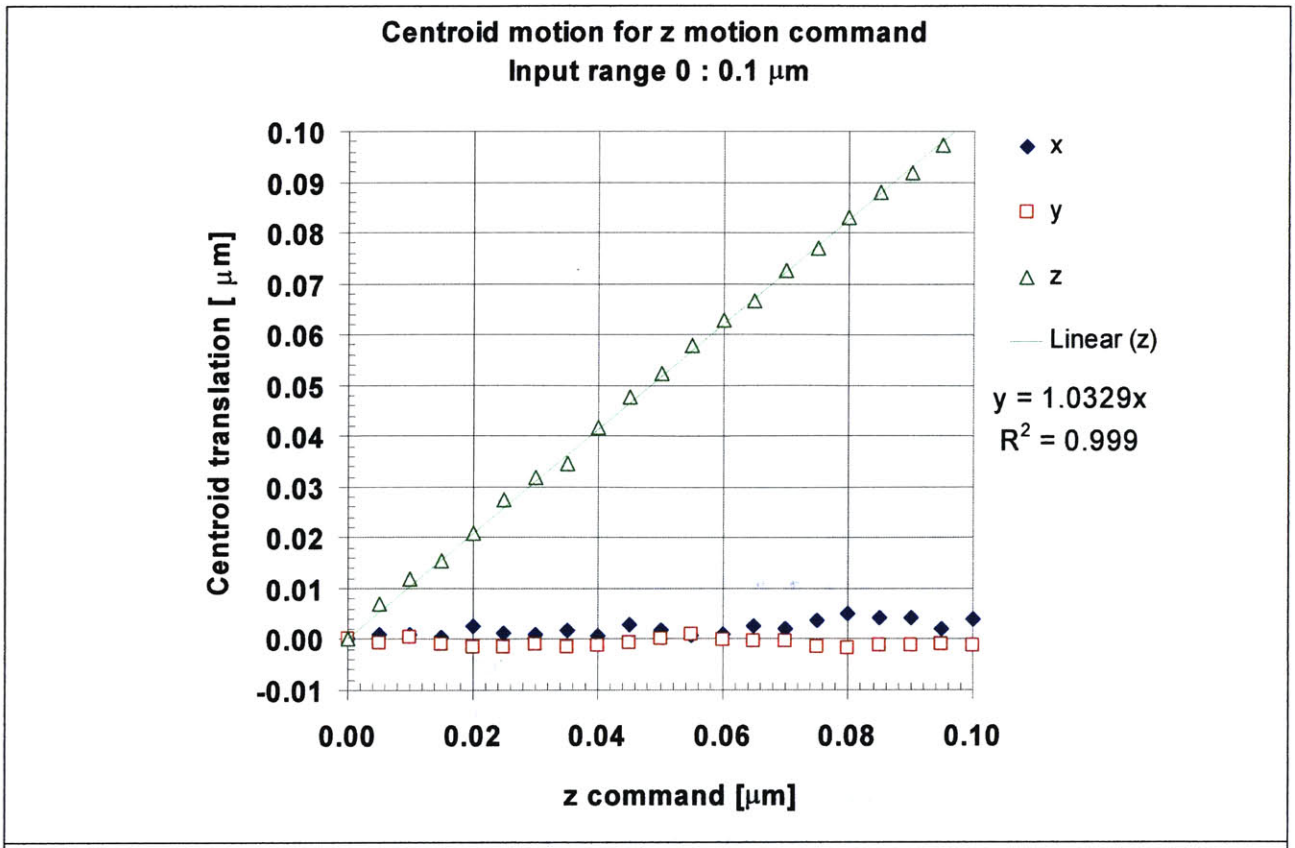


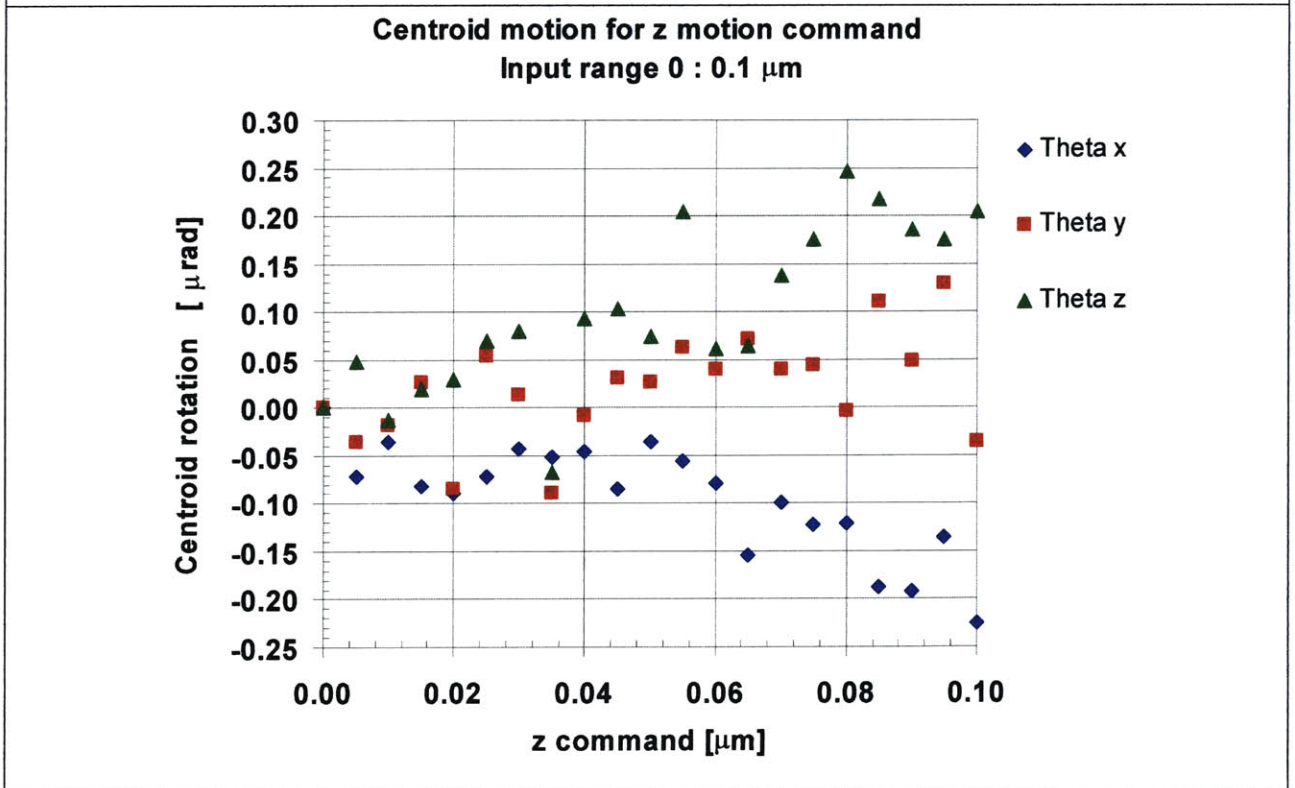


**Figure A-9 Response to z command input (nano-manipulation)**

# Appendix B Repeatability Histograms

The histograms record 100 position measurements of the stage after it was stepped over a nominal range of 52 μm from x = y =z =15μm to x =y =z =-15 μm and then back again.

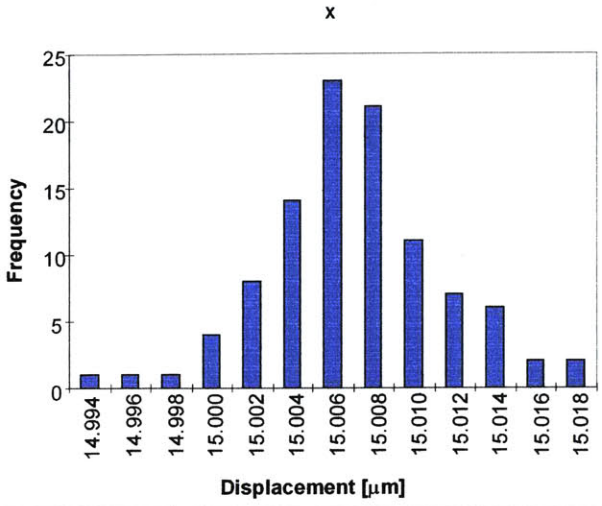


$\sigma_x = 0.004$ μm

$3\sigma_x = 0.013$ μm

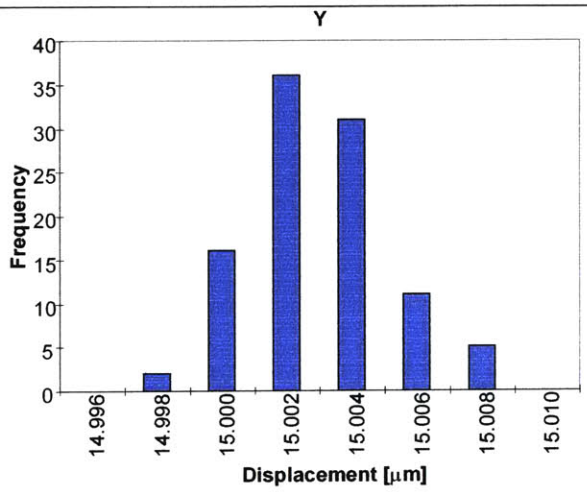


$\sigma_y = 0.002$ μm

$3\sigma_y = 0.007$ μm

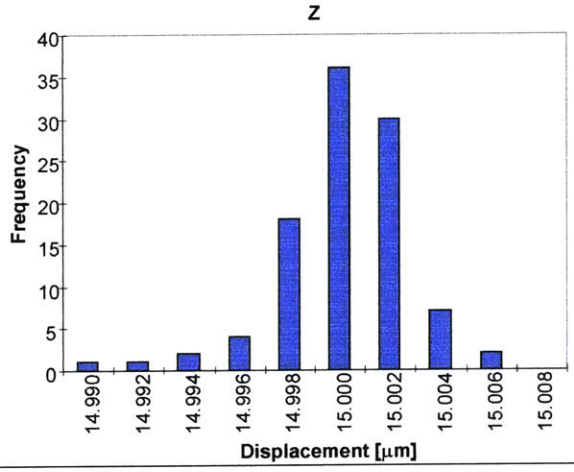


$\sigma_z = 0.003$ μm

$3\sigma_z = 0.008$ μm

**Figure B-1 Repeatability summary**

# Appendix C Frequency Response Plots

The response to a manual 'tap' was recorded for a 0.2s interval at a sampling rate of 10kHz.

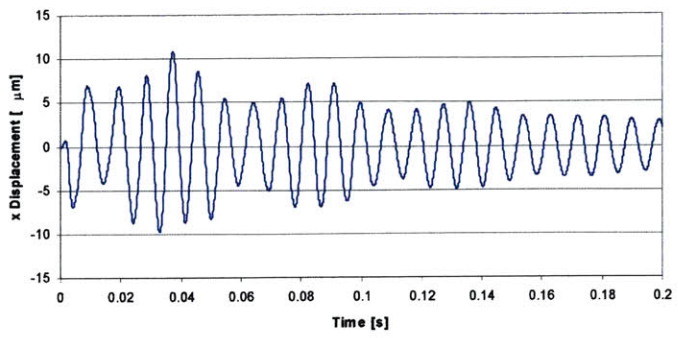


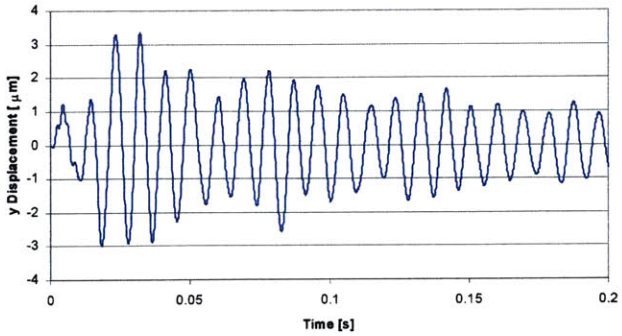


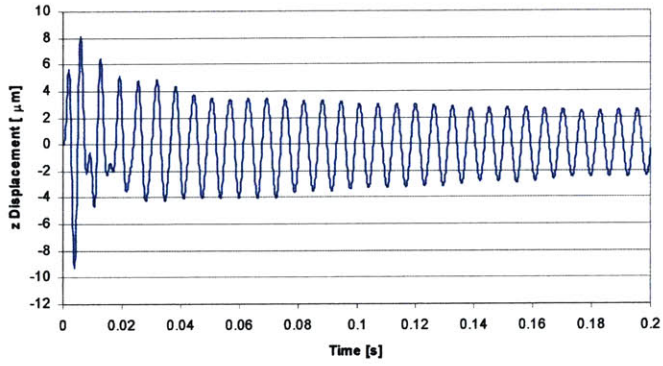


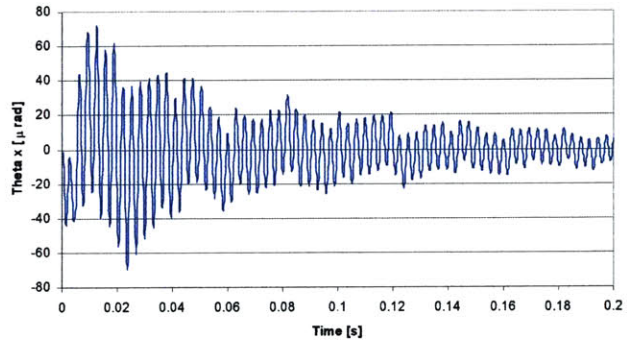


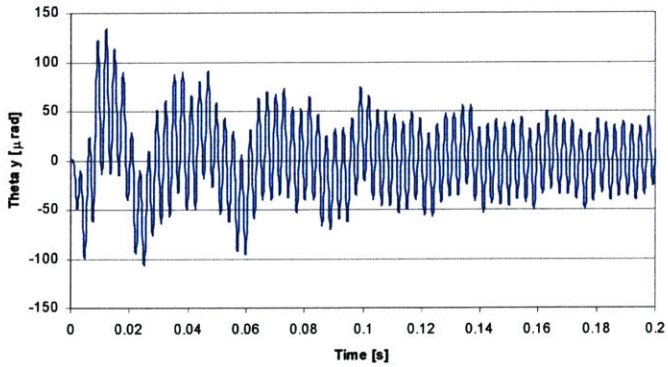


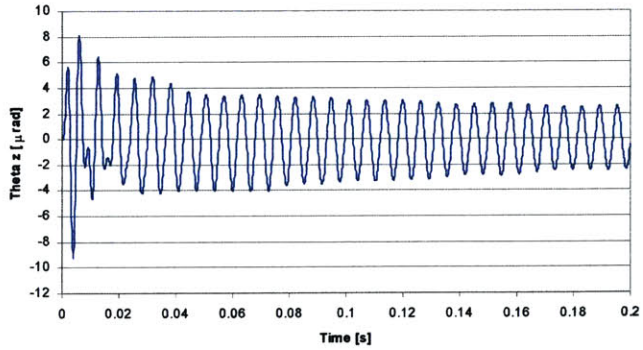


**Figure C-1 Response to impulse**

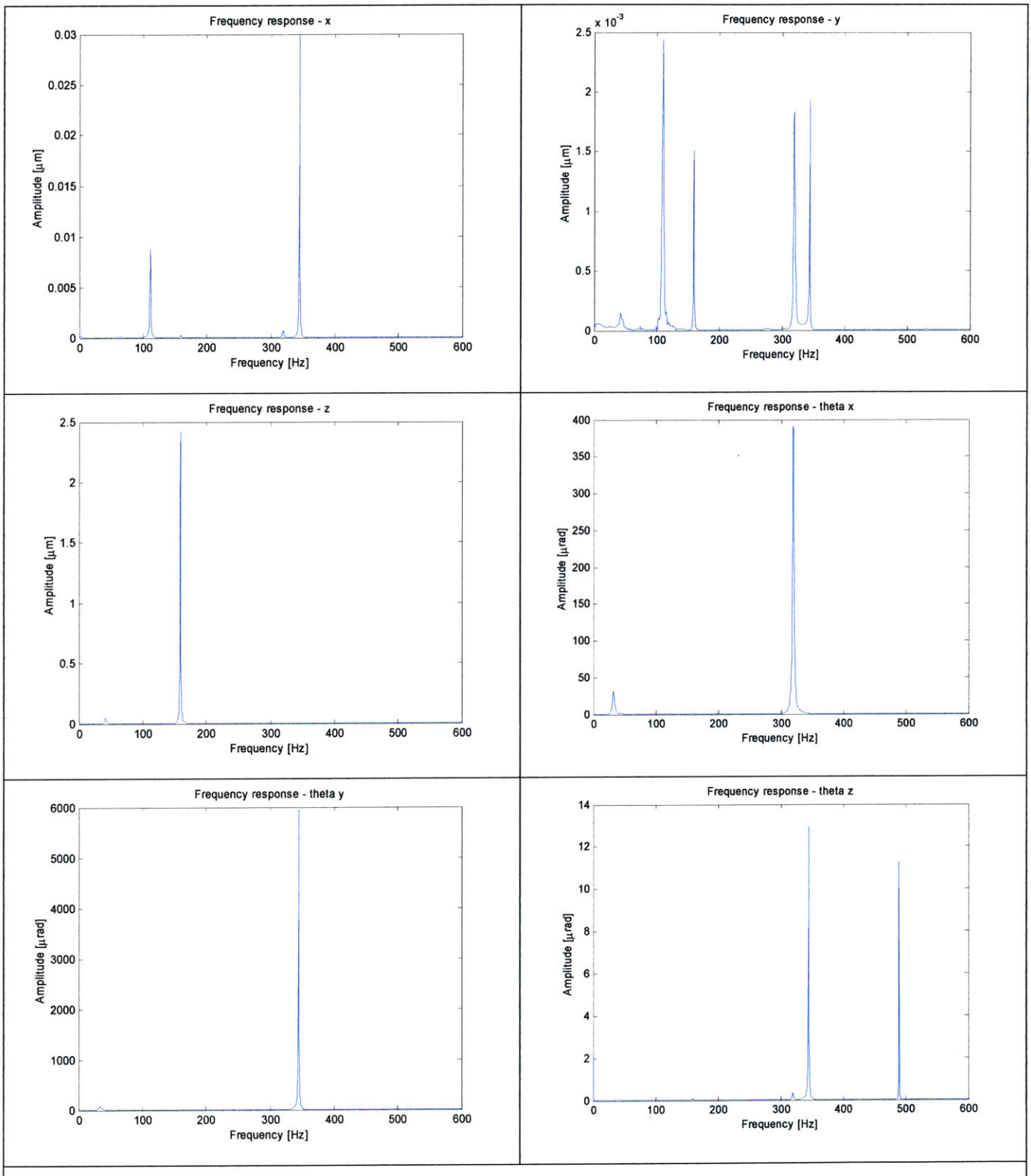


**Figure C-2 Frequency response**